A Long Optical Cavity For Sub-Hertz Laser Spectroscopy

Sana Amairi ep Pyka

A Long Optical Cavity For Sub-Hertz Laser Spectroscopy

Von der QUEST-Leibniz-Forschungsschule
der Gottfried Wilhelm Leibniz Universität Hannover

zur Erlangung des Grades

Doktorin der Naturwissenschaften
Dr. rer. Nat.

genehmigte Dissertation

von

Msc. Sana Amairi ep Pyka
geboren am 22. September 1985 in Tunis, Tunesien

2014

Referent: Prof. Dr. Piet O. Schmidt
Korreferent: Prof. Dr. Christian Ospelkaus
Tag der Promotion: 29. Juli 2014

He who is to be a good ruler must have first been ruled.

Aristotle (384-322 BCE)

Abstract

The development of stable narrow-linewidth lasers is essential for high-resolution spectroscopy and tests of fundamental physics, as well as interferometric measurements, such as gravitational wave detection. In the field of optical frequency standards, the instability of the clock interrogation laser limits the performance of the most sophisticated optical frequency standards to a level of $10^{-16}/\sqrt{\tau}$ for long averaging times τ. Typically, laser stabilization is performed by locking a laser frequency to a resonance of an external high-finesse optical cavity, thus converting the cavity's passive length stability into a frequency stability. The length stability is fundamentally limited by thermal noise; Brownian motion causes local random displacement in the cavity spacer, mirror substrates and mirror coatings. On a less fundamental level, the cavity length is sensitive to the deformation of the cavity material under external perturbations (i.g. vibrations, thermal expansion) and to the variation of the refractive index.

This thesis presents a 39.5 cm long optical cavity featuring an estimated thermal noise limited frequency stability at the level of 7×10^{-17} at 1 s. The stabilized 1070 nm wavelength laser will be frequency-doubled twice (to 267 nm) and used for sub-Hertz clock interrogation of the Al^+ optical frequency standard in PTB.

The first part of the thesis consists of the theoretical study of two approaches to reduce the thermal noise in optical cavities. In the first approach, we investigate the potential and limitations of operating the cavity close to instability, where the beam diameter on the mirrors becomes large. Our analysis shows that even a 10 cm short cavity can achieve a thermal noise limited fractional frequency instability in the low 10^{-16} regime. In the second approach, we increase the length of the optical cavity. We show that a 39.5 cm long cavity has the potential for a fractional frequency instability on the order of 7×10^{-17}. Using finite-element simulations, we design a 39.5 cm cavity, made of ultra-low-expansion material and fused-silica mirrors, with a reduced sensitivity of $\lesssim 10^{-11}/\text{m}\cdot\text{s}^{-2}$ for vibration-induced fractional length changes in all three directions.

The second part of the thesis describes the experimental realization and characterization of the built 39.5 cm long environmentally insensitive cavity. The measured fractional frequency sensitivity to vibration is around or below $10^{-11}/\text{m}\cdot\text{s}^{-2}$ in all three directions. In addition, the effects of thermal fluctuations and vacuum pressure variations on the fractional frequency instability is below the thermal noise limit for averaging times up to 4×10^4 s. Laser stabilization to the cavity was performed using the Pound-Drever-Hall technique. The evaluated residual amplitude modulation effect shows an induced fractional frequency instability of 4×10^{-16} for averaging times shorter than 200 s. Laser intensity stabilization was performed and shows a flicker floor noise limit for the achievable fractional frequency instability of few 10^{-16}.

In the third part, the frequency of the laser stabilized to the 39.5 cm cavity was compared to that of several stable lasers present at PTB. The measurements where performed after transferring the laser via a 350 m long stabilized optical fiber. A frequency comb allows the frequency comparison between lasers of different wavelengths. The results show a flicker floor laser frequency instability at 1.1×10^{-15} for averaging times between 2 s and 200 s. Finally, we discuss the technical issues limiting the current performance of the cavity stabilization and point out possible improvements that will allow us to reach the theoretical thermal noise limit.

Zusammenfassung

Die Entwicklung stabiler Laser mit geringer Linienbreite ist essentiell für hochauflösende Spektroskopie und Tests fundamentaler physikalischer Theorien, sowie interferometrischer Messungen, wie z. B. Gravitationswellendetektion. Im Bereich der optischen Frequenzstandards ist die Instabilität der am höchsten entwickelten Systeme durch deren Uhrenabfragelaser im Bereich von $10^{-16}/\sqrt{\tau}$ für lange Mittelungszeiten τ begrenzt. Die Laserfrequenz wird hier für gewöhnlich auf die Resonanz eines externen optischen Resonators mit hoher Güte stabilisiert, wodurch die passive Längenstabilität des Resonators in eine Frequenzstabilität übersetzt wird. Die Längenstabilität ist fundamental durch thermisches Rauschen begrenzt; Brown'sche Bewegung verursacht hierbei lokale statistische Verschiebungen im Material des Resonatorabstandhalters, der Spiegel, sowie der Spiegelbeschichtungen. Auf einem weniger fundamentalen Niveau hängt die Resonatorlänge von Deformationen des Resonatormaterials unter äußeren Störeinflüssen (z. B. Vibrationen, thermische Ausdehnung), sowie von Änderungen im Brechungsindex ab.

Die vorliegende Arbeit präsentiert einen 39.5 cm langen optischen Resonator mit einer geschätzten Frequenzinstabilität von ungefähr 7×10^{-17} bei 1 s. Der bei einer Wellenlänge von 1070 nm stabilisierte Laser wird zweimal frequenzverdoppelt (auf 267 nm) und anschließend zur Abfrage des Uhrenübergangs des Al^+ optischen Frequenzstandards an der PTB verwendet.

Der erste Teil der Arbeit beinhaltet theoretische Untersuchungen von zwei Ansätzen zur Reduzierung des thermischen Rauschens in optischen Resonatoren. Im ersten Ansatz untersuchen wir Potential und Limitierung von optischen Resonatoren nahe der Instabilität, bei denen der Strahldurchmesser auf den Spiegeln groß wird. Unsere Analyse zeigt, dass bereits mit einem 10 cm langen Resonator eine durch thermisches Rauschen begrenzte relative Frequenzinstabilität von wenigen 10^{-16} erreicht werden kann. Im zweiten Ansatz vergrößern wir die Länge des Resonators. Wir zeigen, dass mit einem 39.5 cm langen Resonator potentiell eine relative Frequenzinstabilität von 7×10^{-17} erreicht werden kann. Mit Hilfe von Finite-Elemente-Simulationen entwickeln wir einen 39.5 cm langen Resonator aus Ultra-Low-Expansion Material und Fused-Silica Spiegeln und mit einer reduzierten Empfindlichkeit auf vibrationsbedingte Längenänderungen in allen drei Raumrichtungen von $\lesssim 10^{-11}/(\mathrm{m \cdot s^{-2}})$.

Im zweiten Teil der Arbeit wird die experimentelle Umsetzung und Charakterisierung des 39.5 cm langen umweltunempfindlichen Resonators beschrieben. Die gemessene relative Empfindlichkeit der Frequenz auf Vibrationen beträgt um die $10^{-11}/(\mathrm{m \cdot s^{-2}})$ oder weniger in allen drei Raumrichtungen. Des Weiteren liegen die Beiträge der thermischen Fluktuationen und Vakuumdruckänderungen zur relativen Frequenzinstabilität unterhalb des thermischen Rauschens für Mittelungszeiten von bis zu 4×10^4 s. Die Laserstabilisierung wurde mithilfe der Pound-Drever-Hall-Methode durchgeführt. Die hierbei gemessene Restamplitudenmodulation führt zu einer relativen Frequenzinstabilität von 4×10^{-16} für Mittelungszeiten von weniger als 200 s. Die Stabilisierung der Laserintensität führt zu einer durch Untergrundrauschen begrenzten erreichbaren relativen Frequenzinstabilität von wenigen 10^{-16}.

Im dritten Teil wird die Frequenz des auf den 39.5 cm langen Resonator stabilisierten Lasers mit weiteren an der PTB vorhandenen stabilen Lasern verglichen. Die Messungen wurden nach dem Transfer des Laserlichts durch einen 350 m langen stabilisierten Lichtwellenleiter durchgeführt. Ein Frequenzkamm erlaubt dabei den Vergleich zwischen Lasern mit

verschiedener Wellenlänge. Das Ergebnis zeigt eine relative Laserfrequenzinstabilität bei einem fluktuierenden Untergrund von 1.1×10^{-15} für Mittelungszeiten zwischen 2 s und 200 s. Abschließend diskutieren wir technische Aspekte, durch welche die bisherige Laserstabilisierungsqualität begrenzt ist, und zeigen dabei mögliche Verbesserungen auf, die es uns erlauben sollten, die durch das thermische Rauschen theoretisch gesetzte Grenze zu erreichen.

Schlagwörter: Optischer Resonator, Frequenzstabilisierung, Thermisches Rauschen, Optische Uhr, Vibrationsempfindlichkeit.

keywords: optical cavities, frequency stabilization, thermal noise, optical clock, vibration sensitivity.

Contents

List of Figures

List of Tables

Chapter 1

Introduction

Frequency-stabilized lasers are a key element in modern precision measurements. The scientific community demonstrates an increasing interest in the interaction between light and matter, i.e. laser cooling and trapping of atoms [1–3] and the measurement and manipulation of individual quantum systems [4–6]. The development of frequency stabilization and measurement techniques [7, 8] pushes researchers to establish ultra-narrow linewidth lasers, with applications ranging from tests of fundamental physics [9, 10], over gravitational wave detection [11] to atomic frequency standards [12–16].

Ultra-stable lasers are particulary important for the field of frequency metrology. The stabilized optical laser frequency is used for precision spectroscopy of atoms with narrow atomic transitions, which serve as stable and accurate references for optical frequency standards. In the case of frequency standards employing trapped ions or neutral atoms, the development of cutting-edge techniques for stabilizing optical frequencies, and femtosecond mode-locked lasers for the comparison and absolute measurement of optical frequencies, have revolutionized the field [17]. Besides applications in modern length and frequency metrology [18], the use of optical frequency standards is extended to various fields ranging from research in fundamental physics to commercial applications including the measurement of fundamental constants and their variation with time (i.e. fine-structure constant α), geodesy, precision satellite navigation, etc. [19].

The stability of a clock improves with increasing frequency of the oscillator. Compared with microwave frequency standards, optical frequency standards using an intercombination line in atomic species such as ytterbium, indium, mercury and strontium [12, 15, 16, 20–23] are at least 100 times more stable than the best Cs fountain microwave clock [24]. The newly established quantum state interrogation technique using quantum logic spectroscopy [6, 25] have enabled the development of the single aluminum ion frequency standard using $^{27}\text{Al}^+$. Such a clock, built at NIST, was classified in 2010 as the world's most stable clock, with a frequency instability of $2.8 \times 10^{-15}/\sqrt{\tau}$ where τ is the averaging time, a frequency uncertainty on the order of several parts in 10^{18}, and proven reproducibility with a fractional frequency difference between two Al^+ clocks of -1.8×10^{-17} [14]. However, the short-term instability of the clock interrogation laser of 3×10^{-16} at 1 s [26] remains the primary limit for Al^+ frequency standards. Indeed, until today, the performance of the most sophisticated optical clocks with a theoretical instability of well below 10^{-17} in 1 s is limited by the short term

stability of their local oscillator at the level of a few $10^{-16}/\sqrt{\tau}$ for long averaging time τ [12, 22]

During the last decade, efforts have been multiplied to realise a laser with the lowest possible short term instability. The most common method relies on the use of a passive optical resonator as a frequency ruler [27]. The optical path length inside a passive optical cavity defines the resonance frequency of the stabilized laser. However, this length is subject to perturbations. Environmental perturbations on the cavity optical path length such as temperature fluctuations, mechanical and acoustic vibrations and refractive index variations, can be significantly suppressed by placing the cavity in a vibration isolated vacuum system with stabilized temperature. However a fundamental limit to the cavity length stability arises from the thermal noise; Brownian motion causes local random displacements in the cavity spacer, mirror substrates, and mirror coatings, not avoidable above the absolute zero temperature [28]. State of the art lasers stabilized to passive cavities show a thermal-noise-limited fractional frequency instability on the order of 1 to 3×10^{-16} at 1 s [29–31].

Numata *et al.* showed that, for a cavity made of ultra-low expansion glass and operating at room temperature, the dominant source of thermal noise comes from the mirrors. The thermal noise scaling is proportional to the mechanical losses in the mirror substrate, but inversely proportional to the laser mode diameter at the mirrors. The work reported in this thesis follows this lead and we analyze the feasibility of two alternative approaches to increase the mode size on the mirrors. The first approach is based on cavities operated close to instability, i.e. with a near-planar or near-concentric mirror configuration, whereas the second approach relies on increasing the cavity length. This study brings us to design and realise a 39.5 cm long stable optical cavity with an estimated thermal noise limit of 7×10^{-17} at one second. This cavity will then stabilize the 1070 nm clock for the interrogation of the clock transition in the Al^+ ion at PTB [32].

Outline of thesis

In addition to the introduction presented in this first chapter, this thesis contains four main chapters concluded by a summary chapter. The chapters are organized as follows:

- Chapter 2: The necessary tools for understanding the notion of laser frequency stabilization are presented. Allan deviation analysis of the frequency instability as well as laser noise sources and their effect on a single ion frequency standard are explained. We also present the theory of a passive optical resonator, and the use of the Pound-Drever-Hall technique for laser frequency stabilization to a passive optical resonator.

- Chapter 3: A theoretical study of reducing thermal noise in optical cavities is presented. Here, we analyze the feasibility of two alternative approaches to increase the mode size on the mirrors. The first approach is based on cavities operated close to instability, i.e. with a near-planar or near-concentric mirror configuration, whereas the second relies on long cavities. In the latter approach, relative frequency fluctuations are further suppressed since they scale with the inverse of the cavity length. We show through simulations that a 10 cm long cavity, when operated near instability, can achieve a thermal-noise-limited instability of 1.5×10^{-16} at 1 s, whereas a 39.5 cm long cavity has the

potential to achieve an instability below 10^{-16} at 1 s. Possible technical limitations of near-concentric and near-planar cavities arising from the dense mode structure close to instability and an estimation of the effects on the laser frequency stabilization are investigated. A major challenge for long cavities is the required insensitivity to accelerations. We present a 39.5 cm long cavity design with a vibration sensitivity of the fractional length change of $< 10^{-10}$/g in all three directions, assuming realistic machining tolerances. The results of this chapter have been published in [33].

- Chapter 4: The experimental details of the optical and electronic setup of the laser stabilization to the 39.5 cm long cavity are presented. We show in this chapter that we have realized an environmentally insensitive long optical cavity. The measured cavity sensitivity to mechanical vibrations at frequencies below 100 Hz is on the order of 10^{-11}/g in the axial direction and 10^{-12}/g in the horizontal and vertical directions, the lowest reported up to the present for such a long cavity. We also show that the temperature and pressure perturbations were suppressed to below the thermal noise limit. By locking the laser to this high finesse cavity, we show that the free running diode laser noise is suppressed also below the thermal noise level of the cavity. We show as well the intensity stabilization performance and passive residual amplitude modulation suppression, and an evaluation of their effect on the final cavity performance.

- Chapter 5: The performance of the laser stabilized to the 39.5 cm long cavity is measured and presented in this chapter. To perform this measurement the laser is transferred via a 350 m stabilized fiber to be compared to two different stable lasers, present at PTB, and operating at different wavelengths. The frequency comparison is performed via a frequency comb. In this chapter we show the technique used for stabilizing the fiber link. The frequency stability comparison of lasers with different wavelengths via a frequency comb is then outlined. A fractional frequency instability of 1.1×10^{-15} for an averaging time between 2 s and 200 s was obtained for our system. A discussion of the limits of the ultimate performance of the cavity is presented at the end of this chapter.

- Chapter 6: The summary and outlook chapter gives a general overview about the obtained theoretical and experimental results, and an outlook of steps that we intend to take in order to improve the current performance of the laser stabilization.

Chapter 2

Concept of a stable optical local oscillator

Frequency stabilized laser sources are a key feature of fundamental physics experiments, particularly in the field of frequency standards. Optical frequency metrology improves in terms of stability essentially by improving the stability of the local oscillator (laser) used for probing the atomic reference. Nowadays, frequency stabilization techniques are based on the comparison of the laser frequency to external stable reference frequencies, such as from spectral hole burning in cryogenically cooled crystals (i.e. Tm^{3+}:$Y_3Al_5O_12$ or Eu^{3+}:Y_2SiO_5) [34, 35] or from an atomic or molecular absorption line (i.e iodine) [36, 37]. More commonly used in optical frequency standards is laser frequency stabilization to a passive optical cavity; the stability of the cavity optical path length is transferred to stabilize the laser frequency.

In this chapter we consider laser frequency stabilization to a cavity (etalon) of perfectly constant length. We will start by explaining how we characterize the laser frequency instability using Allan deviation and classify the different types of noise. In the second part we describe the single ion Al^+ frequency standard and the effect of laser instability on the clock performance. In the third part we first present a brief review of the relevant properties for our study of a Fabry-Perot (FP) cavity, then we present the Pound-Driver-Hall technique used for locking the laser frequency to an optical resonance of the optical cavity.

2.1 Evaluation of frequency instability: Allan deviation

The performance of a frequency standard is evaluated from the stability of the local oscillator (laser). A common technique for describing frequency fluctuations and characterizing the stability of the local oscillator consists of calculating the Allan variance $\sigma_y^2(\tau)$ as a function of the measurement time τ [19]. $\sigma_y(\tau)$ is called the Allan deviation.

Consider the evolution of the frequency over time, $\nu(t)$, measured using a frequency counter that gives, for every data point, a frequency average $\bar{\nu}_n$ over a sampling time (gating time) τ as:

$$\bar{\nu}_n = \frac{1}{\tau} \int_{t_n}^{t_n+\tau} \nu(t)dt. \tag{2.1}$$

Taking the standard deviation of N data points for different values of τ can give information about the long term drifts of the laser frequency, but will conceal information about frequency

fluctuations that happen within different averaging times, and thus lose essential information for the study of the frequency instability and its origins. The Allan deviation method consists of taking the differences between adjacent data points, thus giving integration time resolved measurements of frequency fluctuations. The Allan deviation with different integration times of the frequency instability is calculated as:

$$\sigma_\nu(\tau) = \sqrt{\frac{1}{2(N-1)} \sum_{n=1}^{N-1} (\bar{\nu}_{n+1} - \bar{\nu}_n)}. \tag{2.2}$$

A meticulous theoretical study of this method can be found in [19].

The Allan deviation can be expressed for the fractional (normalized) frequency instability $\sigma_y(\tau)$ and we have:

$$\sigma_y(\tau) = \frac{\sigma_\nu(\tau)}{\nu_0}, \tag{2.3}$$

where ν_0 is the frequency of the local oscillator. In practice, we choose the minimum averaging time τ depending on the type of noise we would like to identify. For example, we choose the integration time in the frequency counter of a beat-note signal between two oscillators to be as small as possible (e.g. 100 ms) to be able to identify noise at short time scales, and we take long intervals (e.g. 5 s) for low frequency noise (e.g. temperature fluctuation).

It is also possible to calculate the Allan deviation from a noise spectrum if this spectrum is measured. This is useful, for example, to characterize the contribution of different noise sources to the fractional frequency instability. Consider the power spectral density (PSD) $S_\nu(f)$, the Fourier transform of the autocorrelation function of the frequency excursion $\Delta\nu(t) = \nu(t) - \nu_0 \ll \nu_0$, where $\nu(t)$ is the instantaneous frequency at time t and ν_0 is the mean frequency of the oscillator. It is transformed into the PSD of the fractional frequency fluctuation $S_y(f)$ via normalization as:

$$S_y(f) = \frac{1}{\nu_0^2} S_\nu(f) \tag{2.4}$$

with f the Fourier frequency, and the unit of $S_y(f)$ is [Hz^2/Hz]. The PSD of the fractional frequency fluctuation can also be obtained from the phase fluctuation of the oscillator $\Delta\phi(t)$ with $\Delta\nu(t) = \frac{1}{2\pi}\frac{d\Delta\phi(t)}{dt}$, resulting in:

$$S_y(f) = \frac{f^2}{\nu_0^2} S_\phi(f) \tag{2.5}$$

where the unit of $S_\phi(f)$ is [rad^2/Hz].

It is often possible to classify $S_y(f)$ into known noise models that are functions of the Fourier frequency to the power of an integer α:

$$S_y(f) = \sum_{\alpha=-2}^{2} h_\alpha f^\alpha. \tag{2.6}$$

Noise type	$S_y(f)$	$S_\phi(f)$	$\sigma_y^2(\tau)$	$Mod\ \sigma_y^2(\tau)$	Possible sources
Random walk FN	$h_{-2}f^{-2}$, $f_h \to \infty$	$v_0^2 h_{-2}f^{-4}$	$(2\pi^2 h_{-2}/3)\tau^{+1}$	$\propto \tau^{+1}$	physical environment (mechanical shock / vibration, temperature fluctuation)
Flicker FN	$h_{-1}f^{-1}$, $f_h \to \infty$	$v_0^2 h_{-1}f^{-3}$	$2h_{-1}\ln 2\tau^0$	$\propto \tau^0$	resonance mechanism of an active oscillator, thermal noise (Brownian motion), electronics, or environmental conditions
White FN	$h_0 f^0$, $f_h \to \infty$	$v_0^2 h_0 f^{-2}$	$(h_0/2)\tau^{-1}$	$\propto \tau^{-1}$	shot noise (Quantum projection noise), Johnson-Nyquist (thermal) noise, Schawlow-Townes noise (diode laser)
Flicker PhN	$h_1 f$, $f < f_h$	$v_0^2 h_1 f^{-1}$	$\frac{h_1 1.038+3\ln(2\pi f_h\tau)}{(4\pi^2)\tau^2}$	$\propto \tau^{-2}$	phase noise from fiber link, electronic components (electronic amplifiers, frequency multipliers), frequency sources
White PhN	$h_2 f^2$, $f < f_h$	$v_0^2 h_2 f^0$	$[3h_2 f_h/(4\pi^2)]\tau^{-2}$	$\propto \tau^{-3}$	frequency generator or sources, electronic amplifiers

Table 2.1: Power spectral density of fractional frequency fluctuation converted into Allan variance $\sigma_y^2(\tau)$ and the modified Allan variance Mod $\sigma_y^2(\tau)$ [19]. PhN denotes phase noise and FN denotes frequency noise. f_h is the cut-off frequency of the measurement system bandwidth where $2\pi f_h \tau \gg 1$. Possible sources of the different noises in the scheme of a laser stabilized to a passive resonator are mentioned.

In Tab. 2.1, we cite the most common noise types and some of their possible sources in the case of an oscillator [19]. The conversion from the power spectral density (frequency domain) to the Allan variance (time domain) is performed by [38]:

$$\sigma_y^2(\tau) = 2\int_0^\infty S_y(f)\frac{\sin(\pi\tau f)^4}{(\pi\tau f)^4}df. \tag{2.7}$$

By considering the Allan deviation behaviour, one can identify the dominant noise mechanisms in the system. However, it can be that the PSD of different noises present the same Allan deviation behaviour: such is the case for flicker phase noise and white phase noise at high Fourier frequencies. In this case, the modified Allan deviation is used:

$$\text{Mod}\ \sigma_y^2(\tau) = 2\int_0^\infty S_y(f)\frac{\sin(\pi\tau f)^6}{(\pi n\tau f)^2 \sin(\pi\tau_0 f)^2}df \tag{2.8}$$

where $\tau = n\tau_0$, and τ_0 is the minimum measurement interval, and n is the number of points averaged to obtain Mod $\sigma_y^2(\tau)$ in the limit that $2\pi f_h\tau_0 \gg 1$, as in Tab. 2.1.

It is important to note that the evaluation of instability $(\sigma_y^2(\tau))_{AB}$ of a system A is determined relative to the instability of a second system B and it is not possible to know which one of the two systems is limiting the comparison. Three oscillators need to be compared in order to determine the individual instability of each. This is performed using the three pair-comparisons or the three-cornered-hat technique [39]. The principle is illustrated in Fig. 2.1. Considering the oscillators A, B, and C, the individual instabilities can be deduced by compar-
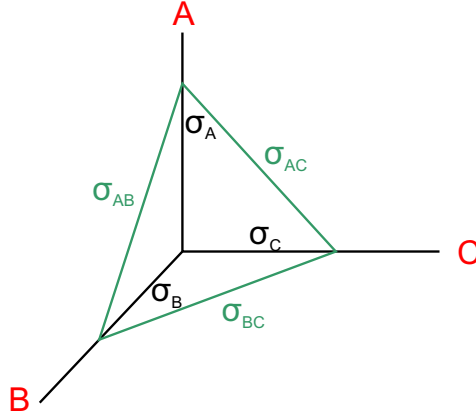
Figure 2.1: Three-cornered hat.

ing them pair by pair giving:

$$(\sigma_y^2(\tau))_A = \frac{1}{2}((\sigma_y^2(\tau))_{AB} + (\sigma_y^2(\tau))_{AC} - (\sigma_y^2(\tau))_{BC})$$

$$(\sigma_y^2(\tau))_B = \frac{1}{2}((\sigma_y^2(\tau))_{BA} + (\sigma_y^2(\tau))_{BC} - (\sigma_y^2(\tau))_{AC}) \tag{2.9}$$

$$(\sigma_y^2(\tau))_C = \frac{1}{2}((\sigma_y^2(\tau))_{CA} + (\sigma_y^2(\tau))_{CB} - (\sigma_y^2(\tau))_{AB})$$

However, this technique is only valid for completely independent oscillators. There exist different mathematical models for calculating the individual stabilities of N oscillators with and without assumption of correlation of the noises between them [40–43].

In a frequency standard experiment, characterizing the laser fractional frequency instability using Allan deviation is useful in determining the limiting noise in the overall performance of the frequency standard.

2.2 Relevance of laser instability for ion frequency standards

An optical frequency standard using a single trapped ion is based on the sequential interrogation of a dipole-forbidden optical transition in the electronic structure of the clock ion with a local oscillator (i.e. laser). The discriminant signal obtained from this interrogation is used in a feedback loop to control the laser frequency in order to lock it to the atomic resonance. A frequency comb is used as a frequency divider to enable counting the stabilized laser frequency. The stability and accuracy of the local oscillator thus represent the performance over time as

a frequency standard. The stability of a single ion clock is fundamentally limited by quantum projection noise (QPN) [44]: the randomness of single quantum jumps between ground and excited state per interrogation cycle, which averages down as the number of interrogations increases. However, a major limit on the frequency standard stability arises from the fact that the time of an interrogation cycle of the ion is limited by the coherence time of the local oscillator. In fact, during the time that the feedback signal to correct the laser frequency is absent (i.e. the time to prepare the ion for interrogations), the phase of the laser evolves randomly. For this reason the achievable clock performance depends on the laser noise. In order to understand the effect on a single ion frequency standard's stability, a brief introduction to the Al^+ ion clock and the effect of laser instability on its final performance are given.

In the Al^+ optical clock, the optical clock transition between the $^1S_0$ and $^3P_0$ states has a natural linewidth with $\Delta \nu_0 = 8$ mHz at $\nu_0 = 1.12 \times 10^{15}$ Hz corresponding to a transition wavelength of 267.4 nm [45]. The used laser light locked to the cavity has a 1069.6 nm wavelength, and is frequency-doubled twice before it is used for the clock transition interrogation. A simplified scheme of the Al^+ optical clock is presented in Fig. 2.2.

Consider the interrogation laser of linewidth Γ_L, with a white frequency noise. In the case of a narrow linewidth where $\Delta \nu_L \ll \Delta \nu_0$, the QPN limited stability is determined by the signal-to-noise ratio (SNR), and by the quality factor of the atomic transition $Q = \frac{\nu_0}{\Delta \nu_0}$. The QPN can be expressed in terms of the Allan deviation of the ion detection noise $\sigma_{y,ion}$ over an averaging time τ by:

$$\sigma_{y,ion} = \frac{C}{\text{SNR}} \frac{1}{Q} \sqrt{\frac{t_c}{\tau}} \approx \frac{\Delta \nu_0}{\nu_0} \sqrt{\frac{t_c}{\tau}} \qquad (2.10)$$

where $t_c = T + t_d$ is the duration of one interrogation cycle where T is the probe time, and t_d is dead time (needed for the preparation and detection of the ion). C is a numerical constant of order unity. The SNR measured for a single ion is equal to one, and $C/\text{SNR} \approx 1$. Several studies of the optimum feedback strategies for interrogating an ion clock [46, 47] show that, for the Al^+ clock where $t_c \approx T$, a fundamental instability limit of $\sigma_{y,ion} \approx 8.2 \times 10^{-17}/\sqrt{\tau/s}$ is feasible by applying a Ramsey excitation scheme to the ion while $\sigma_{y,ion} \approx 1.1 \times 10^{-16}/\sqrt{\tau/s}$ is feasible by applying a Rabi excitation scheme.

For a resolved laser linewidth $\Delta \nu_L$ on the the order of the natural linewidth $\Delta \nu_0$ of the Al^+ clock transition, the difference between the Ramsey and Rabi excitation methods is less pronounced and the Allan deviation of the frequency standard can be approximated to:

$$\sigma_{y,ion}(\tau) \approx 2 \frac{\Delta \nu_L}{\nu_0} \sqrt{\frac{1}{2\pi \Delta \nu_0 \tau}}, \qquad (2.11)$$

where $\sigma_{y,ion}(\tau) \approx 1 \times 10^{-16}/\sqrt{\tau/s}$ using a Ramsey excitation scheme and $\sigma_{y,ion}(\tau) \approx 1.2 \times 10^{-16}/\sqrt{\tau/s}$ using a Rabi excitation scheme [46, 47]. This means that the Al^+ frequency standard instability can reach 10^{-18} in about 1 hour of averaging time when $\Delta \nu_L \approx 8$ mHz. This assumes a laser short term instability during the interrogation time of $\sigma_{y,L} = \Delta \nu_L/\nu_0 \leq 1 \times 10^{-17}$.

In the case of a broad laser linewidth of $\Delta \nu_L > \Delta \nu_0$ (non-resolved transition), one must shorten the ion probe time T to $T < 1/2\pi \Delta \nu_L$ in order to adjust the Fourier transform limit

to the laser linewidth [46]. The clock instability after one interrogation cycle scales as $1/T$, whereas the instability averages as $\sigma_y(\tau) \propto \frac{1}{T}\sqrt{t_c/\tau}$. Since $t_c \approx T$, the clock instability is proportional to $1/(\sqrt{T\tau})$, thus proportional to $\sqrt{\Delta\nu_L/\tau}$.

The stability of a laser locked to an ultra-stable passive cavity is fundamentally limited by the thermal noise of the cavity (see Chap. 3) which is a flicker frequency noise. In this study, we show that with a proper choice of the reference cavity, the Allan deviation of the cavity thermal noise limit can reach $\sigma_{y,L} \approx 7 \times 10^{-17}$, thus providing an average frequency fluctuation from 1 s to the next on the order of 20 mHz at 1070 nm. This laser performance results in $\Delta\nu_L \approx 80$ mHz at 267 nm, which means that the Al$^+$ frequency standard will reach an instability level of 1×10^{-18} in about 24 hours of averaging time.
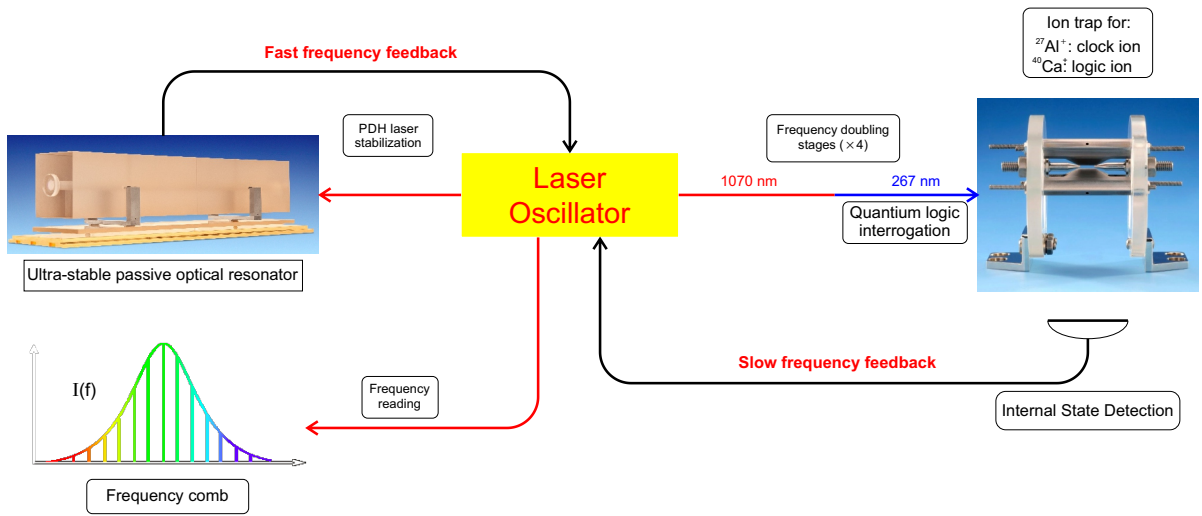
Figure 2.2: Principle of the Al$^+$ frequency standard. The interrogation of the Al$^+$ ion is based on the quantum logic spectroscopy of the 267.4 nm clock transition [6] using Ca$^+$ as logic ion [32]. The Pound Drever Hall (PDH) laser stabilization to the passive optical cavity and the fast feedback loop form the short term stabilization of the laser. The quantum logic interrogation of the Al$^+$ clock transition and the slow frequency feedback form the long term stabilization of the laser. The frequency reading is done via a frequency comb making the frequency countable [48].

2.3   Theory of an optical resonator

Fabry-Perot cavity

The basic theory of the Fabry-Perot (FP) interferometer has been developed and cited in different optics references [49–51]. In this section we recall the relevant theoretical background for our study of laser stabilization to a FP etalon. We consider an optical resonator made of two flat mirrors $M_{i \in \{1,2\}}$ with the corresponding amplitude reflection and amplitude transmission coefficients r_i and t_i respectively, separated by the optical path length of the cavity L as shown in Fig. 2.3. We consider an incident monochromatic electromagnetic beam
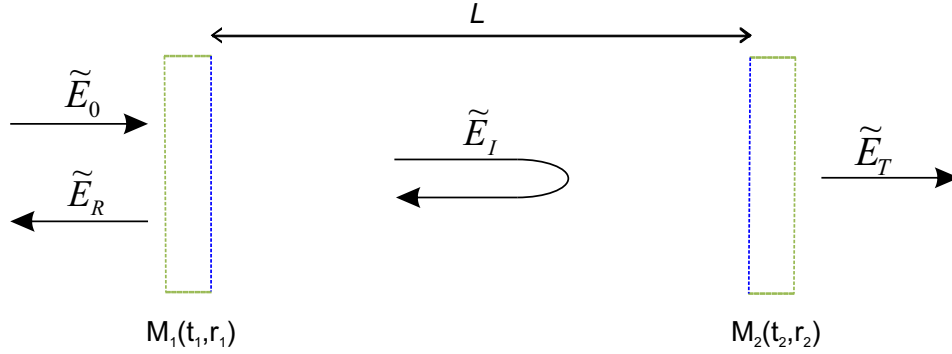
Figure 2.3: Illustration of a FP resonator of length L made of two flat mirrors $M_{i\in\{1,2\}}$ with the corresponding amplitude reflection and transmission coefficients r_i and t_i respectively. $\tilde{E}_0$ symbolizes the incident electromagnetic field, $\tilde{E}_I$ is the internal field, $\tilde{E}_T$ is the transmitted field and $\tilde{E}_R$ is the reflected field.

$\tilde{E}_0 = E_0 \exp(\iota(\omega t - \vec{k}.\vec{r}))$ of frequency ω, where $\vec{r}$ is the position vector and $\vec{k}$ wavevector where $|\vec{k}| = k = 2\pi/\lambda = \omega/c$, and λ is the laser wavelength. This laser is propagating toward the first mirror and normal to it. Assuming that the laser phase $\vec{k}.\vec{r} = 0$ at the surface of the first mirror. and a perfect mode coupling to the cavity, the beam will penetrate the cavity, make several round trips inside the resonator and accumulate in each trip a phase factor of $\Delta\phi = \exp(-\iota\omega \cdot \frac{2L}{c})$, with c being the speed of light, and λ being the laser wavelength. The complex amplitude of the electromagnetic field $\tilde{E}_I$ confined inside the cavity has the following expression :

$$\tilde{E}_I = t_1 E_0 \sum_{n=o}^{\infty} (r_1 r_2 \exp(-\iota\omega 2L/c))^n = \frac{t_1 E_0}{1 - r_1 r_2 \exp(-\iota\omega 2L/c)}. \tag{2.12}$$

The constructive interference inside the cavity will result in a transmitted beam. The expression is then calculated from the internal field as:

$$\tilde{E}_T = \tilde{E}_I \exp(-\iota\omega L/c)t_2 = E_0 \frac{t_1 t_2 \exp(-\iota\omega L/c)}{1 - r_1 r_2 \exp(-\iota\omega 2L/c)}. \tag{2.13}$$

From Eq.2.13 one can calculate the well known expression of the transmitted electromagnetic field intensity from a FP cavity:

$$I_T \simeq \tilde{E}_T \tilde{E}_T^* = E_0^2 \frac{t_1^2 t_2^2}{1 + r_1^2 r_2^2 - 2r_1 r_2 \cos(\omega 2L/c)} \tag{2.14}$$

that represents an Airy function with maxima at $\omega_q = qc/2L$, where q is an integer.

The frequency separation between two peaks of the Airy function is one characteristic of the FP cavity and is called the Free Spectral Range (FSR).

$$\Delta\omega_{\text{FSR}} = \omega_{q+1} - \omega_q = \frac{c}{2L}. \tag{2.15}$$

One free spectral range corresponds to a phase shift between two transmitted electromagnetic fields of $\Delta\phi = 2\pi$. It is also the inverse of one round trip travel time of a photon inside the cavity.

The full width at half maximum of the Airy peaks represents the linewidth of the cavity and is given by:

$$\Gamma = \frac{c}{2L}\frac{(1 - r_1 r_2)}{\pi\sqrt{r_1 r_2}}. \tag{2.16}$$

It corresponds to the inverse of the lifetime of the photon inside the cavity. The free spectral range $\Delta\omega_{FSR}$ normalised to the linewidth of the cavity Γ is another important characteristic of the optical cavity, the cavity finesse:

$$\mathscr{F} = \frac{\Delta\omega_{FSR}}{\Gamma} = \frac{\pi\sqrt{r_1 r_2}}{1 - r_1 r_2}, \tag{2.17}$$

that can be approximated to $\pi/(1 - r_1 r_2)$ for highly reflective mirrors. For a high finesse cavity, and for a laser frequency ω close to the cavity resonance frequency ω_q one can write the transmitted intensity as a Lorentzian function of ω, ω_q and the cavity linewidth Γ:

$$I_T = \frac{I_{max}}{1 + \frac{4}{\Gamma^2}(\omega - \omega_q)^2} \tag{2.18}$$

with $I_{max} = \frac{1}{2}\varepsilon_0 c(E_0 t_1 t_2/(1 - r_1^2 r_2^2))^2$ as the maximum transmitted intensity for a lossless cavity, with ε_0 is the vacuum permittivity and c is the speed of light. This means that for a high finesse cavity the transmitted peaks are narrow compared to the cavity FSR, and thus the Fabry-Perot etalon can be used as a narrow optical filter. The normalized I_T is plotted as a function of the laser frequency detuning from the cavity resonance $\Delta = \omega - \omega_q$ in Fig. 2.4(a).

The reflected electromagnetic field $\tilde{E}_R$ from the optical cavity is a coherent sum of the beam that gets reflected without entering the cavity and a beam that leaks out of the cavity from M_1:

$$\tilde{E}_R = -r_1 E_0 + E_0 \frac{t_1^2 r_2 \exp(-\iota\omega 2L/c)}{1 - r_1 r_2 \exp(-\iota\omega 2L/c)}. \tag{2.19}$$

Close to the cavity resonance, the two fields contributing to $\tilde{E}_R$ have about the same amplitude, but they are out of phase by π when the cavity is perfectly resonant. As a consequence, the two parts destructively interfere and no light is reflected from the cavity. However, the relative phase between the two beams will depend strongly on the frequency of the laser beam [19].

For a symmetric ($r_1 = r_2 = r$ and $t_1 = t_2 = t$) and lossless cavity ($r^2 + t^2 = 1$) cavity, the reflection coefficient is written :

$$R(\omega) = \frac{\tilde{E}_R}{\tilde{E}_0} = r\frac{1 - \exp(-\iota\omega 2L/c)}{1 - r^2 \exp(-\iota\omega 2L/c)}. \tag{2.20}$$

In this case, one can see that the reflected wave has a minimum at $\omega 2L/c = 2\pi$. In Fig. 2.4, we plot the normalized intensity (b) and the phase (c) of $R(\Delta = \omega - \omega_q)$. The model of a planar-mirror resonator described above is useful for introducing a FP cavity. However in practice, it
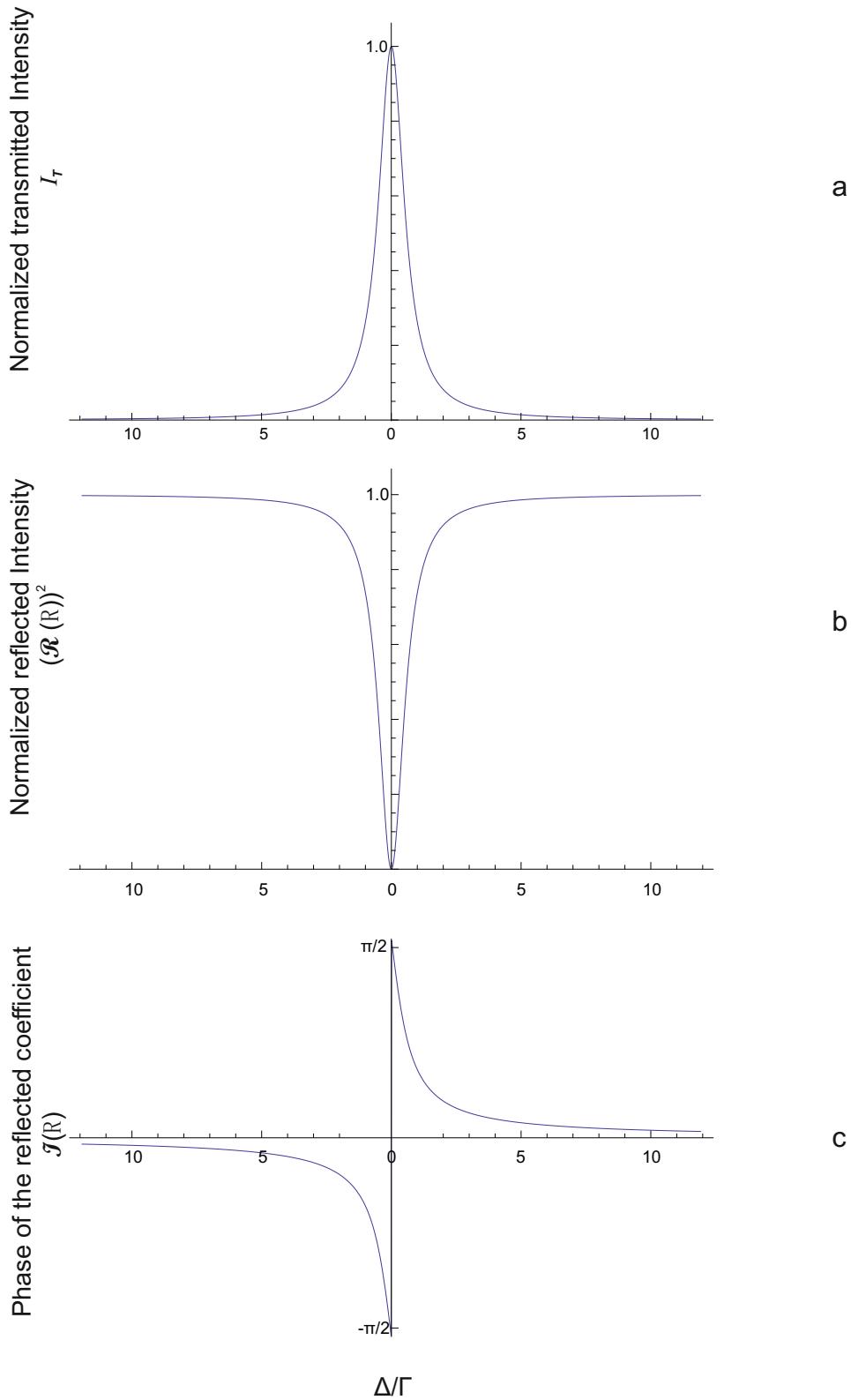
Figure 2.4: Signals from Fabry Perot cavity of finesse $\mathscr{F} = 1000$, and length $L = 39.5$ cm. (a) Transmitted intensity I_T from a FP cavity as in Eq. 2.14. (b) and (c) are the normalized intensity and the phase of the reflection field $R(\omega)$, respectively, as in Eq. 2.20.

is highly sensitive to misalignment[1] and thus the field can not be confined successfully between the mirrors. For stable operation, at least one of the mirrors should have a curvature.

Spectral characterization of an optical cavity
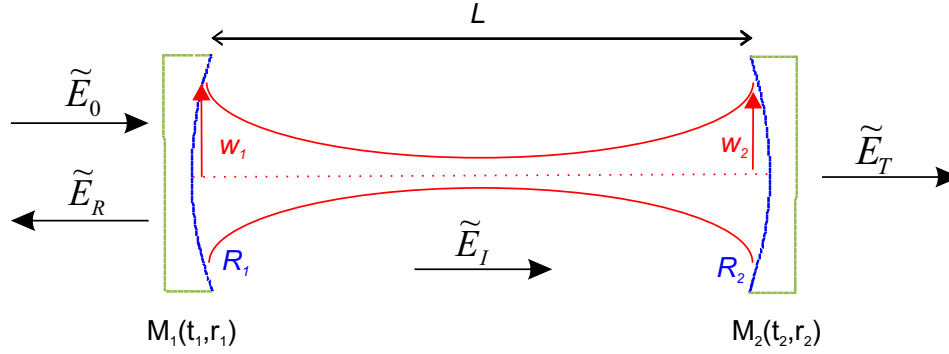
Figure 2.5: Illustration of an optical resonator of length L made of two mirrors $M_{i\in\{1,2\}}$ with radius of curvature R_i and with the corresponding amplitude reflection and transmission coefficients r_i and t_i respectively. $\tilde{E}_0$ symbolizes the incident electromagnetic field, $\tilde{E}_I$ is the internal field, $\tilde{E}_T$ is the transmitted field and $\tilde{E}_R$ is the reflected field. w_1 and w_2 are the beam radii of the Gaussian beam at the mirror inner surface.

We recall the expression for the Gaussian beam [50] inside the optical cavity and the different optical modes. This will give an important characterization of the type of the cavity, its spectral properties, and its stability. Consider an optical resonator made of two mirrors $M_{i\in\{1,2\}}$ with the corresponding radii of curvature R_i and separated by L as in Fig. 2.5. The confinement of a Gaussian beam inside the cavity requires the wavefront curvatures of the beam to match the mirror radii. Using the propagation law for a Gaussian beam, we find the beam radii ($1/e^2$ of the laser intensity) at the mirror reflecting surfaces to be:

$$w_1 = \sqrt{\frac{L\lambda}{\pi}} \cdot \left[\frac{g_2}{g_1(1-g_1g_2)}\right]^{1/4} \qquad (2.21)$$

for mirror M_1 and

$$w_2 = \sqrt{\frac{L\lambda}{\pi}} \cdot \left[\frac{g_1}{g_2(1-g_1g_2)}\right]^{1/4} \qquad (2.22)$$

for mirror M_2, where $g_i = 1 - \frac{L}{R_i}$ are the so called stability parameters. Thus, for a real and positive spot size on the mirrors, the product g_1g_2 must satisfy the stability condition:

$$0 \leq g_1g_2 \leq 1. \qquad (2.23)$$

---

[1]This model is physically meaningful if the mirrors have infinite extend with respect to the laser beam that should in turn be a perfect plane wave.

In other terms, the Gaussian beam can form optical modes inside a stable resonator if the condition of Eq. 2.23 is satisfied. Otherwise, the resonator is considered unstable. We have seen in Eq. 2.15 the resonance condition that gives the spacing $\Delta\omega_{FSR}$ between the different modes, called axial modes or fundamental modes of the optical cavity with frequencies $\omega_q = \omega_{00q}$. With every axial mode, we have a number of transversal mode frequencies ω_{nmq} (with indices nmq with q fixed), also called higher order modes:

$$\omega_{nmq} = \frac{c}{2L}\left(q + (n+m+1)\frac{\arccos\sqrt{g_1 g_2}}{\pi}\right) \qquad (2.24)$$

and

$$\Delta\omega_{hom} = \omega_{(n+1)mq} - \omega_{nmq} = \omega_{n(m+1)q} - \omega_{nmq} = \frac{c}{2L}\left(\frac{\arccos\sqrt{g_1 g_2}}{\pi}\right). \qquad (2.25)$$

The higher order mode spacing $\Delta\omega_{hom}$ corresponds to a Gouy phase shift [50] accumulated per round trip of the Gaussian beam inside the cavity and we can then write:

$$\omega_{nmq} = \frac{c}{2L} + q\Delta\omega_{FSR} + (n+m)\Delta\omega_{hom}. \qquad (2.26)$$

We note that, for a fixed q, all higher order modes with $n+m$ equal to the same constant are degenerate (i.e. $\omega_{11q} = \omega_{02q} = \omega_{20q}$)[2]. A wide range of configurations of g_1 and g_2 can form a stable cavity, but for our study, we will focus in Chapter 3 on two particular configurations close to the boundaries of the stability condition imposed by Eq. 2.23. For a symmetric cavity with $R_1 = R_2 = R$, The two configurations close to instability are the near-planar ($R \gg L$, $g_i \approx 1$) and the near-concentric ($R \approx L/2$, $g_i \approx -1$).

The near-planar configuration is characterized by a large spot size on the mirrors, and the beam waist is almost constant along the cavity. In this case, the beam divergence is very small, but since the cavity is close to instability, it is particulary sensitive to angular misalignment of the mirrors (See Section 3.2.2). When we look at the frequency spectrum for such a cavity, using Eq.2.25, we find that:

$$\Delta\omega_{hom\ (near-planar)} = \Delta\omega_{FSR}(\frac{1}{\pi}\sqrt{\frac{2L}{R}}) \ll \Delta\omega_{FSR}, \qquad (2.27)$$

which means that the higher order modes shift close to the fundamental modes of the cavity. This can be a limitation for stabilizing a laser to the cavity, as we will see in the next chapter (See Section 3.2).

The near-concentric configuration has also the advantage of a large spot size on the mirrors, but the waist at the center of the cavity becomes very small. In this case the beam divergence is very large in addition to the high sensitivity to mirror misalignment, and we write:

$$\Delta\omega_{hom\ (near-concentric)} = \Delta\omega_{FSR}(1 - \frac{2}{\pi}\sqrt{\frac{\varepsilon}{R}}), \qquad (2.28)$$

---

[2]Assuming mirrors with cylindrical symmetry. If the mirrors were astigmatic then the transverse modes would not be degenerate.

with $\varepsilon = L - 2R \gtrsim 0$. This means that the higher order mode spacing is almost as big as the axial mode spacing which makes the higher order modes near-degenerate with the fundamental ($\omega_{01q} = \omega_{10q}$ approaching $\omega_{00(q+1)}$). This spacing can also affect the laser stabilization as we will discuss in the next chapter (See Section 3.2).

2.4 Introduction to the Pound Drever Hall technique

The stability of a passive optical cavity is typically transferred to a laser frequency using the Pound Drever Hall (PDH) technique [27]. It is based on a measurement of the dispersive response of the cavity as a function of laser detuning from cavity resonance [19,52]. Figure 2.6
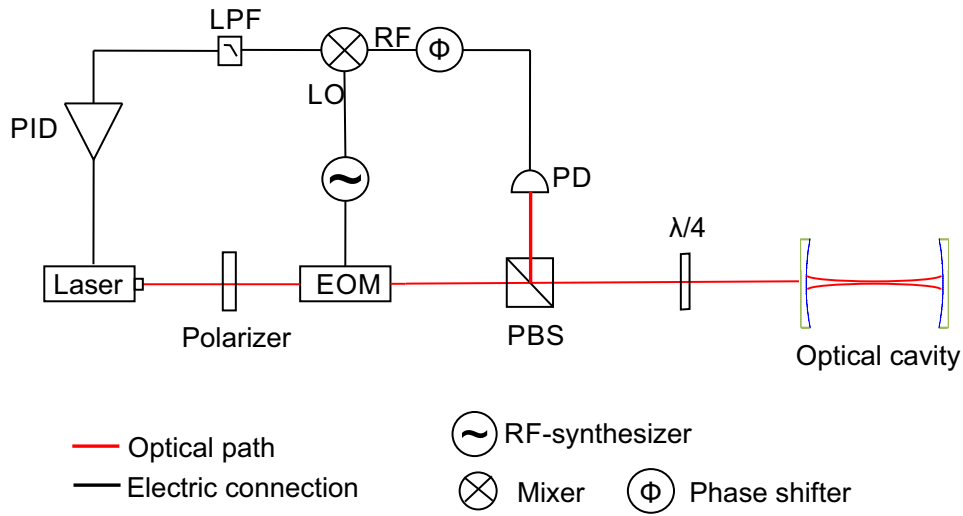
Figure 2.6: Optical set-up of a PDH stabilization scheme. PD: Photo-diode of the PDH detection, LPF: Low-pass-filter. LO is the local oscillator signal from the RF-synthesizer driving the EOM and RF is the AC-signal from the PD. A phase shifter is used to compensate for the phase difference between the RF and LO signals. PID: Proportional+Integral+Differential servo, EOM: electro-optical modulator. PBS: polarized beam splitter, and $\lambda/4$: quarter wave-plate.

illustrates the optical set-up of a PDH stabilization scheme. Consider a cavity with resonance frequency $\omega_{00q} = 2\pi\nu_0$, and a free-running laser frequency $\omega = 2\pi\nu$, detuned from resonance by $\Delta = \nu - \nu_0$. We modulate the phase of the incident beam $\tilde{E}_0$ using an Electro-Optical Modulator (EOM) with modulation frequency Ω. The modulated incident beam will have modulation sidebands at $\pm n\Omega$ where n is the order of the sideband. The incident beam is then written using Bessel functions [52]:

$$\tilde{E}_0 = E_0 \exp(\imath\omega t)[J_0(\beta) + \sum_{n=1}^{\infty} J_n(\beta)\exp(\imath n\Omega t) + \sum_{n=1}^{\infty} (-1)^n J_n(\beta)\exp(-\imath n\Omega t)] \qquad (2.29)$$

with $J_n(\beta)$ being the nth order Bessel function of the first kind as a function of the modulation depth β.

The reflected signal from the cavity $\tilde{E}_R$ contains the carrier frequency plus the reflected modulation sidebands. The reflection function for a high finesse cavity (see Eq. 2.20) can be written as:

$$R(\Delta) = -\frac{\Delta(\Delta + \iota\Gamma/2)}{(\Gamma/2)^2 + \Delta^2} \tag{2.30}$$

where the magnitude can be approximated by a Lorentzian for $\Delta \ll \Delta\omega_{\text{FSR}}$. Taking into account the first and second modulation sidebands only ($\pm\Omega$ and $\pm2\Omega$) and using Eq. 2.30 for the corresponding frequencies, we get:

$$\begin{aligned}
\tilde{E}_R = E_0[&R(\Delta)J_0(\beta)\exp(\iota\Delta t) \\
&+ \sum_{n=1}^{\infty} R(\Delta + n\Omega)J_n(\beta)\exp(\iota(\omega + n\Omega)t) \\
&+ \sum_{n=1}^{\infty} (-1)^n R(\Delta - n\Omega)J_n(\beta)\exp(\iota(\omega - n\Omega)t)].
\end{aligned} \tag{2.31}$$

As seen in Fig. 2.4, the phase of the reflection function $R(\Delta)$ is strongly dependent on Δ. In the PDH technique, the error signal and thus the frequency shift are derived from the measurement of this phase. This is accomplished by relating the phase of the carrier to the two first order side bands contained in the beat signal of the reflected light. The expression of the reflected power is calculated including the interaction between different reflected fields (the carrier frequency and the first order modulation sidebands), to obtain the following analytical expression taking into account first order modulation sidebands only:

$$\begin{aligned}
P_{\text{ref}} = {}&P_c|R(\omega)|^2 + P_s(|R(\omega + \Omega)|^2 + |R(\omega - \Omega)|^2) \\
&+ 2P_0 J_0(\beta)J_1(\beta)\{\Re[R(\Delta)R^*(\Delta + \Omega) \\
&- R^*(\Delta)R(\Delta - \Omega)]\cos(\Omega t) \\
&+ \Im[R(\Delta)R^*(\Delta + \Omega) - R^*(\Delta)R(\Delta - \Omega)]\sin(\Omega t)\} \\
&+ \mathcal{O}(2\Omega).
\end{aligned} \tag{2.32}$$

Here, $P_c = P_0 J_0^2(\beta)$ and $P_s = P_0 J_1^2(\beta)$ are the amplitude of the reflected carrier and sidebands respectively, where $P_0 = \frac{1}{2}\varepsilon_0 c E_0^2 \simeq P_c + 2P_s$ is the total power in the incident beam[3], and $\Re$ and $\Im$ refers to the real and the imaginary part, respectively. In practice, the signal is demodulated through mixing with the local oscillator field $E_L \sim \sin(\Omega t + \varphi)$, where φ is the phase difference between the RF signal (from the PD) and the local oscillator, that will be compensated by a phase shifter in Fig. 2.6. It is then low pass filtered to recover the $\sin(\Omega t)$ term in Eq. 2.32, which is the error signal. For the common situation of a fast modulation frequency ($\Omega \gg \Gamma$), the error signal becomes:

$$\begin{aligned}
\varepsilon(\Delta) = -2P_0 J_0(\beta)J_1(\beta)\Im[&R(\Delta)R^*(\Delta + \Omega) \\
&- R^*(\Delta)R(\Delta - \Omega)]
\end{aligned} \tag{2.33}$$

A plot of the normalized error signal is shown in Fig. 2.7.

---

[3]We neglect the interference effects with higher order modulation sidebands for small modulation depth β

Close to the cavity resonance ($\Delta \ll \Gamma$), the second order terms in Ω in Eq. 2.33 are negligible and $[R(\Delta)R^*(\Delta + \Omega) - R^*(\Delta)R(\Delta - \Omega)] \approx -\imath 2\Im[R(\Delta)]$. We can approximate the error signal in this region with a linear function of the frequency shift $\delta\omega$, where the slope is called the frequency discriminant D, and write the near-resonance error signal as $\varepsilon_{NR} = D \times \delta\omega$ with:

$$D = -8P_0 J_0(\beta)J_1(\beta)\frac{1}{\Gamma}. \tag{2.34}$$
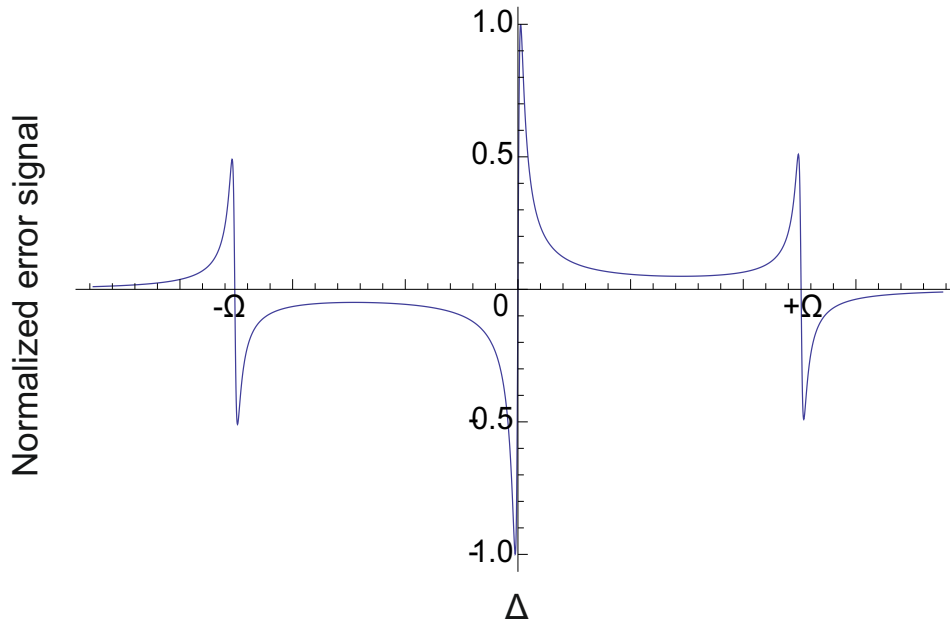
Figure 2.7: Illustration of a normalized error signal as in Eq. 2.33 as a function of the detuning Δ. Ω is the modulation frequency, $\beta = 1.08$, $\mathscr{F} = 1000$, $L = 39.5$ *cm*.

The PDH technique using a FP cavity transforms the frequency fluctuation into an electronic signal via the frequency discriminant D. The steepness of the slope and its magnitude will define how good the lock can be: steep and large in magnitude means more sensitivity to frequency fluctuation and thus better correction. To optimise the slope, we can conclude from Eq. 2.34 that the cavity linewidth Γ needs to be as narrow as possible, and that the optimum modulation depth corresponds to $\beta = 1.08$.

The expression for the discriminant in Eq. 2.34 is valid for frequencies below the bandwidth of the cavity ($|\Delta'| \le \Gamma/2$), but the PDH technique remains valid for higher detuning and is not limited by the cavity bandwidth. Oded Mor and Ady Arie show in [53] that for higher detunings, the expression for D becomes:

$$D_{LP}(\Delta') = \frac{D}{1 + \imath(\frac{2\Delta'}{\Gamma})} \tag{2.35}$$

where the discriminant D_{LP} functions as a first order low pass filter with the corner frequency being half the linewidth of the cavity. This filtering effect can be compensated by adding

a servo design such as a PID system (Proportional+Integral+Differential servo), which is a high-bandwidth low-noise electronic amplifier [53]. The transfer function of the servo is described in Sec. 4.2.2. To close the loop, the amplified and phase-compensated electronic error signal is fed back to a laser actuator to correct for the frequency noise. PDH is a powerful technique that is not limited by the bandwidth of the cavity. When the laser is in lock, the error signal is insensitive to first order to the modulation depth β, the modulation frequency Ω, and the laser intensity on the photodiode. Every element in the PDH stabilization loop (phase modulator, servo, actuator, etc.) can add noise that will contribute to an "effective" error signal and disturb the lock to the cavity. These effects will be discussed in Sec. 4.2.2 and Sec. 4.2.3. The performance is ideally limited by the shot noise of the detection photodiode as we will discuss in Sec. 4.2.2. We showed in this chapter the principle of stabilization a laser using the PDH technique to a passive optical resonator with a stable optical path length. In reality, the optical path length of the cavity is fundamentally not stable as we will show in next chapter and this will be the major practical limit of the laser stability.

Chapter 3

Reducing the effect of thermal noise

In a typical setup for optical frequency standards, the local oscillator source is a laser of frequency $\nu = \frac{c}{\lambda}$ where c is the speed of light and λ is the laser wavelength, which is stabilized to one of the modes of a linear Fabry-Pérot (FP) cavity (see Chap. 2). Several noise sources can change the optical path length L of the cavity. A small cavity length fluctuation $\Delta L \ll \lambda$ results in an undesirable frequency fluctuation $\Delta\nu$, related by:

$$\frac{\Delta L}{L} = -\frac{\Delta\nu}{\nu}. \tag{3.1}$$

Disturbances such as pressure and temperature fluctuations, as well as vibrations, can be reduced by placing the cavity in a vacuum chamber equipped with sufficient active and passive thermal control and careful isolation from mechanical and acoustic vibrations (see Chap. 4).

On a more fundamental level, thermal noise induces optical path length fluctuations [54]. Brownian motion causes local random displacements in the cavity spacer, mirror substrates and mirror coatings, limiting the achievable length stability of optical reference cavities. A theoretical description based on the Fluctuation Dissipation Theorem (FDT) indicates that the thermal noise strongly depends on material parameters, such as the mechanical loss angle (ϕ), and also on the size of the optical mode on the mirrors [55].

One of the dominant sources of thermal noise arises from the mirror coatings due to their high mechanical losses [28, 56]. Increasing the mode size of the beam on the mirror surface averages the thermal fluctuations over a larger surface and thus reduces the corresponding thermal noise contribution [57]. This can for example be achieved through the excitation of higher-order transverse modes [58]. In this chapter, we analyze the feasibility of two alternative approaches that increase the mode size on the mirrors. The first approach is based on cavities operated close to instability, i.e. with a near-planar or near-concentric mirror configuration (Sec 2.3), whereas the second relies on using long cavities. In the latter approach, relative frequency fluctuations are further suppressed since they scale with the inverse of the square root of the cavity length.

In the first section of this chapter we present a short overview of the analytical model of thermal noise and we give the results of finite element simulations of the frequency fluctuations in short and long cavities, with stable and near-unstable configurations. We show through simulations that a 10 cm long cavity, when operated near instability, can achieve a thermal-noise-limited instability of 1.5×10^{-16} in 1 s, whereas a 39.5 cm long cavity has the potential

to achieve an instability below 10^{-16} in 1 s. A major challenge for long cavities is meeting the required insensitivity to accelerations. We present a 39.5 cm long cavity design with a vibration sensitivity of the fractional length change of $< 10^{-10}$/g in all three directions, assuming realistic machining tolerances. In the second section we focus on the possible technical limitations of near-concentric and near-planar cavities arising from the dense mode structure that exists close to instability. We then estimate the alignment sensitivity of cavities operating close to instability. The third section focuses on the simulation results of the mechanical design of a vibration insensitive 39.5 cm long cavity.

Part of the work presented here has been published as Amairi *et al.*, (2013) [33].

3.1 Thermal noise theory in optical cavities

According to the the Fluctuation Dissipation Theorem (FDT), a non-zero temperature results in length fluctuations of the cavity body with random amplitudes proportional to the mechanical losses in the system [59, 60]. One can distinguish two sources of thermally-induced length changes in an optical cavity [57]. The first source is the Brownian motion of the particles within the system at a defined temperature. The second source is the thermoelastic noise that occurs due to the phase delay of the relaxation of thermal distributions in the body (thermodynamic fluctuations of temperature). The last effect is negligible compared to the Brownian noise in the cases we are treating of Fused Silica (FS) mirror substrates [61]. In this section we consider the Brownian thermal noise only.

3.1.1 Fluctuation Dissipation Theorem

The Fluctuation Dissipation Theorem (FDT) relates the thermal noise to unavoidable mechanical losses in the system [59, 60]. The resulting relative displacement noise amplitude $\sqrt{S_L}/L$ for a cavity is converted into fractional frequency noise by the relation 3.1 and we get:

$$\frac{\sqrt{S_L}}{L} = \frac{\sqrt{S_\nu}}{\nu}. \tag{3.2}$$

Numata *et al.* derived analytical expressions for the thermal noise contributions of different parts of the cavity system [28], that have been further improved by Kessler *et al.* [62]. The power spectral density of the displacement noise in a spacer of length L and mechanical loss ϕ_{spacer} can be written as:

$$S_{\text{spacer}}(\omega) = \frac{4k_B T}{\omega} \frac{L}{A\,E} \phi_{\text{spacer}}, \tag{3.3}$$

where k_B is the Boltzmann constant, ω is the angular noise frequency, T is the temperature, A is the end face area of the spacer excluding the center bore, and E is Young's modulus. The frequency noise from thermal noise of the spacer scales with the length as $1/\sqrt{L}$ as seen by combining Eq. 3.2 and 3.3.

The thermal noise from the mirror substrate can be derived by modelling it as an infinite half space, resulting in the following expression:

$$S_{\text{sub}}(\omega) = \frac{4k_B T}{\omega} \frac{1 - \sigma^2}{\sqrt{\pi E}} \frac{\phi_{\text{sub}}}{w}, \tag{3.4}$$

where σ is Poisson's ratio, w is the radius of the laser mode on the mirror, and ϕ_{sub} is the mechanical loss of the substrate.

For a coating of thickness d, the simplified expression of its thermal fluctuation spectrum is:

$$S_{\text{coat}}(\omega) = \frac{4k_B T}{\omega} \frac{2(1 + \sigma)(1 - 2\sigma)}{\pi E} \frac{d}{w^2} \phi_{\text{coat}}, \tag{3.5}$$

where ϕ_{coat} denotes the mechanical losses of a homogenous coating layer.

The dominant source of thermal noise for typical reference cavities arises from the mirror substrates and their coatings [28]. Choosing fused silica for the mirror material, with its one order of magnitude higher mechanical quality factor $Q = 1/\phi$ compared to ultra-low expansion glass, significantly reduces the thermal noise. Cavities made entirely of high mechanical Q materials, such as single-crystal silicon [63], have been investigated. This leaves the coatings on the cavity mirrors as the major contribution to the thermal noise owing to their more than two orders of magnitude larger mechanical losses compared to fused silica. The analytical expression in Eq. 3.5 suggests several options to reduce the coating thermal noise that have been experimentally investigated.

For example, decreasing the mechanical loss ϕ_{coat} by replacing the commonly employed amorphous SiO_2/Ta_2O_5 Bragg-reflector stacks by epitaxial $Al_xGa_{1-x}As$ distributed Bragg Reflectors coatings is a promising approach [64]. Recently, these crystalline coatings used in free-standing mechanical resonators have displayed an exceptional mechanical quality factor Q of up to 40,000 at room temperature and exhibited a finesse of about 150,000 at 1064 nm [65].

Other proposals suggest thermal noise compensated multi-layer coating designs [66, 67] that exploit the coherent character of stochastic displacement and correlated strains from the mirror coating and substrate.

Khalili suggested to reduce the thickness d of the coating and compensate the loss in reflectivity by adding another mirror behind the first [68, 69]. The two separated coating stacks form an etalon, which results in high reflectivity of the coating two-mirror system when tuned into anti-resonance, whereas the thermal noise is dominated by the first (thinner) coating, leading to a lower thermal noise compared to a single-mirror high-reflective coating.

Coating-free mirrors based on a surface nanostructure that creates a resonant surface wave-guide are yet another possibility [70]. However, the low experimentally achieved optical reflectivity and the difficulty of producing such mirrors with curvature, a requirement for stable optical cavities, currently limits their use for optical frequency metrology. We show in Appendix A results of the reflectivity of a micro-structured mirror that we measured with a tunable laser[1].

---

[1]Fabricated at Institut für Angewandte Physik Friedrich-Schiller-Universität in Jena, Germany.

3.1.2 Estimation of thermal noise for different cavities

Most experimentally realized stable cavity designs are hemispherical cavities using a flat mirror and a second mirror with 0.5 to 1 m radius of curvature. This configuration is well within the stability regime and the mode radius on the mirrors increases with cavity length. Moreover, according to Eq. 3.2, the fractional frequency noise decreases with increasing length of the cavity as $1/\sqrt{L}$ for the spacer contribution (See Eq. 3.3) and $1/L$ for the substrate and the coating contributions (Eq. 3.4 and 3.5). Consequently, the best thermal-noise-limited fractional instabilities of 2×10^{-16} and 1×10^{-16} were achieved for cavities 29 cm [29] and 40 cm [30] long, respectively.

However, according to Eqs. 3.4 and 3.5, the thermal noise contribution of the substrate and the coating scale with $1/w$ and $1/w^2$, respectively, which suggests to enlarge the TEM_{00} mode on the mirror surface. The radius of the optical mode on the mirror surfaces is a function of the distance between the mirrors and their radii of curvature as explained in Eq. 2.21 and 2.22. The two symmetric configurations close to instability for which the mode sizes on the mirrors increase considerably are the near-planar ($R \gg L$, $g_i \approx 1$) and the near-concentric ($R \approx L/2$, $g_i \approx -1$) configurations (See Sec 2.3). Both approaches for cavities with large mode field diameter pose different technical difficulties that will be addressed in sections 3.2 and 3.3.

In the following, we present numerical estimates of the thermal noise for various cavity geometries, in particular short near-planar cavities and long cavities, and compare them to existing systems. The calculations are based on a direct application of the FDT using Levin's theorem [55], implemented by Finite Element Simulations (FEM) using the commercial program Comsol Multiphysics [71]. The simulation is similar to the work presented in [62], except for the coating contribution to the thermal noise which was calculated using the analytical expression of Eq. 3.5.

Table 3.1 provides a summary of the estimated Allan deviation σ_ν (See 2.1) of the frequency (flicker) noise for 3 different geometrical cavity designs and lists the individual contributions from the spacer, the substrate, and the coating to the frequency instability. The relative frequency instability is calculated for the implemented or planned operating wavelength of the respective cavity. However, the selected wavelength plays only a minor role with longer wavelengths providing a slightly better performance due to a larger mode size on the mirrors. For cavities with coating-dominated thermal noise, doubling the wavelength also doubles the thickness of the required coating [72], leaving the overall noise contribution constant.

According to the table, the major contribution to thermal noise for all cases stems from the coated mirrors, which is in good agreement with the findings of reference [28] and the experimentally achieved thermal noise limits of 3×10^{-16} [26] and 6.7×10^{-16} [73] for (A) and (C), respectively. For the cavities with 24 cm length, replacing the ULE mirror substrates of case (A) by lower mechanical loss Fused Silica (FS) substrates would improve the frequency stability by a factor of two (case (B)).

The thermal-noise-limited performance of 10 cm long cavities is treated with plane/concave (C) and near-planar (D) mirror configurations. In case (D) the mode radius on the mirrors is increased to 766 μm, resulting in a reduction of the frequency instability by a factor of two compared to (C). It is remarkable that using an optical configuration near instability for a cavity of only 10 cm length provides a frequency stability comparable to the performance of a

Case	Substrate/Spacer	R_1/R_2	w (μm)	Frequency noise ($Hz/\sqrt{Hz}$) Relative contribution (%)			σ_y (10^{-16})	References to similar geometries
				Spacer	Substrate	Coating		
24 cm long cavities, λ=563 nm, d = 3 μm								
A	ULE / ULE	0.5m/∞	293/212	0.021	0.11	0.061	2.97	[26, 28]
				2 %	77 %	21 %		
B	FS / ULE	0.5m /∞	293/212	0.021	0.027	0.058	1.51	
				9 %	17 %	74 %		
10 cm long cavities, λ=1064 nm, d = 5.3 μm								
C	FS / ULE	0.5m/∞	260/291	0.023	0.033	0.087	4.05	[73, 74]
				6 %	12 %	82 %		
D	FS / ULE	30m/∞	767/766	0.023	0.020	0.031	1.85	
				28 %	21 %	51 %		
39.5 cm long cavities, λ=1069 nm, d = 6 μm								
E	FS / ULE	1m/∞	524/408	0.007	0.0064	0.014	0.72	
				17 %	14 %	69 %		
F	FS / ULE	0.2m/0.2m	778/778	0.007	0.0049	0.0083	0.50	
				35 %	17 %	48 %		

Table 3.1: Frequency noise calculation for different materials and cavities. The cavities have a cylindrical (A-D) or rectangular shape (E-F) operating with a laser at wavelength λ. The diameters of spacers of case (A-B), (C-D) and (E-F) are 150 mm, 100 mm and 74 mm respectively. The diameter of the spacer has a negligible influence on the total thermal noise. The optical mode radius w at the position of the mirror is a function of L and the mirror radius of curvature $R_{1,2}$. The relative frequency noise contribution of each component of the cavity is presented in addition to the calculated value of the total frequency noise $\sqrt{S_v(1\,\text{Hz})}$. σ_v is the fractional frequency instability with $\sigma_y = \sqrt{S_v(1\text{Hz})}\sqrt{2(\ln 2)}/v$. For all geometries, the central bore in the spacer is 1 cm diameter, the temperature is $T = 293$ K, $\phi_{\text{ULE}} = 1.6 \times 10^{-5}$ [75], $\phi_{\text{FS}} = 10^{-6}$ [76]. The coating on each mirror is of thickness d and $\phi_{\text{coat}} = 4 \times 10^{-4}$. We assume for ULE (Corning) a Young's modulus of 67.6 GPa and a Poisson ratio of 0.17 [75], and for FS a Young's modulus of 73.1 GPa and a Poisson ratio of 0.17 [76].

much longer cavity such as the 24 cm long cavity of case (B). This design is particularly attractive for applications requiring portable optical cavities [77–80]. Possible technical issues in the realization of such a cavity are discussed in section 3.2.

Cases (E) and (F) compare the improvement in frequency instability for a 39.5 cm long cavity when moving from a plane/concave (E) to a near-concentric (F) configuration. The long cavities result in improvements in the frequency stability by factors of 4 and 6 compared to case (A), while the improvement between the design of the stable plano-concave cavity (E) and the near-concentric cavity (F) is about 30 %. Recently, a cavity similar to case (E) has been implemented with a slightly different mirror configuration, demonstrating a thermal-noise-limited instability of 1×10^{-16} [30], similar to what we aim for in this work. When operated close to instability, both cavity geometries offer superior thermal-noise-limited performance compared to more stable geometries.

3.2 Cavities with large mode field diameter

As we have seen in Sec. 2.3, operating optical cavities close to instability results in an increased alignment sensitivity and a small frequency spacing between axial modes and higher order modes. The close spacing of higher-order modes can disturb the stabilization scheme of the resonance frequency. Furthermore, the cavity becomes sensitive to misalignment of the mirrors that can significantly shift the position and angle of the optical mode axis inside the cavity. This leads to an enhanced sensitivity to seismic and acoustic vibrations (see Sec 3.3).

For the remainder of this section, we consider cavities with higher-order mode spacing $\Delta\omega_{hom} = |\omega_{00q} - \omega_{01q}| \approx 2\pi \times 27$ MHz, corresponding to the cases (D) and (F) of Table 3.1.

3.2.1 Influence of higher-order modes on the error signal

We aim to perform laser stabilization to the optical cavity using the Pound Drever Hall (PDH) technique (See Chap. 2.4). Typically, higher-order modes are neglected in the error signal analysis. However, imperfect mode matching into the cavity can lead to non-negligible coupling to these modes. Off-resonant coupling of the laser to these modes can result in a small offset in the error signal of the fundamental mode. Beam pointing fluctuations will then lead to a fluctuation in the offset of the error signal and therefore instabilities in the laser frequency.

We investigated the two scenarios shown in Fig. 3.1: (A) off-resonant coupling of the first higher-order mode near the fundamental resonance interacting with the PDH modulation sidebands, and (B) near-coincidence of the fundamental resonance ω_{00q} with higher-order modes $\omega_{nmq\pm1}$ of a different longitudinal mode of the cavity. In both cases, by carefully choosing the length of the cavity, the ω_{00q}-resonance is made to lie close to the center between two higher-order modes to avoid PDH lock disturbance. The required length accuracy of the spacer of a cavity near instability ($g_i \approx \pm1$) can be estimated using:

$$\delta L \ll \Delta L_{hom} = \frac{\Delta\omega_{hom}^2}{\Delta\omega_{\text{FSR}} \times \xi},$$ (3.6)

where ΔL_{hom} is the required change in length to shift the resonance frequency ω_{00q} between
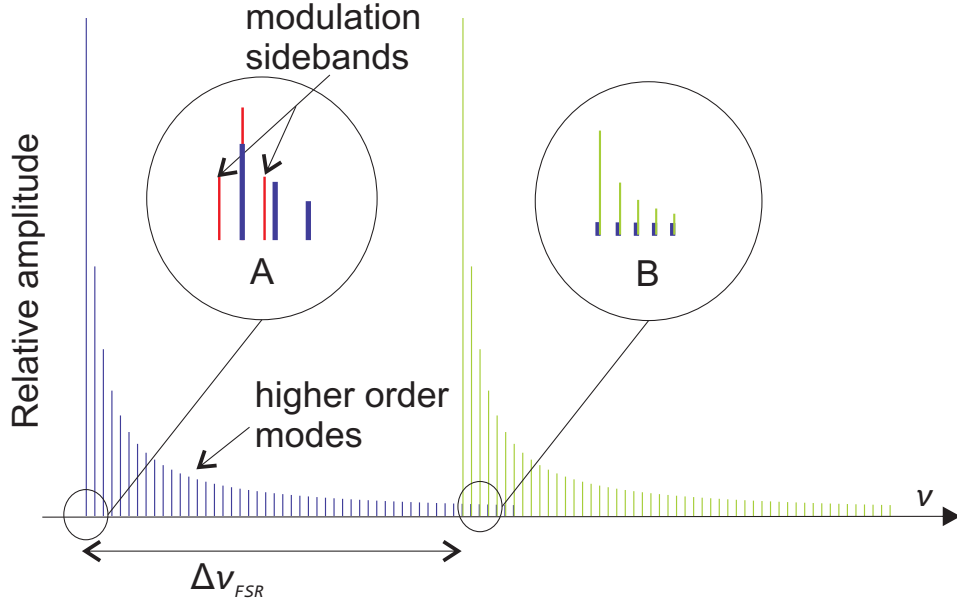
Figure 3.1: Example of two longitudinal modes (in green and blue) with higher-order mode distributions in a Fabry-Perot cavity of free spectral range $\Delta\omega_{\text{FSR}} = 2\pi \times 1.5$ GHz. For illustrative purposes, the relative amplitude of the TEM$_{mnq}$ modes is scaled according to $1/(m+n+1)$. Inset (A) depicts the interaction of higher-order modes with a spacing $\Delta\omega_{hom} = 2\pi \times 27$ MHz with the modulation sidebands at $\Omega = 2\pi \times 20$ MHz. Inset (B) illustrates the near-coincidence of the higher-order modes from a different longitudinal mode with the fundamental mode.
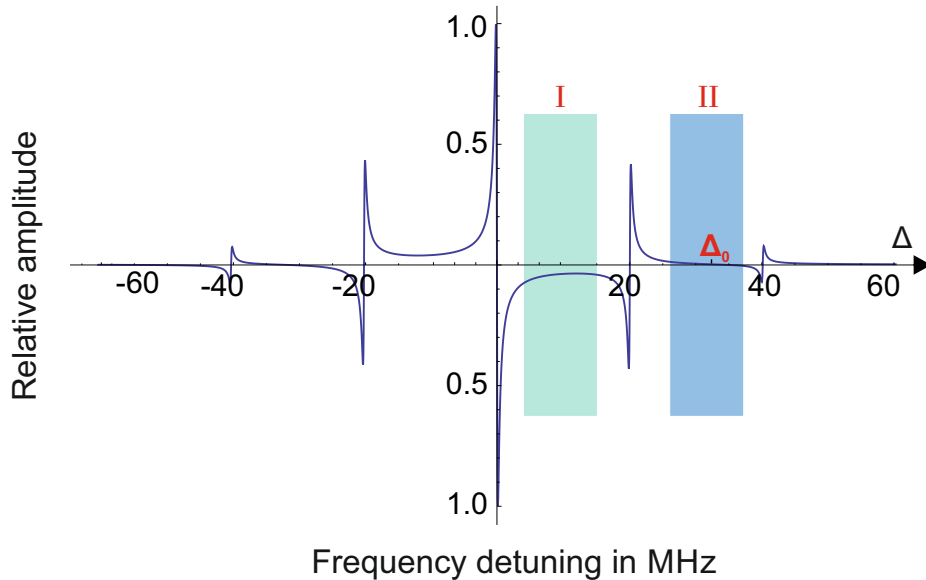
Figure 3.2: Error signal including first and second order modulation sidebands. The modulation frequency is $\Omega = 2\pi \times 20$ MHz, the modulation depth $\beta = 1$ and we assume for illustrative purposes a finesse of 5000. The green (I) and blue (II) regions are discussed in the text.

two neighboring higher order modes (i.e ω_{mnq-1} and $\omega_{mn+1q-1}$) and $\xi = \frac{\partial \Delta \omega_{hom}}{\partial L}$. For $\delta L = \Delta L_{hom}/10$, we estimate that δL for the 10 cm near-planar cavity [Table 3.1(D)] is on the order of 370 μm. This result is compared to the case of the near-concentric 39.5 cm long cavity [Table 3.1(F)] which has a similar higher order mode spacing and δL is on the order of 70 μm due to the smaller $\Delta \omega_{FSR}$. However, for the same cavity finesse, the long cavity has a narrower linewidth compared to the short one, which relaxes the tolerances on δL. For the short cavity, coincidences occur at very large mode indices due to its large free spectral range for which the coupling efficiency is expected to be small.

The effect of an off-resonant higher-order mode on the PDH error signal (case (A) of Fig. 3.1) is evaluated assuming a coupling efficiency $\eta_{hom} = 0.1$ of the laser beam to this first higher-order mode of the cavity. In addition, we assume this coupling to fluctuate by $\delta \eta_{hom}/\eta_{hom} = 10\%$ to estimate the frequency fluctuations. This represents a worst case scenario. A plot of the normalized error signal (See Eq. 2.33) to illustrate the different cases is shown in Fig. 3.2. The general expression of the frequency shift is obtained by dividing the offset contributed by the off-resonant higher order mode at detuning Δ, $\delta \eta_{hom} \cdot \varepsilon_{hom}(\Delta)$, by the frequency discriminant D from Eq. 2.34:

$$\delta \omega(\Delta) = \delta \eta_{hom} \cdot \frac{\varepsilon_{hom}(\Delta)}{D}. \tag{3.7}$$

To understand the effect of the higher-order mode, e.g. TEM_{010}, on the PDH error signal, we consider two possible cases.

The first case is for $\Gamma \ll \Delta \omega_{hom} < \Omega$ as shown in Fig. 3.2 by the green area around $\Delta \approx \Omega/2$. We recall that Γ is the linewidth of the cavity as in Eq. 2.16, and Ω is the modulation frequency. As an example, we use Eq. 3.7 to calculate the laser frequency deviation $\delta \omega(\frac{\Omega}{2})$ due to a distortion of the error signal by a higher-order mode situated at $\Delta = \frac{\Omega}{2}$ for a 10 cm long cavity with a finesse $\mathscr{F} = 10^5$, a modulation index of $\beta = 1$, and a modulation frequency of $\Omega = 2\pi \times 20$ MHz. In this case, the frequency fluctuation is estimated to be on the order of $\delta \omega(\frac{\Omega}{2}) = 2\pi \times 75$ mHz. This value is too large for operating a laser with $< 10^{-16}$ instability and therefore we conclude the first higher order mode resonance must be beyond the first modulation sideband.

The second case is for $\Omega < \Delta \omega_{hom} < 2\Omega$ as shown in Fig. 3.2 by the blue colored area around $\Delta \approx 3\Omega/2$. As an example, for a higher-order mode situated exactly at $3\Omega/2$ and for the parameters stated above, we get $\delta \omega(\frac{3\Omega}{2}) = -2\pi \times 6.6$ mHz, still representing a fairly large shift. However, the error signal has a zero crossing at $\Delta = \Delta_0 \approx 1.67 \Omega$ for our parameters. If the first higher-order mode is at $\Delta = \Delta_0$ from the longitudinal mode resonance, this mode will have no influence on the error signal of the fundamental mode. This situation can always be achieved by adjusting the sideband modulation frequency. We evaluate the influence of the next higher order mode on the error signal for this case to be $-2\pi \times 1.6$ mHz and thus tolerable.

3.2.2 Alignment tolerances for near-instability cavities

Cavities close to instability are more sensitive to misalignment of the mirrors. This requires tight tolerances to spacer and mirror manufacturing, and to mirror alignment. The displace-
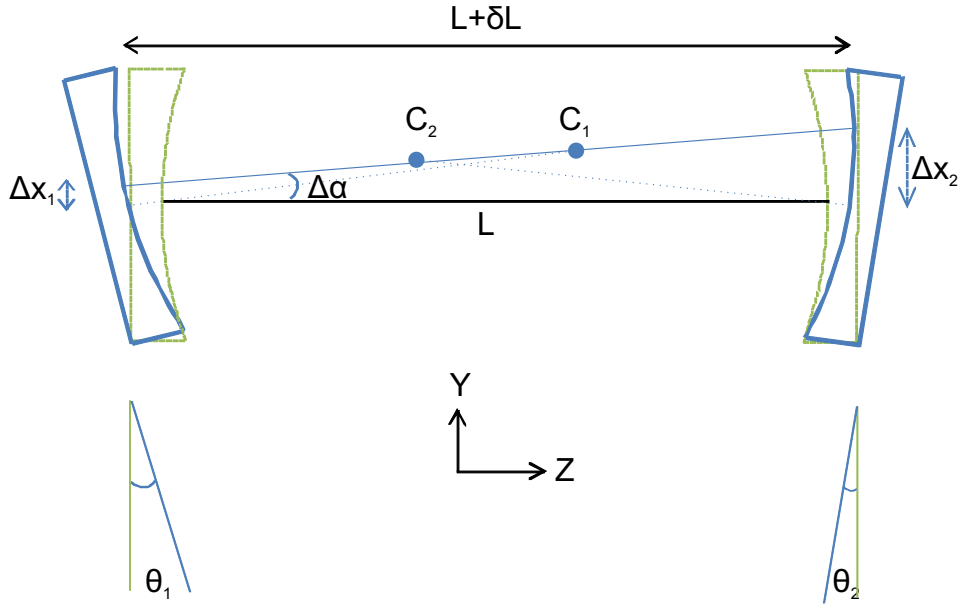
Figure 3.3: Illustration of the misalignment and the mode displacement in a stable FP resonator. The original positions are drawn in green and the misaligned positions are drawn in blue.

ment of the optical mode from the center of the mirror and the geometrical axis of the spacer affects the vibration sensitivity of the optical cavity as we will discuss in Section 3.3. In order to estimate the required tolerances, we consider a FP resonator made of two mirrors S_i with the corresponding radii of curvature R_i and centers C_i, separated by the optical path length of the cavity L (see Fig. 3.3). If the mirror S_i is tilted by an angle θ_i, the center of the mode intensity pattern on each mirror S_i shifts by a distance Δx_i from the geometrical axis [50] due to a rotation of the optical axis by an angle $\Delta\alpha$ according to:

$$\Delta\alpha = \frac{(1-g_2)\theta_1 - (1-g_1)\theta_2}{1-g_1g_2}$$

$$\Delta x_1 = \frac{g_2}{1-g_1g_2} \times L\theta_1 + \frac{1}{1-g_1g_2} \times L\theta_2$$

$$\Delta x_2 = \frac{1}{1-g_1g_2} \times L\theta_1 + \frac{g_1}{1-g_1g_2} \times L\theta_2.$$

For the case of a 10 cm long FP cavity with a near-planar mirror configuration [Table 3.1(D)], we estimate a shift of $|\Delta x_1 + \Delta x_2| = 100\ \mu$m for a mirror tilt of $\pm 0.8\ \mu$rad while with a near-concentric mirror configuration ($R_1 = R_2 = 5.1$ cm), the same shift occurs for a mirror tilt of ± 0.1mrad. We note that the sensitivity to mirror tilt scales with the length of the cavity for fixed g_1 and g_2. In addition, for near-concentric cavities, the positioning of the mirrors on the end face of the spacer is critical, particulary for long near-concentric cavities. A shift Δr of one mirror center from the symmetry axis of the cavity results in a rotation of the optical axis by an angle $\gamma \simeq \frac{\Delta r}{2R-L}$. This leads to a displacement $\Delta x = \gamma \times R$ of the optical mode on both

mirrors. We estimate for a 39.5 cm long cavity [Table 3.1(F)], that a shift of 10 μm of one mirror results in a mode displacement of 400 μm.

We conclude from these estimates that for a long cavity, working with a configuration close to instability requires challenging mechanical machining and alignment tolerances. However, for a short cavity the required tolerances are technically feasible.

3.3 Design of a vibration insensitive long optical cavity

As indicated in Table 3.1, long cavities can reach a thermal noise limited instability below 10^{-16}. However, low-frequency seismic and acoustic noise in the environment of the cavity causes fluctuations of the optical path length, particularly for long cavities with their intrinsically higher sensitivity to vibrations.

In this study, we adopt the approach of Nazarova *et al.* [81] to take advantage of the symmetries of the cavity spacer for intrinsic cancellation of length changes. The sign of the length change varies depending on the position of the support with respect to the symmetry plane that is orthogonal to the direction of the acceleration. In the case of individual support points, all points have to lie in the symmetry plane and act symmetrically on it for perfect length change cancellation. Thus, careful positioning of the mounting points allows supporting the cavity spacer with significantly reduced sensitivity to accelerations in all three directions. During the past years, significant effort was put into designing reference cavity systems with inherent insensitivity to vibrations [73, 77, 81–89].

Although length fluctuation and bending of the cavity can in principle be compensated, imperfections of the spacer manufacturing and mounting process lead to a non-zero vibration sensitivity.

The analysis of the sensitivity to vibrations and the results for an optimized mounting configuration are presented in this section, before comparing different diameter-length ratio configurations of a 39.5 cm long cavity. We end the section by estimating the effect of asymmetric spacer machining and unequal force distribution on the vibration sensitivity of the cavity.

3.3.1 Optimized long cavity design: FEM simulations

Vibrations of mechanical or acoustic origin usually have a frequency below 100 Hz. For example, street traffic noise frequency is between 10 and 100 Hz, while upper-floor building vibrations are in the range of 1 to 10 Hz. Acting on an elastic body such as a cavity spacer, these vibrations lead to a linear deformation of its shape through Hooke's law. The first order relative change of the optical path length in a cavity subject to accelerations a_j in the direction j is given by:

$$\frac{\Delta L}{L} = -\frac{\Delta \nu}{\nu} = \sum_{j=x,y,z} a_j k_j + \sum_{j=x,y,z} a_j \kappa_j \Delta r. \tag{3.8}$$

The first sum on the right-hand side of Eq. 3.8 describes a relative length change under a_j with the sensitivity coefficient k_j. The second sum denotes a relative change in optical path length due to a tilt of the mirrors, characterized by the coefficient κ_j, in the case where the optical

mode is displaced from the mechanical symmetry axis of the cavity by an average distance Δr. In the ideal case, where $\Delta r = 0$, the mirror tilt θ has a second order effect on the length change $\delta L \propto \theta^2$, which can be neglected [50].

We have performed simulations using the Finite Element Method (FEM) [71] to determine the optimum position of the supporting points for a 39.5 cm long cavity. The simulation provides a solution for which the cavity length variations k_j vanish and residual angle tilt coefficients κ_j became small, as well as the sensitivities of these coefficients to changes from the optimum support point positions.

The mounting strategy described in the following is the result of several FEM simulations made for multiple cavity designs (See Appendix B). This chosen design has the smallest residual sensitivity to vibration in the axial direction, and the largest tolerances with respect to machining, and allows a large degree of adjustability of the support points.
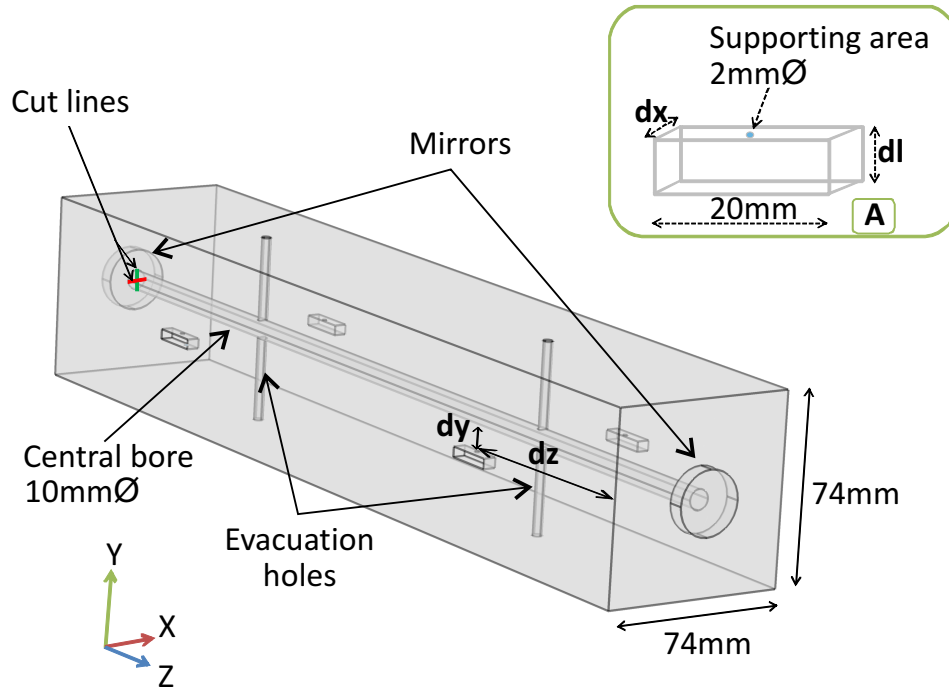
Figure 3.4: Parameters of the 39.5 cm long cavity. The inset shows the parameters for one of the cut-outs by which the cavity will be supported, and the blue point indicates the fixed contact position of the mechanical support.

The parameters of the 39.5 cm long cavity are presented in Fig. 3.4. The spacer has a cuboid shape with a square cross section of 74 mm side length. For the simulation, we assume that the ULE spacer material is perfectly homogenous, as well as the FS mirror material. A force density $\overrightarrow{a} \cdot \rho_x$ with $|\overrightarrow{a}| = |\overrightarrow{g}| = 9.8$ m s^{-2} is applied to the ULE spacer of density ρ_s = 2210 kg m^{-3}, and on the FS mirrors of density ρ_m = 2203 kg m^{-3}. It induces a quasi-static elastic deformation, as we study low frequency effects.

As shown in Fig. 3.4, four small cut-outs have been designed in the ULE spacer (two on each side) in order to support the cavity. All the cut-outs (box (A) in Fig. 3.4) have the same dimensions. The size of the cut-outs is a compromise between maximum adjustability of the

support points and the retention of the symmetry between upper and lower halves of the spacer by choosing the support points as close as possible to the central horizontal symmetry plane. The mechanical support of the cavity is in contact with the ULE spacer only in a small circular area of 2 mm diameter to reduce thermal conductivity between the heat-shields (see Chap. 4) and the cavity through the supporting legs. The displacement of the mirror and its tilting angle are evaluated from the displacement field[2] U_z: the component along the optical axis (Z) of the displacement of the vertical cut-line (for the case of vertical (along Y) or axial (along Z) accelerations) and the horizontal cut-line (for the case of horizontal accelerations (along X)), crossing the center of the mirror, as shown by the green and red lines of Fig. 3.4, respectively.
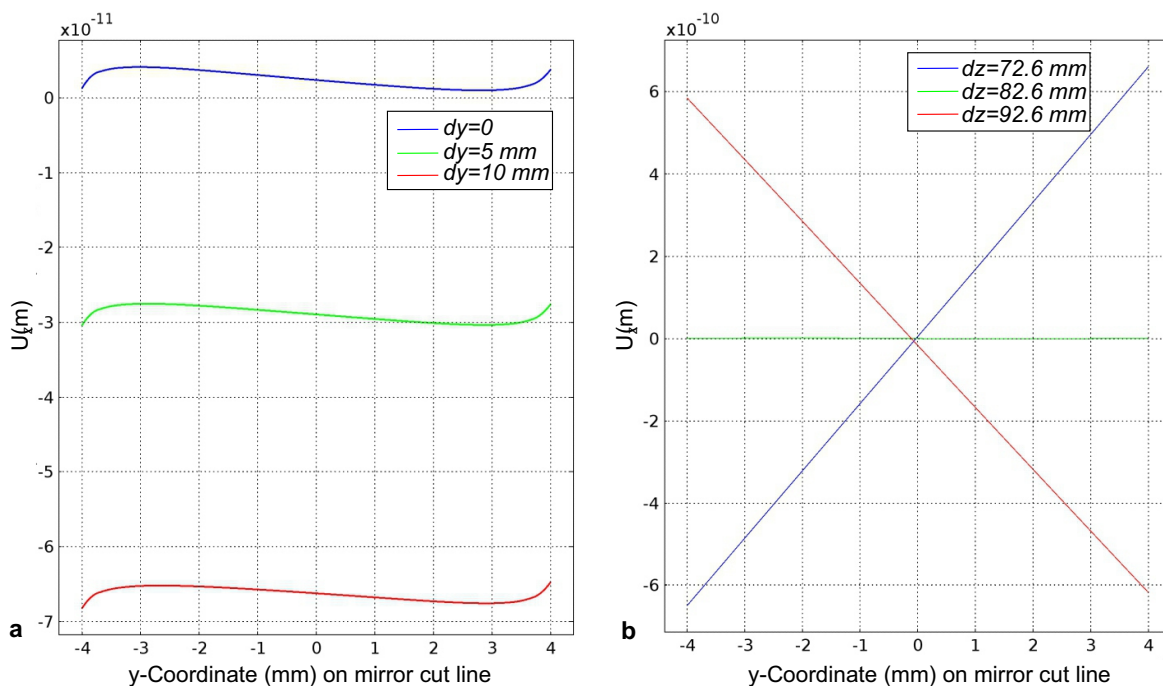
Figure 3.5: Support-point-dependent mirror displacement and tilt under vertical acceleration shown in Fig. 3.4. Z-component of the displacement field, $U_z(y)$, along the vertical mirror cut-line as a function of the (a) dy ($dz = 83$ mm fixed) and (b) dz ($dy = 0.5$ mm fixed) positions of the cut-out. Length changes and mirror tilts manifest themselves as offsets and non-zero slopes of the curves, respectively. The simulations show that length changes are sensitive to the dy position, whereas tilt is introduced by a non-optimum dz.

To find the optimum mounting points and to estimate the allowed machining tolerances, we vary symmetrically the position of the four cut-outs within the spacer[3].

We first consider vertical acceleration along the Y axis. The volume of the cut-outs and in particular their height dl (dimension of the cut-out along the Y axis) break the symmetry of the cavity with respect to the middle horizontal symmetry plane (Z, X). This results in a

---

[2]As calculated by the simulation program COMSOL.

[3]In the simulation, we vary the position of the entire cut-out, while the supporting point is fixed at the center of the cut-out.

finite axial length change under vertical acceleration through Poisson's ratio [81], see (a) in Fig. 3.5. This effect scales with the diameter of the cavity and can be cancelled by optimizing the parameter dy (position of the cut-out along the Y axis, relative to the middle horizontal plane of the cavity).

Mirror tilt is introduced through the asymmetric expansion of the spacer with respect to the middle horizontal plane (X,Z) due to Poisson's ratio, and through the bending of the cavity around the support points with two extreme cases: supporting in the center leads to downward tilt of the ends of the cavity, whereas supporting at the ends results in an upward tilt. In between these two configurations, there is an optimum position with vanishing total mirror tilt that can be found by adjusting dz (position of the cut-out along the optical axis Z, starting from the end faces), see (b) in Fig. 3.5.

The simulation process is iterative; two of the three parameters (dx, dz and dy) are fixed, while the third one is varied. The depth of the cut-out dx (from the side face of the spacer towards the optical axis) is optimized first such that both the mirror displacement and the mirror tilt are canceled for the same fixed value of dx. Close to the optimum values of dz and dy, the three parameters can be considered independent and a small variation (<500 μm) of dx has a negligible effect on the mirror tilt and length change of the cavity.

The relative displacement values at the mirror center as a function of the parameter dy are plotted in Fig. 3.6 (a). The tilt angle of the mirror is plotted as a function of the parameter dz in Fig. 3.6 (b). The simulations confirm the dependence of the length change and the mirror tilt on the variables dy and dz, respectively, and that these two variables can be considered as independent. Linear fits to the data shown in Fig. 3.6 provide us with the optimum positions $dz = 82.6$ mm and $dy = 0.5$ mm. The slope of these fits is a measure of the sensitivities k_y and κ_y to machining tolerances δdy and δdz for the cut-outs, and to Δr. The sensitivity to changes in the support points for horizontal and axial accelerations was determined using the same methods as for the vertical direction.

Table 3.2 presents a summary of the simulation results as functions of sensitivities to the machining tolerances for a 39.5 cm long cavity loaded with vertical, axial, and horizontal acceleration fields. The symmetry of the cavity spacer with respect to horizontal (along X) and axial (along Z) accelerations is maintained through the mounting structure, thus eliminating length changes along the cavity axis. For axial acceleration, a mirror tilt occurs due to $dy \neq 0$ which can not be avoided unless the supporting legs are exactly on the horizontal symmetry plane ($dy = 0$). By choosing cut-outs of small volume, we reduce the magnitude of the dy parameter to $dy = 0.5$ mm and get a tolerable sensitivity to axial acceleration of $63 \times 10^{-12}/g$ for the ideal case of $\delta dy = 0$. For the horizontal acceleration, the optimum cut-out position agrees with the optimum value found for the vertical acceleration within the precision of the simulations.

The measured vibration spectrum in our laboratory is a few $\mu g/\sqrt{\text{Hz}}$ at 1 Hz in all three directions (See Chapter. 4, Fig. 4.15). Thus, to achieve a relative length change below the expected thermal noise limit ($\frac{\Delta L}{L} < 10^{-16}$), we need the machining tolerances for making the supporting cut-outs on the spacer to be in the order of a few hundred μm. The large sensitivity to mirror tilt in long cavities requires an alignment of the optical axis with the geometrical axis on the mirrors (Δr) to be precise to within a few 100 μm. Both requirements are achievable with current technology.
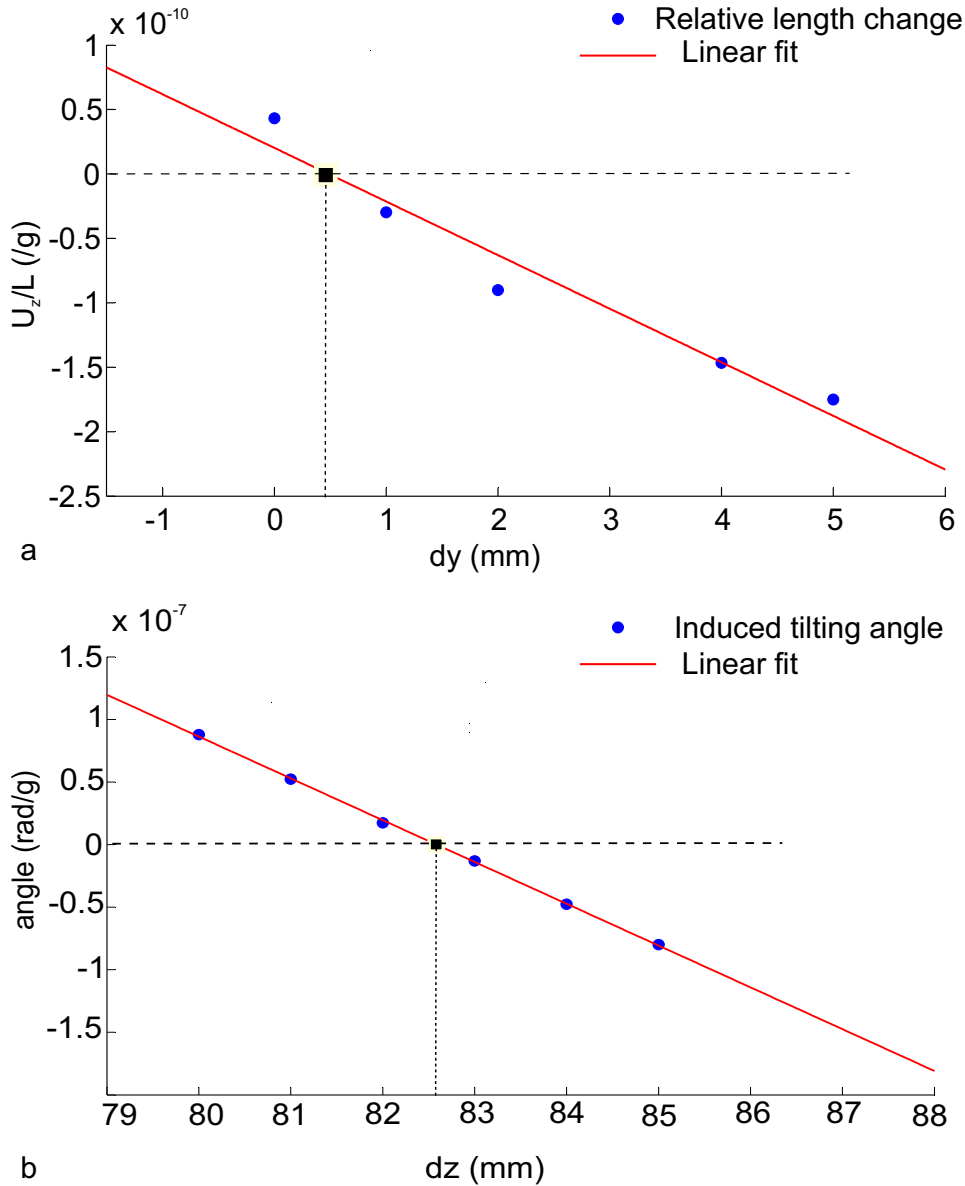
Figure 3.6: Simulated cavity length change and tilt under vertical acceleration as a function of parameters dy and dz. (a) Relative cavity length change U_z/L at the center of the mirror as a function of the cut-out position dy for fixed $dz = 83$ mm. A linear fit provides the optimum value of $dy = 0.5$ mm and a sensitivity to machining tolerances of $k_y = 42 \times 10^{-12} \cdot \delta dy/(g \cdot \text{mm})$. (b) Cavity mirror tilt as a function of the cut-out position dz for fixed $dy = 0.5$ mm. A linear fit provides the optimum value of $dz = 82.6$ mm and a sensitivity to machining tolerances in dz of $\kappa_y = 84 \times 10^{-12} \cdot \delta dz/(g \cdot \text{mm}^2)$.

Direction of acceleration $g = 9.8 \text{ ms}^{-2}$	Tolerances	
	k_j $(10^{-12}/(g \cdot \text{mm}))$	κ_j $(10^{-12}/(g \cdot \text{mm}^2))$
Vertical (Y)	$42 \cdot \delta dy$	$84 \cdot \delta dz$
Horizontal (X)	≈ 0	$68 \cdot \delta dz$
Axial (Z)	≈ 0	$126 \cdot (dy - \delta dy)$

Table 3.2: Optimum support point positions and acceleration sensitivities to machining tolerances of a 39.5 cm long cavity with a square cross section of 74 mm side length. For the vertical acceleration, we evaluate the sensitivities of Fig. 3.6, and we use the same method for evaluation under horizontal and axial accelerations.

### 3.3.2   Influence of the diameter-length ratio

Bending of the mirrors under accelerations orthogonal to the optical axis is caused by a bend of the entire spacer (extremal for support points either in the center or the outer points along the optical axis), and an asymmetric expansion along the cavity axis of the lower and upper halves of the cavity due to Poisson's ratio [81]. For vertically mounted cavities these two effects cancel for a certain diameter-length ratio [73]. For the horizontally mounted cavities considered here, the effects add constructively, and an additional length change is introduced. However, by choosing an appropriate diameter-length ratio, we can balance the sensitivities to length change and tilt. In Fig. 3.7, we compare the relevant factors k_j and κ_j under vertical, axial and horizontal accelerations for different square cross sections of a 39.5 cm long cuboid cavity. The sensitivity to mirror tilt becomes larger for smaller cross sections, whereas the sensitivity to length changes under accelerations perpendicular to the optical axis scales linearly with the cross section.

We found that, given machining tolerances on the order of a few 100 μm, square cross sections between 65 mm and 85 mm offer a good tradeoff between length and tilt sensitivity.

3.3.3   Asymmetric spacer and inhomogeneous loading forces

We investigated the influence of geometrical deviations from the optimum cavity shape to assess the required machining tolerances, which become critical for longer cavities. Through numerical simulations, we estimate the sensitivity of a 39.5 cm long cavity to accelerations in the case of an asymmetric spacer that has an end surface tilted by an angle α around a horizontal axis, while maintaining the calculated optimal support points for a perfect rectangular shape. The sensitivity of the cavity becomes $4.9 \times 10^{-9} \alpha/(g \cdot \text{rad})$ and $4 \times 10^{-8} \alpha/(g \cdot \text{rad})$ under vertical and axial accelerations, respectively. The horizontal acceleration is unchanged, since in this case the corresponding symmetry is not broken. We expect that a tilt along the vertical axis results in similar sensitivities for horizontal and axial accelerations. We conclude, for a 39.5 cm long cavity of width and depth equal to 74 mm, that the faces of opposing sides of the cavity should be parallel to within 0.1 mrad to achieve a sensitivity of less than $10^{-11}/g$ to

accelerations in all directions. This requirement is technically achievable and might be further relaxed by experimentally determining new optimal support point positions (See Chap 4).
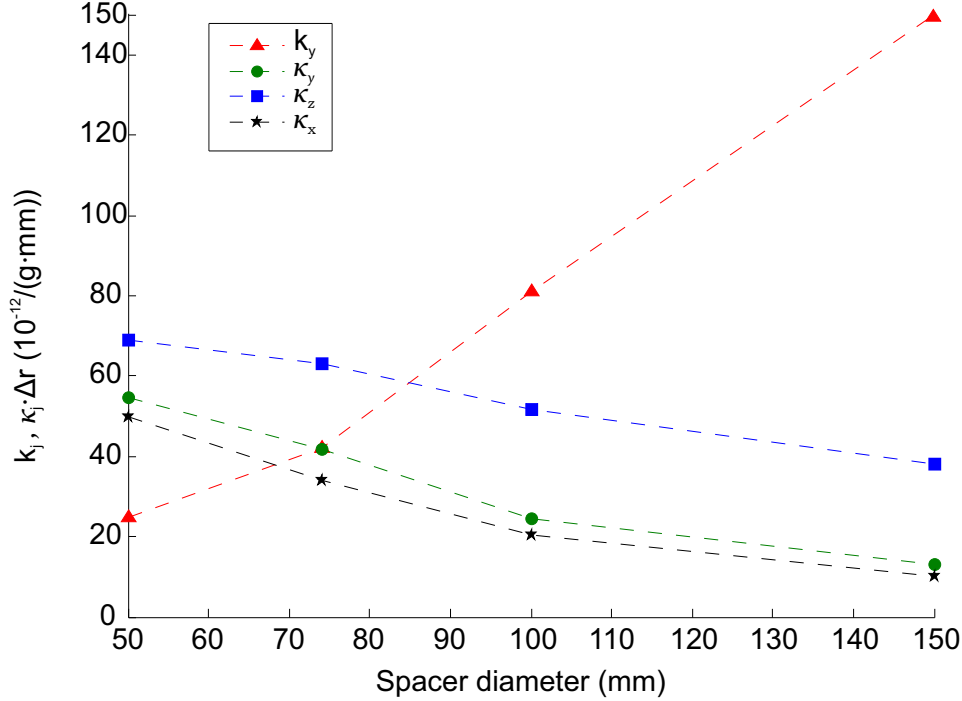
Figure 3.7: Variation of the sensitivity coefficients for mirror tilt κ_j and mirror displacement k_j as a function of the spacer cross section, under vertical (Y axis), axial (Z axis), and horizontal (X axis) accelerations. The length of the spacer is fixed to 39.5 cm as well as the shape of the supporting cut-outs. We have assumed $\Delta r = 0.5$ mm and $\delta dy = 0.5$ mm for the calculation. The dashed lines are a guide to the eye.

Equal distribution of the total reaction forces $\overrightarrow{F} = m\overrightarrow{a}$ applied between the supporting points is also of crucial importance, and an unexpected force imbalance may be a reason for differences between theoretical results and experimental measurements of the vibration sensitivities [77]. FEM simulations show that a force difference ΔF applied between two pairs of supporting legs induces a sensitivity of $7.4 \times 10^{-9}/g \cdot \frac{\Delta F}{F}$ in the axial direction and $2.4 \times 10^{-10}/g \cdot \frac{\Delta F}{F}$ in the vertical direction, for this cavity of mass $m = 5$ kg. Equal force distribution to within 1% between the supporting legs is therefore of major importance for a vibration insensitive cavity. Equalizing the forces applied on the cavity could be achieved either by using elastic supports or by converting the four-point support into an effective three-point support as we will show in Chap. 4.

3.3.4 Limitation of the FEM simulation

We use the finite element simulation method to calculate the component displacements and strains under external loads. This method depends strongly on the size of the mesh elements[4]:

---

[4]A prior knowledge of the FEM simulation software, largely used in modeling, is assumed in this subsection.

the more accurately the mesh matches the cavity geometry, the more accurate the analysis results will be. We see a clear difference in the simulation results using predefined meshing methods on COMSOL. For example, we see an error in the vibration sensitivity on the order of 10^{-10}/(g.mm) when changing from predefined "fine" to predefined "normal" meshing. Similar effects on cavity simulation results have been discussed by Nazarova [90]. It is possible to make the meshing much finer around the critical calculation zones i.e. mirror cut-lines (see Fig. 3.4), then increase the element integration size with a defined "growing rate" over the rest of the spacer body. For that, we use an adaptive meshing procedure[5] with up to 2 generations of calculation iteration to produce the most accurate meshing possible for the cavity and to avoid being limited by the simulation time or computer memory. Using this technique, we estimate the meshing error to be on the order of 10^{-12}/(g.mm).

---

[5]Adaptive meshing is a COMSOL function. It allows an automatic adjustment (after some iterations) of the meshing. We use 25 mesh elements around the cut-lines and an element growth rate factor of 1.5).

Chapter 4

Laser stabilization system

We have seen in the first two chapters that the frequency stability of a cavity resonance depends on the length stability of the cavity as $\Delta L/L = -\Delta\nu/\nu$. In addition to vibrations, environmental influences such as pressure and temperature fluctuations change the optical distance between the two mirrors and thus the resonance frequency of the cavity. In order to reduce these disturbances, have placed the cavity in a vacuum chamber provided with the heat-shields for active and passive thermal control, and carefully isolated it from mechanical and acoustic vibrations. An external cavity diode laser (ECDL) was locked to the cavity. By changing external parameters (i.e. cavity temperature, vibration force, etc.) and comparing the laser's frequency to other cavities or to a stable RF-signal via an optical frequency comb, the sensitivity of the cavity resonance frequency to these effects was evaluated.

This chapter is divided into two sections. In the first section we will present the mechanical setting of the cavity. The effect of the four external perturbations, thermal expansion, mechanical vibration, and linear drift of the cavity, as well as pressure perturbations in the vacuum chamber are presented and evaluated. The implemented solutions for minimizing these effects are explained. In the second section we focus on the laser locking performance using the PDH technique, the effect of residual amplitude modulation (RAM), and the influence of laser intensity instability on the performance of the cavity.

In this chapter and at the end of each subsection, the influence of environmental effects and perturbations from the laser locking scheme on the cavity performance are evaluated in terms of fractional frequency instability and compared to the limit imposed by the thermal noise of the cavity.

4.1 Realization of the environmentally insensitive optical cavity

4.1.1 Temperature stabilization

Fluctuations of the temperature T of the cavity affects its length stability, which is typically relevant for time scales larger than a second. The fractional variation of the cavity length as a

function of the temperature variation in the interval from T_i to T_f is given by:

$$\frac{\Delta L}{L} = \int_{T_i}^{T_f} \alpha(T_f)dT \tag{4.1}$$

where $\alpha(T)$ is the Coefficient of Thermal Expansion (CTE) as a function of the temperature T. The effect of temperature fluctuations can be reduced by choosing low thermal expansion materials for the cavity and by thermal isolation and temperature stabilization of its housing system. We will start by presenting the thermal properties of the 39.5 cm optical cavity and then describe the housing system. We then report on a measurement of the thermal expansion behaviour of the cavity and determine its optimum operating temperature as well as the effect of the temperature instability on the overall performance of the stabilized laser.

Thermal properties of the 39.5 cm cavity

Ultra Low Expansion glass ceramic (Corning® ULE) is used as the spacer material because of its combination of ultra low thermal expansion properties [91] and relatively low mechanical losses compared to e.g. Zerodur[1]. This TiO$_2$-doped silica glass has a temperature dependent CTE $\alpha_s(T)$ that is zero at a specific temperature T$_s$ and can be approximated to second order in T by:

$$\alpha_s(T) = a_s(T - T_s) + b_s(T - T_s)^2, \tag{4.2}$$

where a_s is on the order of 10^{-9}/K^2 and b_s is on the order -10^{-11}/K^3 denoting the linear and quadratic temperature coefficients, respectively. T_s is the CTE null temperature, which for Corning ULE is usually specified to be around 20°C [92].

The mirrors are made of Fused Silica (FS) in order to reduce their dominant contribution to the thermal noise (See Chap. 3). However, fused silica has a relatively high thermal expansion coefficient[2] α_m of about 500×10^{-9}/K.

The CTE mismatch between the ULE spacer and the FS mirrors leads to an effective CTE $\alpha_{\text{eff}}(T)$ of the system (ULE spacer + two FS mirrors) that can be written as [93]:

$$\alpha_{\text{eff}}(T) = \alpha_s(T) + \xi \frac{2R_m}{L}(\alpha_m - \alpha_s(T)) \tag{4.3}$$

where ξ is the coupling coefficient assuming a linear stress-strain relation between the spacer and the optically contacted mirror, R_m is the radius of the mirror and L is the length of the cavity. The coupling coefficient ξ is positive and depends only on the geometry of the spacer and mirrors and their mechanical properties; it is independent of the temperature and their thermal expansion properties [92]. It is worth mentioning that here we neglect the effect of the thermal expansion of the mirror coating since it was shown in [93] to be negligible compared to the expansion of the substrate itself.

Since the mismatch of CTE $\alpha_m - \alpha_s(T)$ is positive, and the CTE slope a of the spacer in Eq. 4.2 as well as ξ are positive, the system (ULE spacer + FS mirrors) will have a higher

---

[1]Mechanical losses in Zerodur are $\phi_Z \approx 3 \times 10^{-4}$, and the linear coefficient of thermal expansion is $\approx 5 \times 10^{-9}$/K^2.

[2]considered constant for temperatures around 30°C

$\alpha_{\text{eff}}(T)$. Thus, the final CTE null temperature T_0 that corresponds to the minimum thermal expansion of the cavity made of ULE spacer and FS mirrors will be below the CTE null temperature T_s of the cavity made of ULE only. FEM simulations (see Chap. 3) of the 39.5 cm cavity thermal expansion behaviour, assuming $T_s = 20°C$, which is the most common case for Corning® ULE are plotted in Fig. 4.1. Changing from ULE mirrors to FS mirrors shifts the CTE null point of the cavity by about $-10°C$.
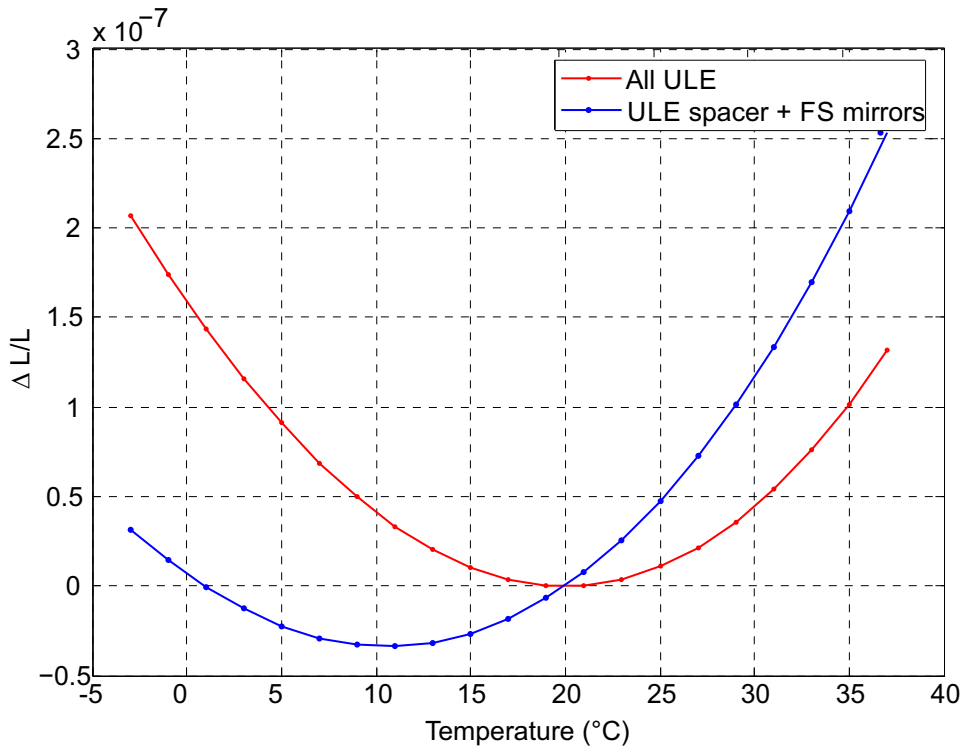
Figure 4.1: FEM simulated thermal expansion of an optical cavity with a ULE spacer (L=39.5 cm, D=7.4 cm), and two mirrors of diameter $2R_m$ =2.54 cm, as a function of the temperature in °C. The red line shows the behaviour of a cavity made of ULE (mirror substrates and the spacer are made of ULE) assuming the CTE null temperature of the ULE is at $T_s = 20°C$. The blue line is the expansion behaviour of the same cavity spacer but with mirrors made of FS. The minimum expansion temperature is shifted by about $-10°C$

Despite specifications by Corning®, ULE exhibits strongly varying CTE null temperatures, usually below 20°C. Using FS mirrors, this temperature is further reduced, requiring cooling of the entire cavity to below room temperature [94]. This is typically accomplished through Peltier cooling of the bottom of the cavity, requiring a technologically challenging setup to guarantee a homogeneous distribution of temperature around the cavity.

Legero *et al.* proposed to reduce the effect of FS mirrors on the thermal properties of ULE by contacting ULE rings on the back of the FS mirrors [92].

In our case, the spacer is made of a different type of Corning ULE material that has larger TiO_2 content than what Corning usually offers, which puts its intrinsic CTE null point T_s above 50°C. This means that contacting the FS mirrors will bring the optimum operating temperature

T_0 in our case to above room temperature. For this, we design a housing system that maintains homogenous temperature around the cavity by only heating.

Heat transfer laws

The design of the housing system that we are about to describe provides a high thermal isolation for the cavity. In our case, the heat transfer can be conductive or radiative. According to Fourier's law, the conductive heat transfer $\dot{q}_c$ from a system at fixed temperature T_1 toward a system of temperature $T_2(t > t_0)$ with $T_2(t_0) < T_1$, through material of thermal conductivity λ of length d and contact surface a_c is:

$$\dot{q}_c = \lambda \frac{a_c}{d}(T_1 - T_2(t)). \tag{4.4}$$

The conductive heat transfer depends on the conductivity of the connecting material and the contact surfaces, and can be reduced by choosing a connecting material with low thermal conductivity between the different parts of the housing and by minimizing their contact surfaces.

However, the heat transfer through thermal radiation, especially for our operating temperature above 40°C, can limit the thermal isolation between the different parts of the housing and the cavity. The radiative heat flow $\dot{q}_{rad}$ from a surface A_1 of temperature T_1 to a surface A_2 of temperature $T_2(t_0) < T_1$ is written as [95]:

$$\dot{q}_{rad} = \sigma_{SB}(\frac{1}{A_1\varepsilon_1} + \frac{1}{A_2\varepsilon_2} - \frac{1}{A_1})^{-1}(T_1^4 - T_2(t)^4) \tag{4.5}$$

where σ_{SB} is the Stefan-Boltzmann constant[3], and ε_1 and ε_2 are the emissivity of the surfaces A_1 and A_2, respectively. The emissivity is a property of the material surface that ranges from 0 to 1 and defines the ratio of the transmitted heat compared to a black-body of emissivity $\varepsilon = 1$. A perfectly reflective surface would have an emissivity equal to zero, so it is possible to reduce the heat emissivity by using a highly reflective coating on the housing surfaces and by polishing them to better than $\lambda/10$. For a small applied temperature step with $T_1 - T_2(t) \ll T_1$, a first order approximation of Eq. 4.5 can be written as:

$$\dot{q}_{rad} \approx 4\sigma_{SB}T_1^3(\frac{1}{A_1\varepsilon_1} + \frac{1}{A_2\varepsilon_2} - \frac{1}{A_1})^{-1}(T_1 - T_2(t)). \tag{4.6}$$

Taking into account both the radiative and conductive heat transfer, one can express the variation of the temperature T_2 of the system (2) under the influence of the temperature T_1 of the system (1) as a function of time using Eq. 4.6 and Eq. 4.4 by:

$$C_P(2)\frac{\partial T_2(t)}{\partial t} = \dot{q}_{rad} + \dot{q}_c = \Lambda_{12}(T_1 - T_2(t)) \tag{4.7}$$

where $C_P(2) = M_2 \times c_p(2)$ is the thermal capacity of the system (2) of mass M_2 and specific heat capacity $c_p(2)$, and Λ_{12} is the total heat flow between systems (1) and (2). A solution

---

[3] $\sigma_{SB} = 5.6703 \times 10^{-8}$ W/(m²K⁴).

of Eq. 4.7 consists of the exponential propagation of the heat from T_1 towards T_2 that is characterized by the time constant $\tau_1 = C_p(2)/\Lambda_{12}$. Thus, fluctuations of the temperature T_1 that occur on a time scale faster than the time constant τ_1, will be attenuated (filtered) as if $1/\tau_1$ is the cut-off frequency of a first order low-pass filter between systems (1) and (2). In order to minimize the thermal fluctuation at the level of the optical cavity, two heat shields are placed around it, where the temperature of the outer heat shield is actively stabilized, which results in the combination of two first-order low-pass filters in series with different time constants.

Design of the cavity housing

We describe here the mounting system and housings starting from the cavity and going toward the outside. A sketch of the housing design for the stable 39.5 cm cavity is presented in Fig. 4.2 and the precise dimensions of the cavity chamber system can be found in Appendix D.
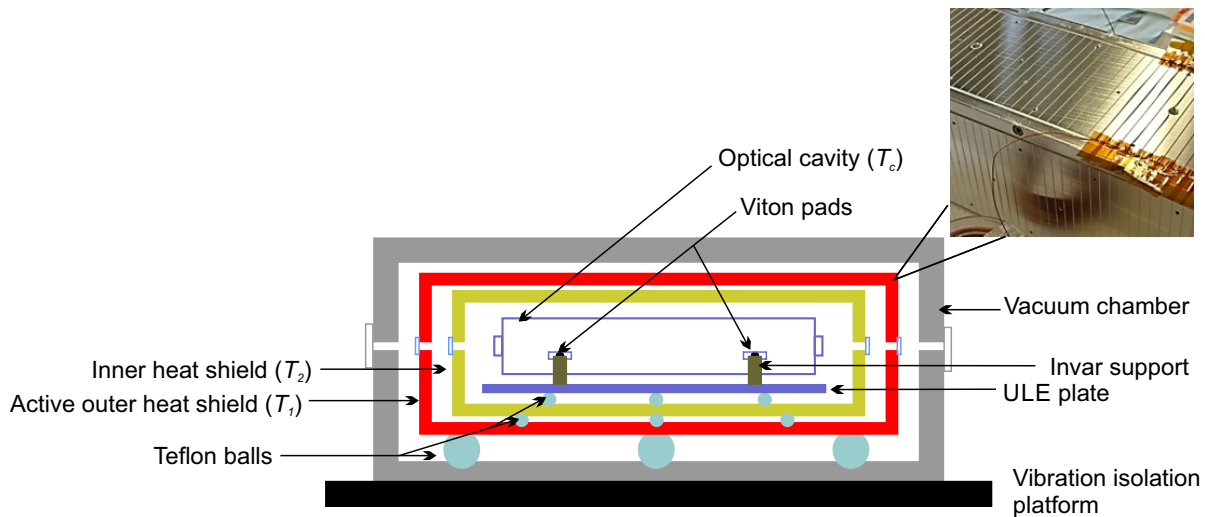
Figure 4.2: Schematic diagram of the 39.5 cm long cavity inside the vacuum chamber. The cavity supports (invar with viton pads on the top) are resting on a ULE plate which is placed inside the first (inner) heat shield made of gold coated brass. Three teflon balls serve as thermal isolation between the ULE plate and the first heat shield and three more between the first and second heat shield. The second heat shield, made of aluminum, is used for the active temperature stabilization inside the vacuum chamber, also made of aluminum. The temperature notations assigned to the different parts are: T_c for the cavity temperature, T_2 for the inner heat shield temperature, and T_1 for the active heat shield temperature. The insert photo of the active heat shield shows the serpentine pattern of the heating wire. This wire is fixed to the heat shield facets with 3 mm thick aluminum plates (the kapton tape (of brown color) shown on the photo is removed before fixing the plates).

The cavity (heat capacity c_p(ULE)=767 J/(kg·K), mass $M_c = 5.07$ kg) is placed on two invar U-shaped supports (see Sec. 4.1.2), that are resting on the top of a ULE plate (same material as the spacer) in order to reduce the radial tension that might accrue from the thermal expansion of the rest of the metallic housing. The Invar (thermal conductivity λ_{invar}=13 W/(m·K), height

= 40 mm) that is used for supporting the cavity has a less than 20 mm^2 contact surface with the ULE plate (thermal conductivity λ_{ULE}=1.31 W/(m·K), thickness = 5 mm) and no direct contact with the cavity, since we use viton half spheres on the top of each support (thermal conductivity λ_{viton}=0.26 W/(m·K), height 2 mm).

The ULE plate is placed on top of three teflon balls inside the first heat shield (of temperature T_1 in Fig. 4.2) made of gold coated brass (heat capacity c_p(Brass)=377 J/(kg·K), density: 8525 kg/m^3, thickness = 10 mm, mass M_1= 9.46 kg). The heat conduction between the ULE plate and the inner heat shields is minimised by using these three teflon[4] spheres of diameter $d_s = 7.93$ mm (Thermal conductivity $\lambda_{teflon} = 0.25$ W/(m·K)) on a kinematic mount[5] for maximum mounting stability and minimum contact surfaces $a_c \approx 32$ mm^2 (much smaller than d_s^2 as for a cylinder). The polished gold coating of the brass (emissivity of gold $\varepsilon_{Au} = 0.02$) minimizes the radiative heat transfer between this heat shield and the cavity (emissivity of glass and ULE $\varepsilon_{ULE} = 0.91$) as well as the rest of the housing system.

Three more teflon spheres ($d_s = 7.93$ mm) are used to place the passive inner heat shield inside the second heat shield (of temperature labeled T_2 in Fig. 4.2), and reduce the conductive heat transfer between them. Aluminum is used for building the second (outer) heat shield (heat capacity c_p(Al)= 897 J/(kg·K), density: 2701 kg/m^3, thickness = 10 mm, mass M_2= 9.51 kg). The temperature of the outer heat shield is actively stabilized. Since we will need to heat the chamber in order to operate the cavity at the CTE null point, i.e. above 40°C, the outer surface of the first heat shield contains grooves in which we place about 40 m of heating wire[6] in a serpentine pattern (separation distance 2 mm) for a homogeneous thermal distribution around the cavity. Six polished aluminium plates (~ 3 mm thickness) are used to hold the wire firmly to each side of the active heat shield and fixed with vacuum compatible screws (no additional adhesive). A picture taken during this procedure can be seen in Fig. 4.2. The surfaces of this aluminum heat shield and the aluminum plates are polished[7] in order to minimise the radiative heat transfer to the rest of the system (emissivity of polished aluminum $\varepsilon_{Al} = 0.04$). The used highly heat conductive housing materials homogenize the temperature distribution around the cavity.

The temperature stabilization of the active heat shield (labeled **2** in fig. 4.2) is realized by connecting the heating wire (around the outer heat shield) to a PI temperature controller system[8]. Eight temperature sensors[9] are glued using thermally conductive, vacuum compatible two-component epoxy [10] to different sides of the shield and connected through a sub-D feedthrough to the temperature controller for a feedback of the temperature.

Finally, this outer heat shield is placed inside the vacuum chamber on top of three bigger teflon balls with $d_s = 50.8$ mm in order to leave space for an eventual third passive heat shield. The custom made vacuum chamber is made of aluminum (wall thickness 30 mm) polished

---

[4]Polytetrafluoroethylene (PTFE).

[5]All degrees of freedom within the horizontal plan are fixed with minimum constraints. The center of gravity of the mounted system coincides with the center of mass the triangle formed by the balls.

[6]0.4 mm diameter, KAPW1X040 Kapton insulated copper wires, LewVac.

[7]Aluminum polishing paste used manually, chemical polishing is to be avoided with this type of 6061 aluminum alloy.

[8]Thermo-electric controller TEC from ibrt.com

[9]Glass-encapsulated sensor type B57560G1303+005 NTC-30KΩ@25°C

[10]two-component Aremco-Bond™860 Thermally Conductive Epoxy, Aremco.

from the inside for a minimum radiative heat transfer with the rest of the system. The use of highly conductive material such as brass (thermal conductivity $\lambda_{brass} = 109$ W/(m·K)) and aluminum ($\lambda_{AL} = 205$ W/(m·K)) allows a homogeneous thermal distribution around the cavity.

The two heat-shields around the cavity acts as a heat capacitance that filters the short term thermal fluctuations. The thermal time constant is modeled by taking into account both kinds of thermal transfer mechanisms explained in Eq. 4.4 and Eq. 4.6. According to Eq. 4.7, the variation of the temperature over time of the inner heat shield $T_2(t)$ and that of the cavity $T_c(t)$ is related to the fixed temperature of the active heat shield T_1 by the coupled equations:

$$
\begin{aligned}
\frac{\partial T_2(t)}{\partial t} &= \frac{1}{\tau_1}(T_1 - T_2) - \frac{1}{\tau_c}(T_c - T_2) \\
\frac{\partial T_c(t)}{\partial t} &= \frac{1}{\tau_2}(T_2 - T_c)
\end{aligned}
\tag{4.8}
$$

where τ_1 is the time constant between the active heat shield and the inner heat shield and τ_2 is the time constant between the inner heat shield and the cavity. τ_c describes the time constant of the temperature propagation from the cavity toward the inner heat shield (which is much longer than τ_1 and τ_2). Using the material properties described above, we obtain from our model $\tau_1 = 3.9$ days, $\tau_2 = 5.9$ days and $\tau_c = 41.2$ days (calculated at $1/e$ of the final temperature).

The term in $(1/\tau_c)(T_c - T_2)$ can be neglected due to the slow heat transmission from cavity to the inner heat shield compared to that from the active heat shield to the inner heat shield. From Eq. 4.8, we calculate the cavity temperature $T_c(t)$ that shows an exponential behaviour with two time constants given by:

$$
T_c(t) = T_i + (T_f - T_i). \left[1 - \frac{\tau_1}{\tau_1 - \tau_2} \exp\left(-\frac{t}{\tau_1}\right) + \frac{\tau_2}{\tau_1 - \tau_2} \exp\left(-\frac{t}{\tau_2}\right) \right]
\tag{4.9}
$$

where T_i and $T_f = T_1$ are the initial and final temperatures of the cavity, respectively. The time constants τ_1 and τ_2 allow the cavity to be insensitive to thermal fluctuations at the active heat shield that occur on a time scale shorter than 9.8 days. However, thermal sensor connection via copper wires ($\lambda_{copper} = 401$ W/(m·K), 0.4 mm diameter), which have a heat-transfer in the order of 4 mW per meter for a temperature difference of 20.5°C, and the windows on the sides of the vacuum chamber, create additional conductive and radiative heat transfer paths that results from the temperature gradient between the active heat shield and the rest of the laboratory ($T_{lab} = 23 - 27$°C), and can modify the estimated time constants.

In addition to a good thermal isolation, the cavity must be operated at the CTE null temperature for minimum thermal expansion. We describe in the following the temperature stabilization system used to identify the CTE null temperature of our 39.5 cm cavity and determine the real time constants of the system.

Measurement of the CTE null temperature and of the thermal time constant

We stabilized a 1070 nm laser (see Sec. 4.2.2) to the cavity at room temperature and under 10^{-5} mbar vacuum pressure. The stabilized laser is transferred via a 100 m long fiber to a

different lab (on the 5th floor of the same building), containing a frequency comb referenced to a hydrogen maser. A frequency beat-note is established between our laser and the frequency comb. An AC-coupled photodiode measures the beat-note frequency in the RF, which is sent to a frequency counter[11] to record the beat-note frequency shifting as the cavity temperature changes.
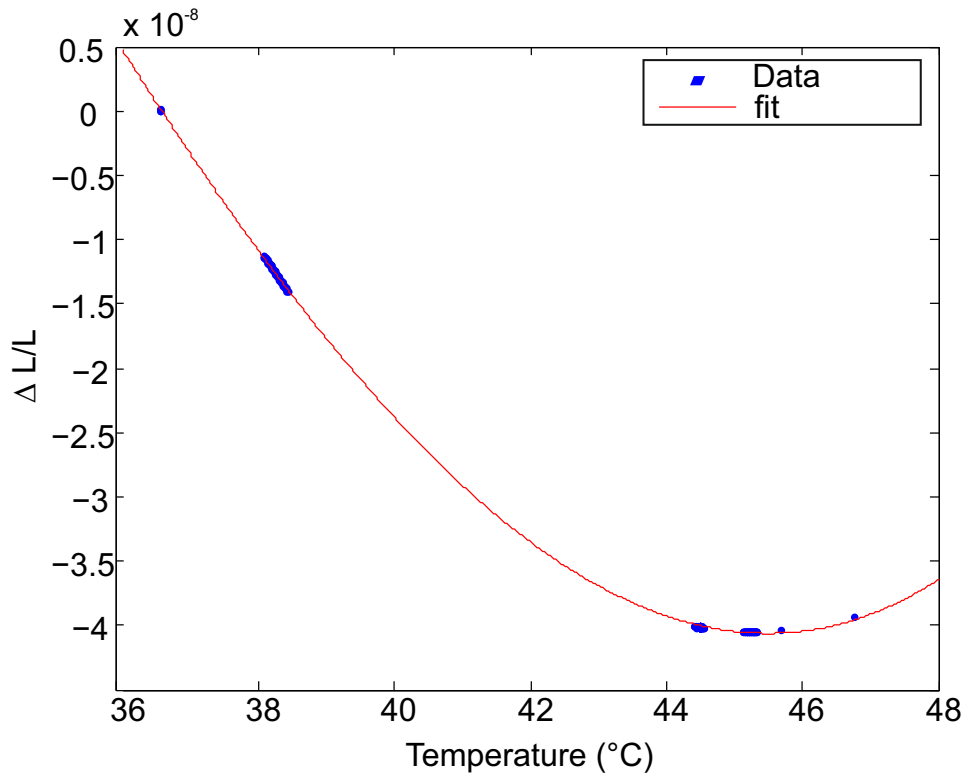
Figure 4.3: Relative length change of the cavity as a function of the temperature. The parabolic fit is made as in Eq. 4.10. The minimum of thermal expansion corresponds to $T_0 = 45.50(1)°C$. These results were established for one temperature step (36°C to 46°C), and recorded over 7 days of measurements. The discontinuities in the measured data (in blue) occurred when one of the lasers of the frequency beat-note (our laser or the reference laser from the comb) was out of lock.

In order to monitor the temperature of the ULE cavity, we attach an extra sensor[12] to the ULE spacer (out of the temperature stabilization loop) using vacuum compatible Kapton tape. This sensor is removed after the conclusion of the CTE point measurements. We sweep the temperature of the active heat shield from 36°C to 46°C in order to find the temperature of minimum thermal expansion. The relative length change $\Delta L/L$ as a function of the temperature is shown in Fig. 4.3. When changing the temperature of the cavity, the frequency of the beat-note shifts following the cubic law of the thermal expansion of the cavity as a function of

---

[11]FXE High Resolution Multichannel Synchronous Phase Recorder, K+K Messtechnik GmbH
[12]Sensor type B57560G103F NTC 10KΩ@25°C

temperature, which corresponds to:

$$\frac{\Delta \nu}{\nu} = -\frac{\Delta L}{L} = \frac{a}{2}(T_c - T_0)^2 + \frac{b}{3}(T_0 - T_c)^3 + C_0. \tag{4.10}$$

By fitting this expression to the data, we estimate $T_0 = 45.50(1)°C$ for the CTE null temperature at which the length variation of our cavity is minimum, and $a = 1.03(1) \times 10^{-9}/K^2$ and $b = -12.3(2) \times 10^{-12}/K^3$ the linear and quadratic thermal coefficients, respectively, from the fit. C_0 is an arbitrary constant, and a function of the initial conditions. The linear drift of the cavity over time of 0.2 Hz/s due to the aging of the material was removed in this evaluation [92] and will be discussed separately in Sec. 4.1.3. According to these results and to Eq. 4.10, a temperature change of 1 mK will introduce a frequency change on the order of one kHz when operating the cavity at $38°C$, whereas at $T = T_0$, the frequency variation will be suppressed to 0.1 Hz for the same temperature variation. This confirms the fact that operating the cavity at T_0 reduces its sensitivity to temperature fluctuations.

Evaluation of the cavity temperature instability

At a small temperature offset δT from the CTE point of the cavity ($\delta T = |T_c - T_0| \ll T_0$), the Allan deviation of the cavity fractional temperature fluctuation σ_T^c is related to the induced fractional (length) frequency stability σ_y by:

$$\sigma_y \approx a|\delta T|\sigma_T^c. \tag{4.11}$$

Thus, in order to operate the cavity at the thermal noise limit of 7×10^{-17} at 1 s, while $|\delta T| = 1$ mK, the instability of the temperature at the level of the cavity σ_T^c should not be higher than $70\,\mu$K at 1 s.

The cavity temperature instability σ_T^c is evaluated from the active heat-shield temperature variation over time $T_1(t)$, taking into account the filtering effect from the time constants of the heat shields.

For this evaluation, we record the temperature of the active heat shield via one of the in-loop sensors[13]. The Fast Fourier Transform (FFT) of $T_1(t)$ is then filtered by applying the transfer function obtained from the heat-shield time constants as:

$$H_{LP}(\omega) = \frac{1}{\sqrt{1 + (\frac{\omega}{\omega_1})^2}} \cdot \frac{1}{\sqrt{1 + (\frac{\omega}{\omega_2})^2}} \tag{4.12}$$

where ω is the Fourier frequency of the temperature fluctuation, $\omega_1 = 1/\tau_1$ is the cut-off frequency of the first low pass filter (active heat shield to passive heat shield), and $\omega_2 = 1/\tau_2$ is the cut-off frequency of the second low pass filter (passive heat shield to cavity). From the inverse of this filtered temperature FFT we obtain the temperature fluctuations at the cavity.

Two parameters are important for evaluating the induced fractional frequency stability:

---

[13]The temperature stabilization software gives a real-time reading of the temperature of the stabilized system.

- The first parameter is the value of the time constants τ_1 and τ_2. In our case, an out-of-loop sensor remains at the level of the inner heat shield[14]. This sensor is connected by a Kapton wire (~ 1 m length, $\lambda_{copper} = 401$ W/(m·K), wire diameter 0.4 mm), which has a non-negligible conductive heat transfer in the order of 4 mW for temperature difference of 20.5 K between the inner heat shield and the vacuum chamber. This sensor shortens the thermal time constant of the system thus it should be removed in the future. Nevertheless, we measured the current thermal time constants, which are found to be $\tau_1 = 0.6$ days and $\tau_2 = 2.5$ days, in order to have a realistic estimation of the effect of thermal fluctuations on the current stability of the cavity length.

- The second parameter is the cavity temperature offset from the CTE point $\delta T = T_c - T_0$. The quadratic behaviour of the frequency as a function of the temperature (Eq. 4.10) changes the cavity sensitivity to thermal fluctuations as a function of the set value of T_c.
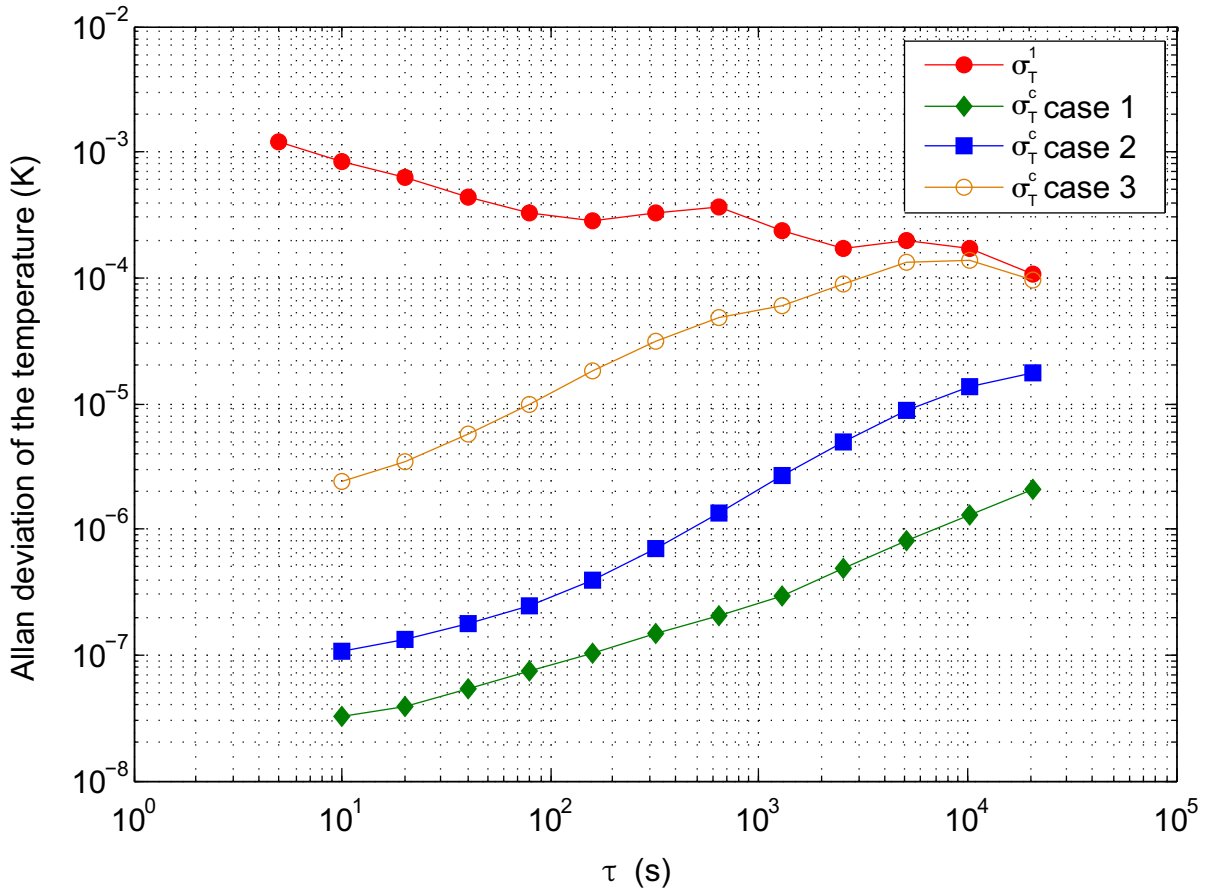
Figure 4.4: Allan deviation of temperature fluctuations as a function of the averaging time τ. Allan deviation of temperature fluctuations at the measured active heat-shield σ_T^1, and extrapolated at the cavity σ_T^c using Eq. 4.9 in case (1) ($\tau_1 = 3.9$ days, $\tau_2 = 5.9$ days), case (2) ($\tau_1 = 0.6$ days, $\tau_2 = 2.5$ days), and case (3) ($\tau_1 = 0.2$ days, $\tau_2 = 0$ days)

---

[14]This sensor is used for an out-of-loop evaluation of the temperature excursion.

The stability performance of the temperature controller at T_1 is measured at the active heat shield. Fig. 4.4 shows the in-loop relative instability of the temperature σ_T^1, which decreases over time. In order to evaluate the effect of the time constants (first parameter discussed above), and thus the cavity temperature fluctuation, three different pairs of first order low pass filters (see Eq. 4.12) are applied to the FFT of T_1. The first case corresponds to the calculated time constants of our cavity housing ($\tau_1 = 3.9$ days and $\tau_2 = 5.9$ days), the second case corresponds to the measured time constants in our system ($\tau_1 = 0.6$ days and $\tau_2 = 2.5$ days), and the third corresponds to the estimated single time constant for the case of having no heat shield in the system with $\tau_1 = 0.2$ days and $\tau_2 = 0$. Fig. 4.4 compares the Allan deviation of the relative temperature fluctuation at the cavity σ_T^c for the three filter types in order to show the influence of heat-shielding and the different time constants.
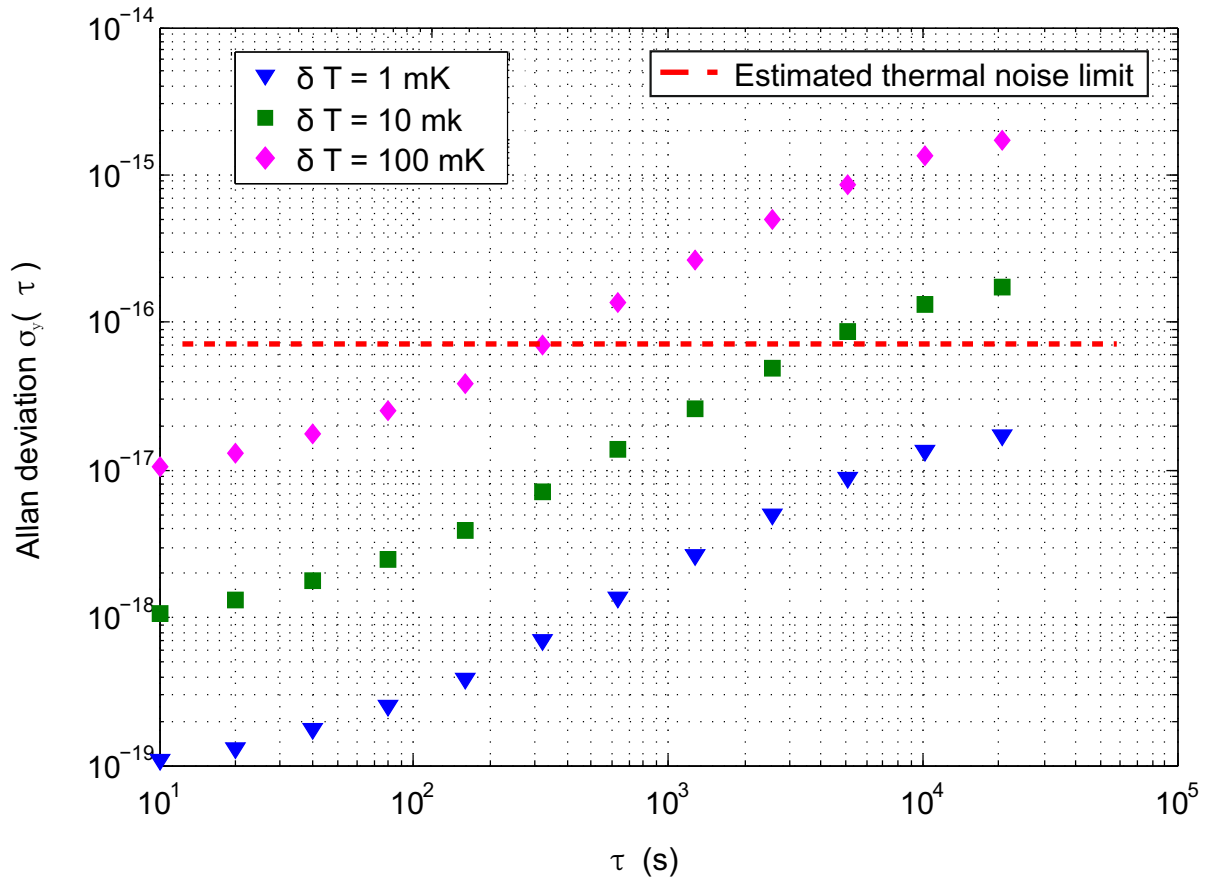
Figure 4.5: Allan deviation of the fractional frequency fluctuations as a function of the averaging time τ, calculated for the cavity temperature fluctuation σ_T^c of case (2) (where $\tau_1 = 0.6$ days and $\tau_2 = 2.5$ days, see Fig. 4.4), and for three different temperature shifts $|\delta T|$ from the cavity CTE null temperature. The results are compared with the thermal noise fundamental limit of the cavity stability (red dashed line). For temperature shifts $|\delta T| < 10$ mK, the temperature fluctuations do not limit the cavity stability for time scales shorter than 5000 s.

The Allan deviation of the fractional frequency fluctuations is calculated using Eq. 4.11 and the cavity temperature instability (calculated with the measured time constants of our system,

case (2) of $\tau_1 = 0.6$ days and $\tau_2 = 2.5$ days, see Fig. 4.4), for three different temperature shifts from the CTE null temperature of the cavity $|\delta T| = 1$ mK, $|\delta T| = 10$ mK and $|\delta T| = 100$ mK. The results are plotted in Fig. 4.5. This shows that for a temperature shift of 10 mK or less
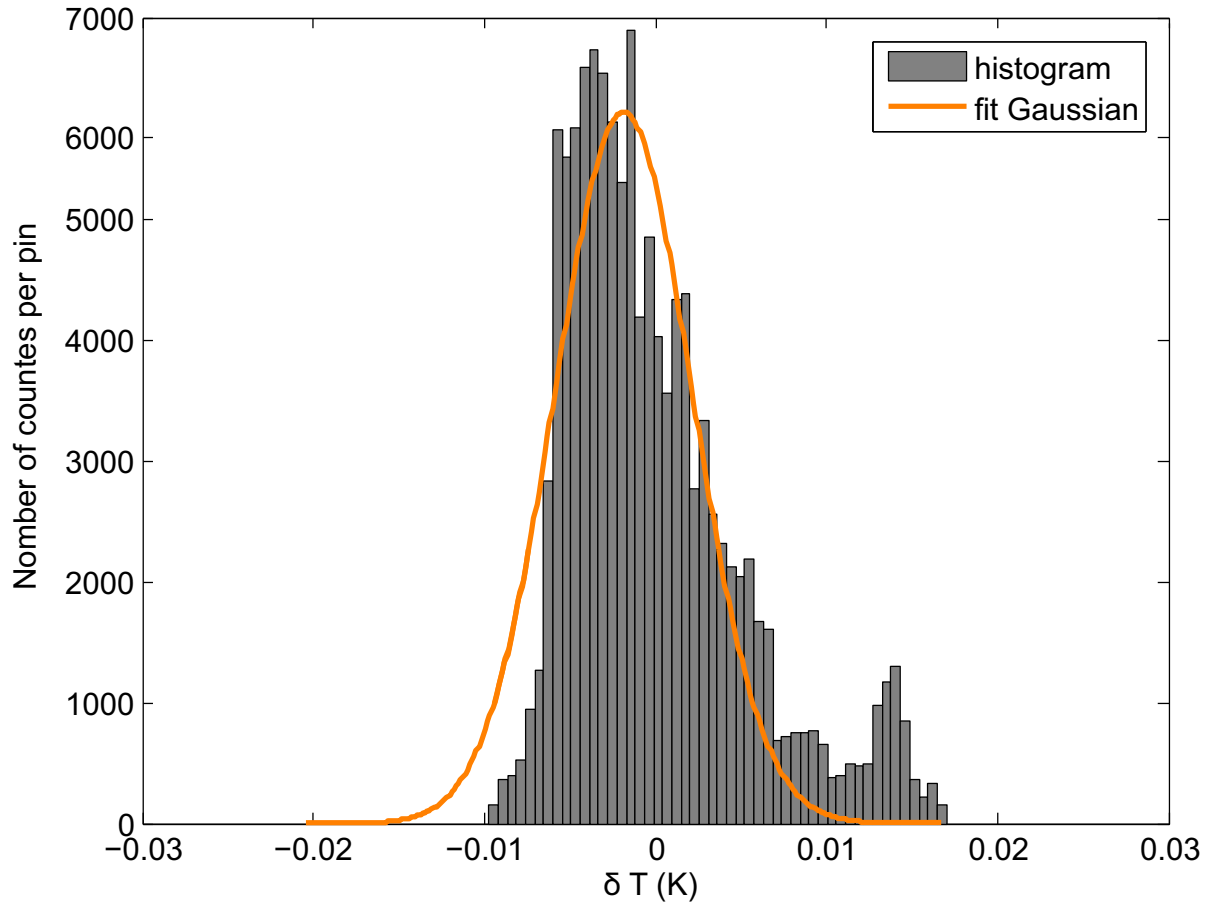
Figure 4.6: Histogram of the temperature excursion $\delta T = T_2 - T_0$ measured at the level of the passive heat shield. It shows an asymmetric temperature distribution (the heating process is faster than the cooling process due to the use of a heating wire for temperature stabilization) that can be approximated by a normal distribution with a standard variance of about 4 mK.

from the cavity CTE, the temperature fluctuation will not limit the cavity stability at time scales shorter than 5000 s. In order to observe the temperature excursion around the CTE-null point, a temperature sensor[15] (out-of-loop) placed on the passive heat shield (at T_2) was used for recording the temperature fluctuation over 15 days. A histogram of this data is plotted in Fig. 4.6. It shows a temperature excursion on the order of 4 mK. Thus, temperature fluctuations of the cavity are suppressed to a level below the thermal noise limit for integration times up to 2×10^4 s.

---

[15]It should be removed in order to maximize the thermal isolation.

4.1.2 Mechanical Vibration isolation

We showed in section 3.3 FEM simulations performed to obtain a mounting design of the 39.5 cm long cavity which permits low sensitivity to environmental acceleration vibrations.

The cavity housing system has been described in Sec. 4.1.1. Here, we start by presenting the ULE spacer that was machined as well as the measured machining and mounting tolerances. After that, we present the measurement technique used to evaluate the cavity vibration sensitivities in all three directions. We show and discuss results of the cavity vibration sensitivities obtained with two different mounting strategies. The measurement results of the spectrum of the mechanical and acoustic noise between 0.1 and 100 Hz in our laboratory environment and on the vibration isolation platform are shown in the third subsection. Finally we present the effect of vibration in terms of fractional frequency instability and compare its Allan deviation to the estimated thermal noise limit of the cavity.

ULE spacer machining

In section 3.3, we estimated that under acceleration forces of few μg, a cavity relative length change below the expected thermal noise limit ($\frac{\Delta L}{L} < 10^{-16}$) is achievable if the machining tolerances are in the order of a few hundred μm. The ULE cavity spacer machining was performed by a specialized company[16]. The ULE material was provided by our group. It is worth mentioning that drilling the optical hole in a cubic ULE spacer that is 39.5 cm long (width and depth 7.4 cm), was not possible without cutting the spacer into halves, due to the sensitivity of the glass material[17]. After performing a precise and centered drill in each half, the two pieces were optically contacted again. The cavity design can be found in Appendix D.

The precision of the machining was verified by sending the cavity to a specialized measurement division within PTB[18]. The machining tolerances (on the surface parallelism, optical contact of the two halves, centering of the optical hole, etc.) are below 50 μm. However, the most significant machining error of 90 μm was found in one of the four cut-outs of the cavity. This corresponds to the δdy tolerance (see Sec. 3.3.1), and is within the acceptable machining tolerances.

The optical contact of the mirrors to the center of the optical hole of the spacer (See 4.2.1) was made within an estimated precision error of 60 μm[19]. This corresponds to a Δr (see Sec. 3.3.1) shift between the optical axis and the geometrical center of the cavity, which is also within the acceptable machining tolerance.

The positioning of the cavity support was performed manually. An electronic caliper is used to measure δdz and δdx with a positioning precision of up to 100 μm (see Sec. 3.3.1).

---

[16]Optrovision

[17]This was the case in 2011; since then some companies specialized in silicon machining started to offer drilling long holes in ULE glass.

[18]Tactile technique (ZEISS Calypso). Credit to Dr. Norbert Gerwien.

[19]Measurement of the position of the mirror was made using an electronic caliper

Vibration sensitivity measurement technique

In order to determine the vibration sensitivity of the optical cavity, we record at the frequency shift of the laser when locked to the cavity as a function of an applied acceleration in all three directions. For this purpose, a 10 cm long cavity is used as a frequency reference. The optical set up is illustrated in Fig. 4.7.
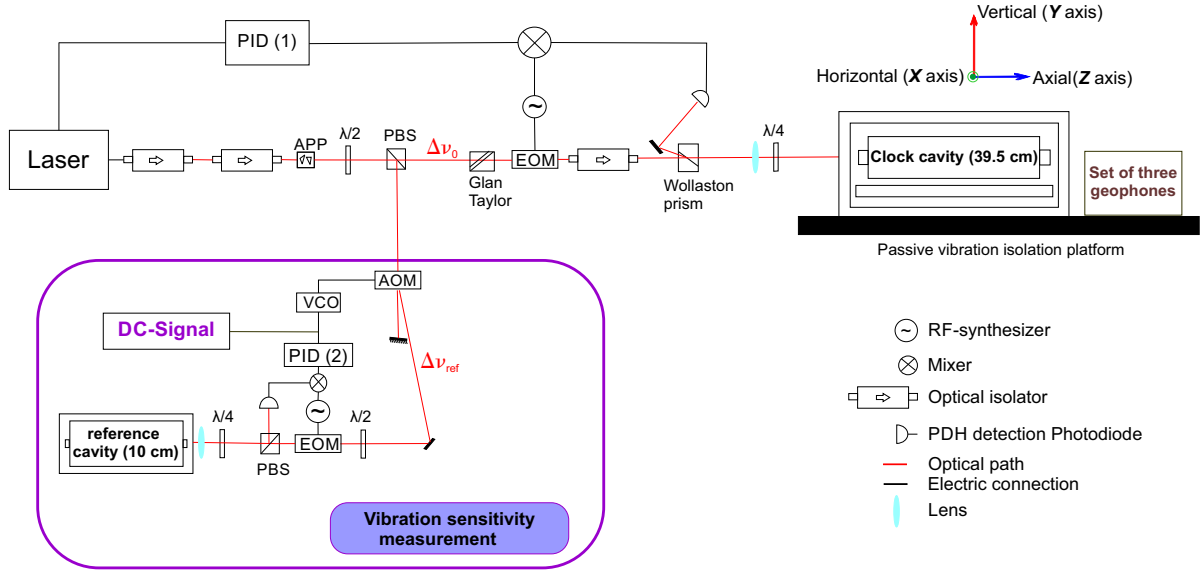
Figure 4.7: Optical set-up used for the 39.5 cm optical cavity vibration sensitivity measurements. One path of the laser is sent to the 39.5 cm cavity and the other path is sent to a 10 cm long reference cavity used for the vibration sensitivity measurement (delimited by purple box). The laser is locked to the long clock cavity, and then shifted by an Acousto-Optic Modulator (AOM) toward a resonance frequency of the short reference cavity. The AOM frequency locking signal is then used to identify the main laser frequency shift due to the vibration of the 39.5 cm long clock cavity. Both cavities are inside vacuum chambers (below 10^{-5} mbar). PBS : Polarizing Beam Splitter, APP : Anamorphic Prism Pair, PID (1) and PID (2): Proportional-Integral-Derivative controllers used for the first (clock cavity: 39.5 cm long) and second (reference cavity: 10 cm long) PDH frequency locks at $\Delta\nu_0$ and $\Delta\nu_{ref}$ respectively.

We separate the laser beam of frequency ν into two paths: one to be locked to the resonance frequency ν_0 of the 39.5 cm long cavity using the PDH lock technique (See section 2.4), and the second to be shifted by an Acousto-Optic Modulator[20] (AOM) toward a resonance frequency of the 10 cm reference cavity, ν_{ref}. We drive and scan the AOM's RF-frequency using a Voltage-Controlled Oscillator (VCO)[21]. A second PDH lock uses this VCO as an actuator to lock the laser (originally stabilized to the 39.5 cm cavity) to the reference cavity resonance. This way the first beam path is frequency locked at ν_0 and the second beam is locked at ν_{ref}. When the 39.5 cm long cavity undergoes vibrations, the optical path length of the cavity

---

[20]Type: Inc. AOMO 3200-1117, Crystal Technology.

[21]Marconi 2023B Signal Generator. We use the DC modulation input to correct the RF frequency output sent to the AOM

changes and thus the source laser frequency shifts by $\Delta\nu$. The amplitude of the frequency shift depends on the amplitude of the acceleration applied to the cavity. The reference cavity PDH system (originally locked at ν_{ref}) is subject to the same frequency shift via the laser source and the PID (noted PID(2) in Fig. 4.7) corrects for it by applying a correction voltage to the VCO proportional to $\Delta\nu$. Using the calibrated VCO conversion factor in [Hz/V], we calculate the frequency shift $\Delta\nu$ applied to the AOM (in [Hz]) as a function of the voltage correction signal (in [V]) obtained from the PID.

We place three identical vibration sensors (geophones[22]) pointing in the three directions of the lab: vertical (Y), horizontal (X) and axial (Z), as shown in Fig. 4.7, and identical to the orientation used in Chap. 3. The 39.5 cm long cavity is resting on a passive vibration isolation platform[23], while the reference cavity together with the laser source[24] are placed on an optical breadboard[25].

Once the laser is locked in the first path to the 39.5 cm long cavity and in the second path to the 10 cm long cavity, we manually apply oscillation movements (frequency $\approx$ 1 Hz) in the three directions independently. The geophones provide a voltage signal proportional to the applied acceleration with a (linear) sensitivity of 0.1 g/V (g = 9.8 ms^{-2}) between 0.1 and 100 Hz. The DC correction signal (from PID(2) in Fig. 4.7), in addition to the signals from the geophones, are recorded via an oscilloscope.

An example of the measurement results is plotted in Fig. 4.8 where the recorded voltages are converted to the corresponding accelerations (for the geophones) and to fractional frequency deviation (for the PID). By applying an acceleration in the axial direction a_A, the corresponding axial geophone records a large oscillation signal (in blue) while the other two (vertical geophone signal a_V in red and horizontal signal a_H in green) have minimal oscillations. The fractional frequency deviation $\Delta\nu/\nu_0$, where $\Delta\nu$ is the frequency shift correction applied to the AOM, is plotted in purple. The sensitivity to axial acceleration is then obtained by solving the equation:

$$\frac{\Delta\nu}{\nu} - \sum_{j=A,H,V} a_j s_j = 0 \qquad (4.13)$$

where s_j is the cavity sensitivity to acceleration in the direction j (A: axial, V: vertical, H: horizontal) per 1/g [1/g] (g = 9.8 ms^{-2}), and at a specific support point. It is different from k_j (coefficient of relative cavity length change [1/(g·m)]) and κ_j (coefficient of mirrors tilt [1/(g·m^2)]) that are the cavity sensitivity to machining tolerance δdy, δdz and Δr under a_j, as described by Eq. 3.8. However, the value of s_j results from machining tolerances and other effects that can influence the cavity symmetry (i.e spacer inhomogeneity, force unbalancing etc.).

In our case, we can change the parameter δdz by moving the supporting point along the Z (optical) axis, thus one can have an approximative idea about the actual κ_j of the cavity when a horizontal or a vertical acceleration is applied, as well as the cavity sensitive to δdz under

---

[22]High sensitive accelerometer, with ceramic flexural ICP, working range 0.1 to 200 Hz, model:393B31PCB, Signal Conditioner (Model 480B21), Piezotronics.

[23]vibration isolation platform type 250BM-1, Minus-K.

[24]Toptica: SYST DL PRO, Semiconductor laser diode: LD-1060-0150-AR-1.

[25]Thorlabs PBI51506 with enhanced vibration damping effect
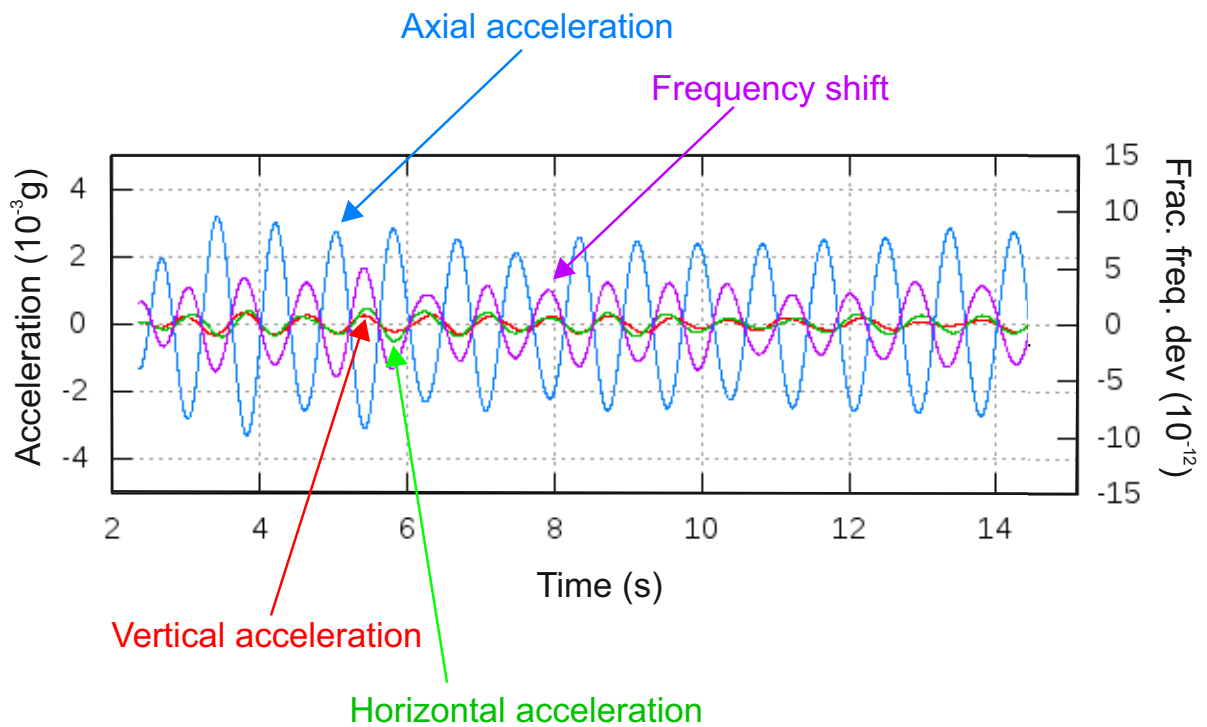
Figure 4.8: Vibration sensitivity measurement signals. The blue, green and red signals show the axial, horizontal and vertical accelerations respectively, as a function of time while shaking the cavity along the axial direction. The purple signal is the vibration induced fractional frequency deviation ("Frac. freq. dev"). All signals are band pass filtered around the shaking frequency (1 ± 0.5 Hz) to reduce the detection noise. These results belong to the 4-legged support (See Fig 4.9). The results correspond to an axial vibration sensitivity of 15.1×10^{-10}/g with a VCO conversion factor of 5 Hz/mV.

axial acceleration which was found to be negligible in the FEM simulations (See Tab. 3.2). By solving Eq. 4.13, we take into account the residual coupled motion between the different accelerations. The phase shift between the acceleration signal and the fractional frequency deviation signal is neglected in Eq. 4.13. In fact, in most of our recorded data this phase is π (this means there is a (-) sign in front of Eq. 4.13) or negligible (≈ 0 phase shift). This is possible because the coupling between the motion in different directions is small. If the coupling is strong (i.e. rotation of the cavity) then the phase shift between the different signal increases and Eq. 4.13 is no longer valid. This method of measuring the 39.5 cm long cavity vibration sensitivities is applied for two different cavity mounting strategies and the results are compared to the FEM simulations presented in Sec. 3.3.

Vibration sensitivity measurement results

The mounting of the cavity is important for minimizing its vibration sensitivity. We have found by means of FEM simulations four points from which we can support the cavity with minimum cavity length change under accelerations, however unbalanced force loading between the different supporting points increases the cavity vibration sensitivity compared to the ideal simulation model (see Sec. 3.3). Two different mounting strategies are evaluated in order to select the optimum cavity support scheme. The first strategy is supporting the cavity with four
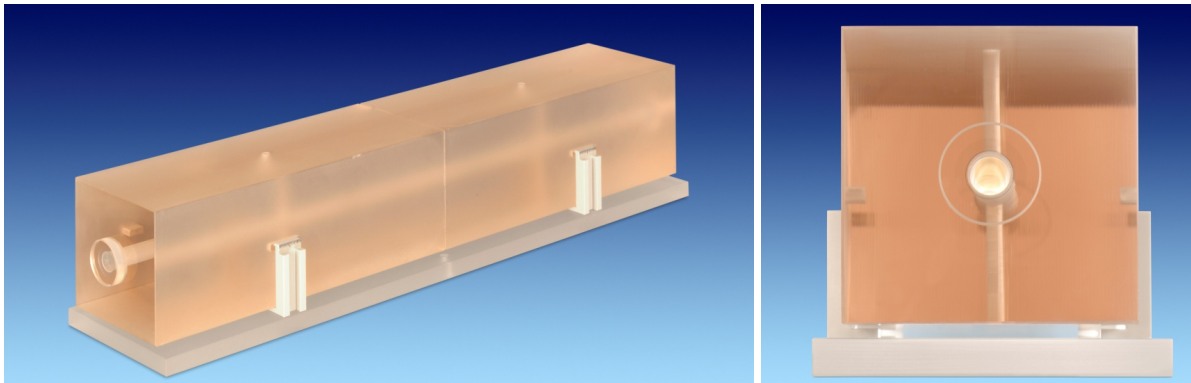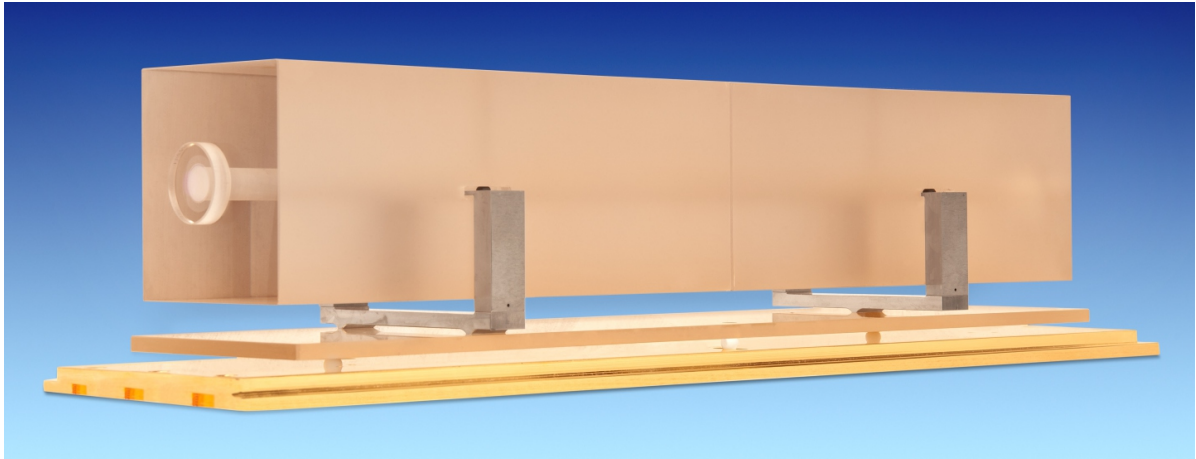

Figure 4.9: The 39.5 cm long optical cavity supported with the first mounting strategy. Four C-shaped legs made of Peek are placed on a 1 cm thick ULE plate and support the cavity from the four cut-outs. The viton pads between the spacer and the legs where not placed when these pictures were taken. The details of the cavity geometry are in Fig. 3.4.

viton (elastomer) half spheres of diameter ≈ 4 mm (estimated contact surface with the spacer ≈ 12 mm^2) placed on top of four C-shaped legs made of Peek (Polyetheretherketone). The use of viton[26] between the spacer and the supporting legs softens the support and improves the force distribution among the supporting legs. It also reduces the cavity sensitivity to high-frequency vibrations, particulary in the vertical direction [94]. The four legs are then placed on a 1 cm thick plate made of ULE (same material as the spacer of the clock cavity) so that the dis-

---

[26]Viton is a vacuum compatible, highly viscous elastomer with high surface tension. Below 100°C, viton has less than 10% compressibility [96]. It also has the capacity for remembering its original shape for a long time.

tance between the legs remains constant even after temperature variation. We support the cavity from the four cut-outs as explained in Sec. 3.3 (See Fig. 3.4). Figure 4.9 shows a picture of the cavity resting on the four-leg mounting. The VCO conversion factor is set to 15 Hz/mV, and the frequency of the applied vibrations is around 1 Hz. The measured vibration sensitivities s_j at optimized support positions ($dz = 82.6$ mm) are: $1.1(2) \times 10^{-10}$/g in the vertical direction, $14.0(4) \times 10^{-10}$/g in the horizontal direction and $15.1(3) \times 10^{-10}$/g in the axial direction. The cavity was fabricated with machining tolerances on the parameter δdy (See Fig. 3.4) of below 100 μm, giving an estimated sensitivity to vibration on the order of 10^{-11}/g assuming equal forces on all four support points (See Tab. 3.2). However, the measured results are one order of magnitude higher. This can be explained by the fact that supporting the cavity with four independent legs induces an unequal distribution of forces between the four supporting points, in agreement with the estimations presented in Sec. 3.3.3.

To overcome this problem, a second mounting strategy was implemented, consisting of converting the four supporting points into three with equalized force distribution.


Figure 4.10: The 39.5 cm long optical cavity supported with the second mounting strategy. Two U-shaped Invar supports are placed between the cavity and a 0.5 cm thick ULE plate, which is thinner than the original ULE plate for reasons of alignment with the vacuum chamber windows. The first half of the cavity is fixed in all directions and rotations, due to the two contact-cylinders on the bottom of the first U-shaped support. The second half of the cavity has a free degree of rotation around the central axis of the cavity due to the single contact-cylinder placed at the center of the bottom of the second U-shaped support. Two of the viton half-spheres between the Invar supports and the ULE cavity are visible in these pictures (in black).

Fig. 4.10 shows the second mounting strategy. The four viton half spheres are now placed on top of two U-shaped supports made of Invar (nickel-iron alloy) which is a low thermal expansion material[27]. The first U-shaped support has two contact-cylinders at the bottom while the second one has only one contact-cylinder in the middle, to allow free movement of half the spacer toward an equilibrium of force load. The two supports are placed directly

---

[27]Linear coefficient of thermal expansion: 10^{-6}/K.

on top the ULE plate. The technical drawings of the Invar supports and corresponding ULE plate are in Appendix D. This mounting method is convenient for an automatic balancing of the forces between the four cut-outs, and thus approaching the theoretical idea of equal force distribution assumed for the FEM simulation.

In order to study the effectiveness of this second supporting method, several vibration sensitivity measurements are done with the viton half spheres at different points along the Z (axial) direction. This is equivalent to what is done in the FEM simulation in Sec. 3.3 by varying δdz with respect to the optimum position of $dz = 82.6$ mm. In the simulations the cut-out position is shifted, whereas here we only move the supporting point within the cut-out (the position of the viton half sphere).
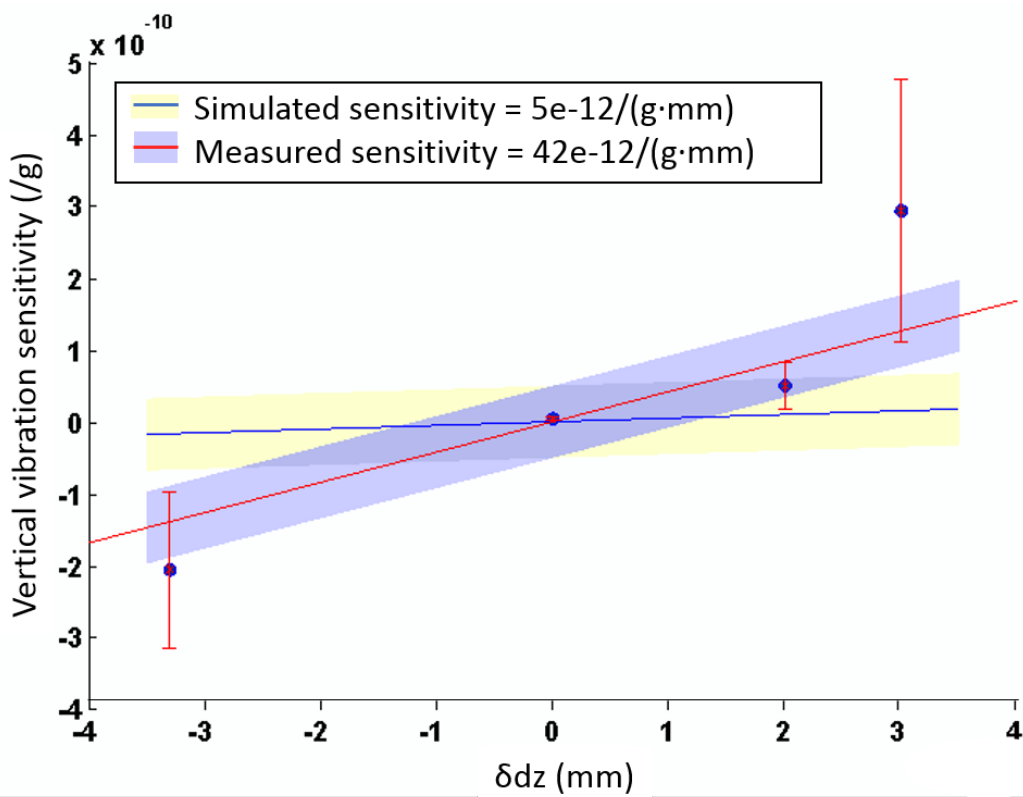
Figure 4.11: Sensitivity of the cavity to vertical acceleration as a function δdz position of the supporting point along the optical axis. The measured cavity vertical acceleration sensitivity as a function of δdz (blue circles) is given a sensitivity of $\kappa_Y \cdot \Delta r = 42 \times 10^{-12}/(g \cdot mm)$ (red line). The linear fit is obtained by using a non-linear least squares analysis. The error bars on the measured points represent the statistical error calculated by repeating the measurements 5 times at each position. The FEM simulated cavity sensitivity to vertical acceleration (blue line) is $\kappa_Y \cdot \Delta r = 5 \times 10^{-12}/(g \cdot mm)$, taking into account a mismatch between the cavity optical axis alignment with the geometric center of the cavity of $\Delta r = 60\mu m$, no error in the cut-outs machining ($\delta dy = 0$) (see Sec. 3.3), and a FEM simulation error of $5 \times 10^{-11}/(g \cdot mm)$ (dashed area).

The results of the vertical acceleration sensitivity as a function of δdz are plotted in

Fig. 4.11 and compared to the simulated sensitivity. The simulated sensitivity to δdz under vertical acceleration, as in Sec. 3.3, is $\kappa_Y \cdot \Delta r = 5 \times 10^{-12}/(\text{g}\cdot\text{mm})$ for $\Delta r = 60$ μm (estimated mismatch between the optical axis and the geometrical central axis of the cavity, discussed earlier). The results show that the 39.5 cm cavity sensitivity to δdz under vertical acceleration is $\kappa_Y \cdot \Delta r = 42 \times 10^{-12}/(\text{g}\cdot\text{mm})$. The measured sensitivity to the δdz is one order of magnitude higher than predicted by FEM simulation, which may be the result of either an asymmetry produced while manually placing the viton pads (i.e. variation in the depth with respect to the cut-outs δdx (see Sec. 3.3), a Δr higher than 60 μm, or both, in addition to an incomplete load balancing and inhomogeneous ULE material. Nevertheless we measure a minimum vertical vibration sensitivity for $\delta dz = 0$, in agreement with the position predicted by FEM simulations (see Sec. 3.3).
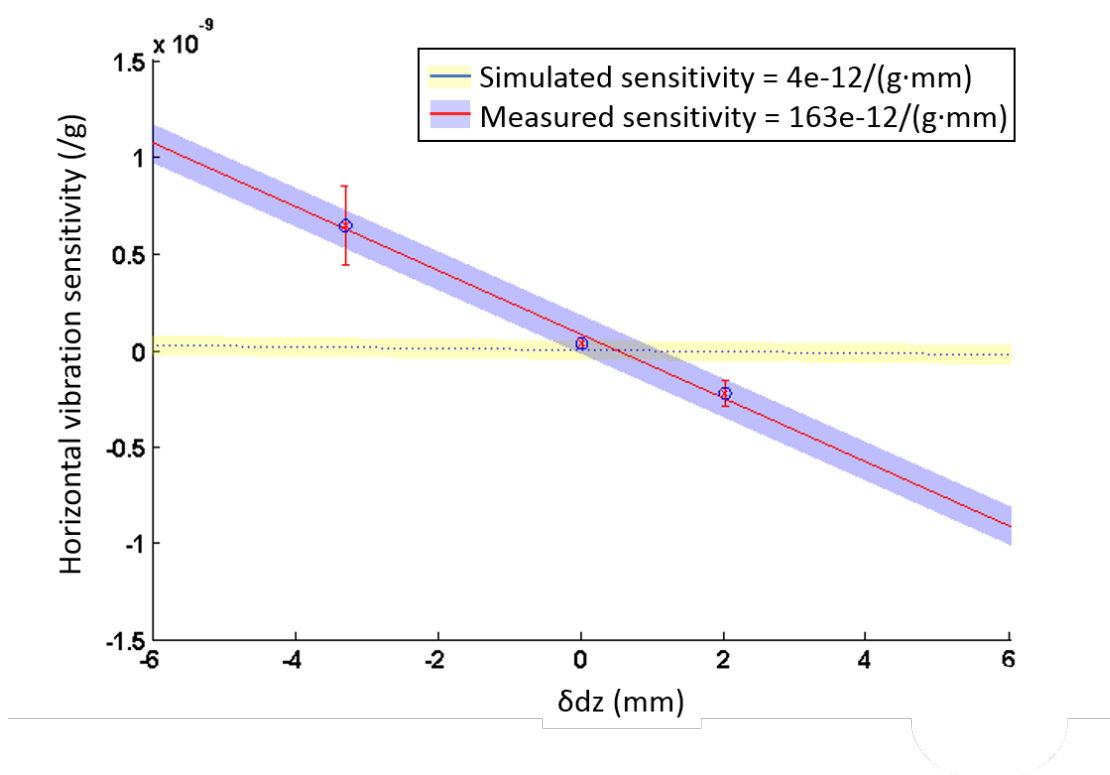
Figure 4.12: Sensitivity of the cavity to horizontal acceleration as a function δdz position of the supporting point along the optical axis. The measured cavity vertical acceleration sensitivity as a function of δdz (blue circles) gives a sensitivity of $\kappa_X \cdot \Delta r = 163 \times 10^{-12}/(\text{g}\cdot\text{mm})$ (red line). The linear fit is obtained by using a non-linear least squares analysis. The error bars on the measured points represent the statistical error calculated by repeating the measurements 5 times at each position. The FEM simulated cavity sensitivity to horizontal acceleration (blue line) is $\kappa_X \cdot \Delta r = 4 \times 10^{-12}/(\text{g}\cdot\text{mm})$, taking into account a mismatch between the cavity optical axis alignment with the geometric center of the cavity of $\Delta r = 60\mu$m, no error in the cut-outs machining ($\delta dy = 0$) (see Sec. 3.3), and a FEM simulation error of $5 \times 10^{-11}/(\text{g}\cdot\text{mm})$ (dashed area).

The sensitivity of the cavity to horizontal acceleration as a function of the supporting po-

sition along the Z axis δdz, is measured as well. The results are presented in Fig. 4.12 and compared to the simulation results. These measurements show that the cavity sensitivity to δdz under horizontal acceleration $\kappa_X \cdot \Delta r = 163 \times 10^{-12}/(\text{g·mm})$, which is about two orders of magnitude higher than the simulated result of $\kappa_X \cdot \Delta r = 4 \times 10^{-12}/(\text{g·mm})$ (for $\Delta r = 60\mu\text{m}$). This discrepancy can be due to an asymmetry that accrues while manually positioning the viton pads with respect to the middle plane (Y,Z) as in the case of the vertical vibrations. The results also show that it is possible to operate the cavity at $\delta dz = 0$, (where the effect of the vertical acceleration is minimal) with a sensitivity to horizontal acceleration below $10^{-10}/\text{g}$.
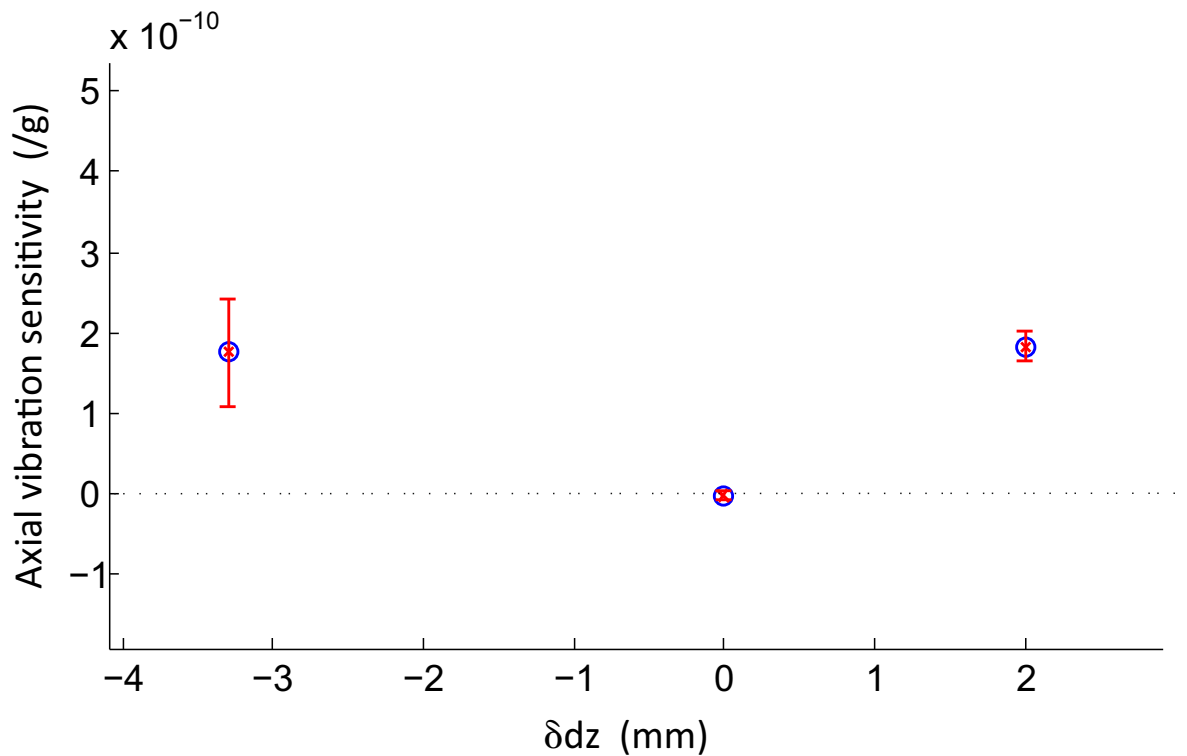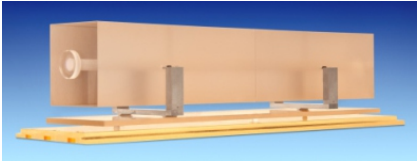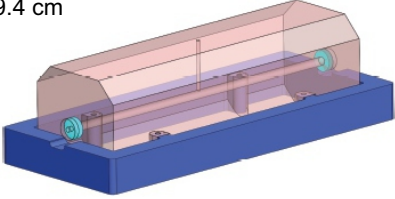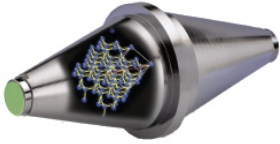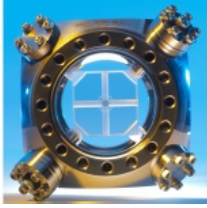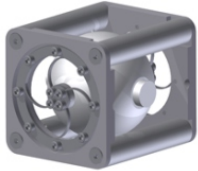

Figure 4.13: Sensitivity of the cavity to axial acceleration as a function δdz position of the supporting point along the optical axis

In the case of axial acceleration applied to the cavity, the FEM simulation shows that the cavity is insensitive to δdz in first order (see Tab. 3.2). The measured results of the axial acceleration sensitive to δdz are shown in Fig. 4.13. Results show that cavity fractional frequency changes did not flip sign as a function δdz in the case of an applied axial accelerations, and that the cavity sensitivity to axial accelerations s_A increases to above $10^{-10}/\text{g}$, when supported at $|\delta dz| > 2$ mm. This may be due to the spacer inhomogeneity. However, from the measurements, one can conclude that the minimum sensitivity to axial accelerations is obtained for $\delta dz = 0$, thus at the calculated optimum supporting point.

Finally, we support the cavity using the second mounting strategy at optimum $dz = 82.6$ mm found by FEM simulation and approved by the measurements. A residual error of $\delta dz \pm 100\ \mu$m from the viton pads positioning is assumed. The measured cavity sensitivity of the cavity to vertical, horizontal and axial acceleration is $s_V = 3(2) \times 10^{-12}/\text{g}$, $s_H = 12(3) \times$

	Sensitivities		
	Vertical $\times 10^{-12}$/g	Horizontal $\times 10^{-12}$/g	Axial $\times 10^{-12}$/g
L = 39.5 cm **A**	3 (2)	12 (3)	2 (1)
L = 39.4 cm **B**	1400	80	–
L = 21.2 cm **C**	67	84	55
L = 5 cm **D**	<1	2	25
L = 5 cm **E**	55	35	1

Figure 4.14: Vibration Sensitivity Comparison. A: The cavity we study in this thesis. B: Cavity design from Swallows *et al.* [30], C: Cavity design used in Kessler *et al.* [63], D: Cavity design from Webster *et al.* [77]. E: 5 cm diameter spherical cavity designed by Leibrandt *et al.* [89], which has also shown a vibration sensitivity below 10^{-12}/g in all three directions using a real-time feed-forward cancellation of length fluctuations.

10^{-12}/g and $s_A = 2(1) \times 10^{-12}$/g, for a vibration frequency around ≈ 1 Hz. The new U-shaped supports allow an extra degree of freedom to the cavity that contributes to an equal force distribution over the four cut-outs. The results are then in good agreement with the simulated case in which all the supporting points have the same acceleration constraint. The performance of the 39.5 cm cavity results is compared in Fig. 4.14 to other experimentally realized cavities showing that this long cavity mounted with effective-3 point support strategy allows a vibration sensitivity as small as a 5 cm long cavity [77].

In order to reduce the fractional frequency instability due to vibrations below the thermal noise limit, the mechanical vibrations sensed by the cavity must be suppressed to below a μg. In the following we present the vibration isolation system of the cavity and the resulting fractional frequency instability in terms of Allan deviation.

Vibration isolation system

The cavity is placed on a passive Vibration Isolation Platform (VIP) to isolate vibrations of mechanical origin below 100 Hz. The VIP in turn is placed on top of a sand box[28] on an aluminum plate. The sand permits further isolation of the VIP platform from the floor. Finally, we operate the cavity in a 5 m^2 dedicated laboratory situated in the basement of our building to avoid vibrations and oscillation that might exist in the clock experiment laboratory situated at the 5th floor of the same building. We measure the acceleration amplitude spectral density on the floor of the laboratory and compare this to the spectrum on top of the VIP. The measurements are performed using three identical geophones pointing at the three directions of the lab: vertical, horizontal and axial (same convention of directions used in chapter 3.).

Figure 4.15 (a) shows that the vibration accelerations (mechanical and acoustic) are similar in all three directions. The VIP suppresses the vibrations between 0.2 Hz and 90 Hz. The isolation efficiency has been improved by ensuring that the load on the VIP approaches the weight of 123 kg required by the manufacturer as one can see in Fig. 4.15 (b).

The vertical acceleration on the VIP (with 125 kg load) were compared to the vertical accelerations on the floor of the laboratory. The transmissibility of the VIP is then obtained and compared to the manufacturer specifications [97]. The result plotted in Fig. 4.16, show that the VIP vibration suppression efficiency is about 20dB less then specified between 10 and 100Hz.

Results in terms of Allan deviation

The laser fractional frequency instability due to vibrations is calculated using the vibration noise spectrum of the cavity platform shown in Fig. 4.15 and the measured vibration sensitivities from Eq. 4.13. The power spectral density of the mechanical vibration noise spectrum in the direction j (A: axial, V: vertical, H: horizontal): $S_{vib}^{j}(Hz)$ [g^2/Hz] is converted into Allan deviation $\sigma_v^{j}(\tau)$ [g] using Eq. 2.7. Assuming no correlation between the vibrations in the three directions (H, V and A), and assuming that the vibration sensitivities s_j are independent of the

---

[28]775 Kg of sand with diameter <1 mm.
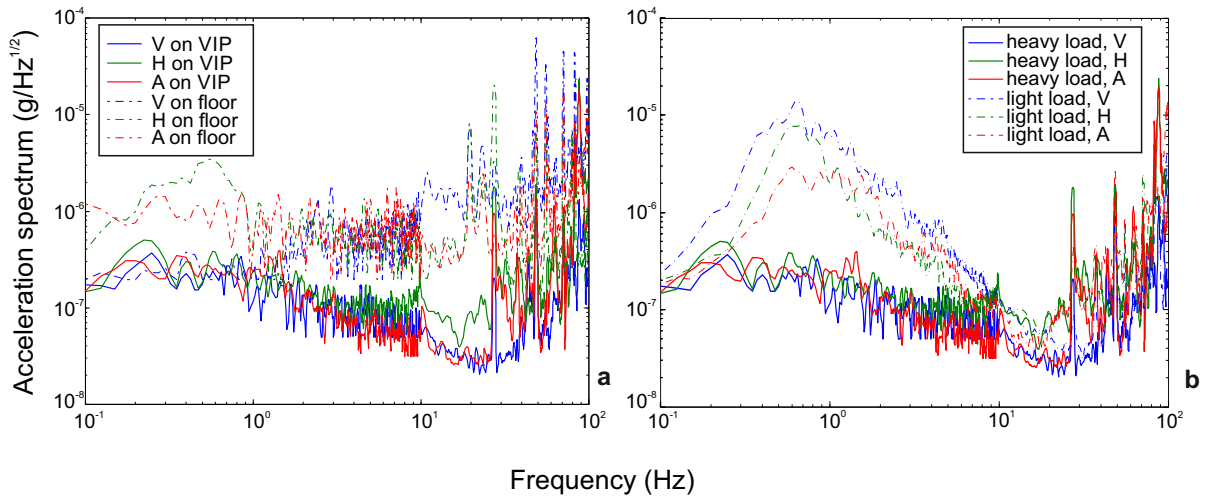
Figure 4.15: Measured amplitude spectrum of accelerations in the V: vertical direction, H: horizontal direction, and A: axial direction. (a) Comparison between the acceleration spectrum on the lab floor (dashed lines) and on the passive Vibration Isolation Platform (VIP) (full lines). There is no acoustic isolation around the VIP. (b) Comparison between the acceleration spectrum when the VIP is loaded with light load of ≈ 105 kg (dashed lines) and when it is loaded with a load of ≈ 125 kg (full lines), close to the specified maximum load.
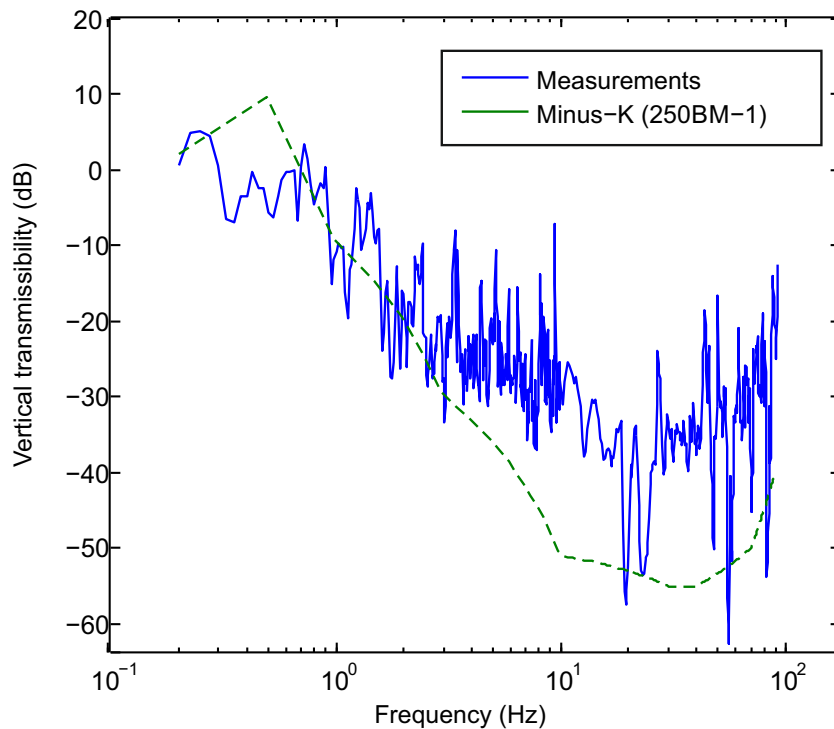

Figure 4.16: Transmissibility of the passive vibration isolation platform. The measurements (full line) correspond to the ratio between vibrations on VIP and vibration on the laboratory floor. The VIP transmissibility data specified by the manufacturer (dashed line) were taken from the specification data-sheet for Minus-K type 250BM-1.

vibration frequency, the fractional frequency instability can be written as:

$$\sigma_y(\tau) = \sqrt{\sum_{j=A,H,V} (\sigma_v^j(\tau) \times s_j)^2}. \tag{4.14}$$

The obtained Allan deviation is plotted in Fig. 4.17 as well as the calculated thermal noise limit of the cavity. The Allan deviation of the fractional frequency instability due to vibrations on the VIP is below the thermal noise limit for averaging times longer than 0.05 s.
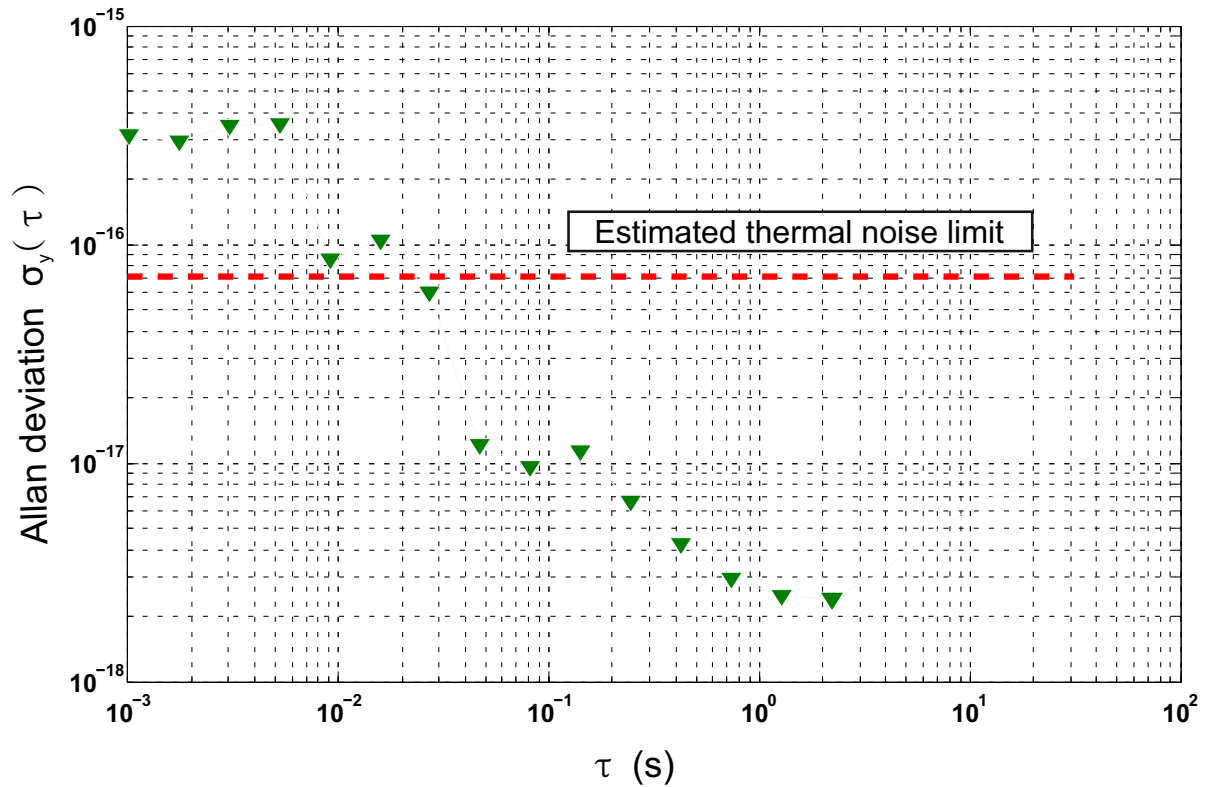
Figure 4.17: Vibration contribution to Allan deviation of the laser frequency stabilized to the 39.5 cm optical cavity as a function of the averaging time τ. The red dashed line is the thermal noise limit as estimated in Sec. 3.1.1.

We have shown in this section the realization of a 39.5 cm long cavity with a vibration sensitivity less than $10^{-11}/\text{m·s}^{-2}$ in all three directions. Thus, the residual mechanical vibrations, measured between 0.1 Hz and 100 Hz on the vibration isolation platform, will not limit the short term stability of the laser. We plan in the future to implement an acoustic vibration (frequencies higher than 100 Hz) isolation box around the vacuum chamber, since the effect of these vibrations on the cavity performance have not been taken into account in our evaluation.

4.1.3   Linear drift

Even though the cavity spacer is made of an ultra-low expansion material, and operated at the zero-crossing temperature for minimum thermal expansion as in Sec. 4.1.1, there persists

an additional limiting factor to the frequency stability, which is a linear drift in cavity length. In fact, the aging of the glass material manifests itself as a slow volume contraction over time [87]. The optical contacting of the mirrors also induces stress on the spacer material that settles over some years. This length drift effect is linear over averaging times $t - t_0$ of several days and one can write the linear temporal length (frequency) drift as [92]:

$$\frac{\Delta L}{L} = -\frac{\Delta \nu}{\nu} = \gamma(t - t_0) \qquad (4.15)$$

where γ is the temporal drift coefficient in [1/s]. In terms of Allan deviation, a simple relationship relates γ to the fractional frequency instability as $\sigma_y = \gamma/\sqrt{2} \cdot \tau$ [19].

For much longer times scales going up to some years, the drift rate decreases exponentially [87].

In our case, the optical contact of the mirrors on the 39.5 cm long cavity was made in June 2013. Two measurements of the short term linear drift of our cavity were performed and the results are shown in Fig. 4.18.
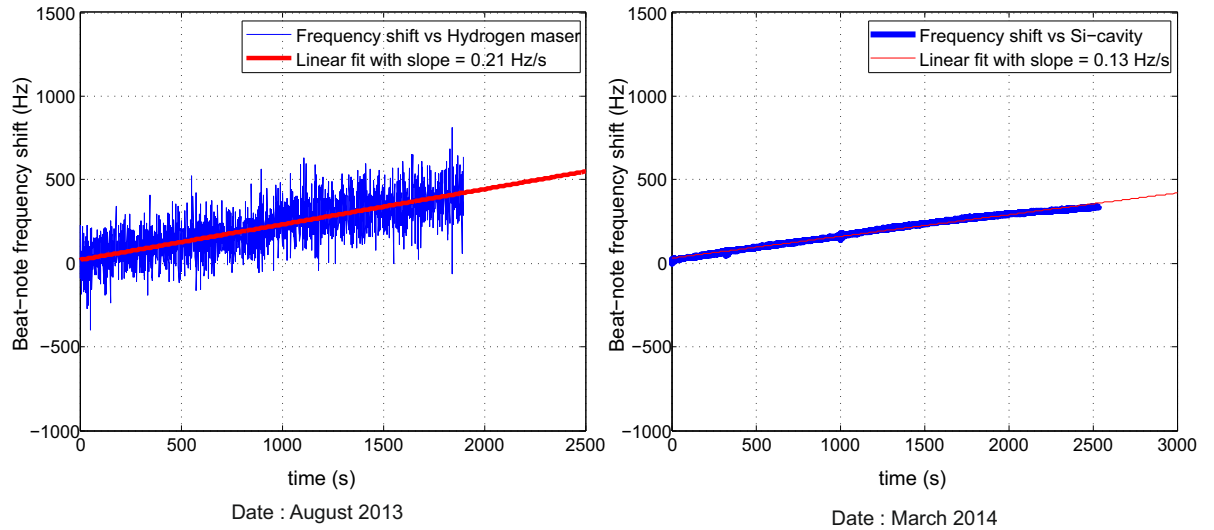
Figure 4.18: Linear drift of the laser frequency as a function of time. Left: Al vs H-Maser; refers to the measurement of the cavity linear drift from a beat-note frequency between our laser (Al) and the frequency comb stabilized to the Hydrogen maser (H-Maser), measurement made in August 2013. The data in this case is noisy due to the unstabilized fiber link. Right: Al vs Si; refers to the measurement of the cavity linear drift from a beat-note frequency between our laser (Al) and the stable laser based on a Silicon cavity (Si) [31], which has negligible linear drift, measurement made in March 2014. The fiber link in the second measurement was stabilized.

The first linear drift measurement was performed in August 2013. For this measurement, the laser, stabilized to the cavity, was transferred to the experimental laboratory (5th floor) via a 100 m fiber. As described in Sec. 4.1.1, a beat note between our laser and a frequency comb referenced to the Hydrogen maser was performed. A record of the beat-note frequency

counting over ≈ 35 min shows a linear frequency drift on the order of 0.21 Hz/s measured over 200 s, which corresponds to a fractional frequency stability of $\sigma_y(1\text{s}) = 5.3 \times 10^{-16}$.

The second measurement was performed in March 2014. For this measurement, the laser was transferred via a 350 m long fiber and compared to a second ultra-stable laser referenced to the silicon cavity [63] present at PTB via a frequency comb (for details see Sec. 5.1 and Sec. 5.2). The comparison beat-note frequency shows a linear drift of 0.13 Hz/s that corresponds to $\sigma_y(1\text{s}) = 3.3 \times 10^{-16}$. The silicon cavity used as a reference has a negligible linear drift ($\approx \mu$ Hz/s) [31].

This intrinsic drift of the cavity length is not avoidable and is the major reason for which we need an atomic reference for the long term stabilization of frequency standards (See Sec. 2.2). However, this drift is measurable, predictable and relatively slow; thus, it is possible to correct for it by taking it into account in the servo feedback while interrogating the atomic reference [98].

4.1.4 Pressure stabilization

Pressure fluctuations in the cavity vacuum chamber lead to a fluctuation of the refractive index in the air, Δn, and thus a fluctuation of the optical path length ΔL between the two mirrors, since $L = n \cdot L_g$ where L_g is the geometrical distance between the two mirrors. The relationship is described by:

$$\frac{\Delta L}{L} = -\frac{\Delta \nu}{\nu} \approx \Delta n. \tag{4.16}$$

For a 1070 nm laser wavelength and constant temperature[29] of $T = 45.5°$C, the Allan deviation of the refraction index σ_n as a function of the Allan deviation of the fractional pressure fluctuation σ_P is estimated[30] according to [99] by:

$$\sigma_n \approx 2.4 \times 10^{-7} \sigma_P/\text{mbar}. \tag{4.17}$$

This means that the fluctuation of the pressure should be below 10^{-10}/mbar in order to pose no limitation for a cavity at a thermal noise limit of 7×10^{-17}.

The housing system of the cavity is composed of two heat-shields and a vacuum chamber (see Sec. 4.1.1). The vacuum chamber, as well as the first heat-shields, are made of aluminum[31], a material known for its low outgassing and good vacuum properties. The second (inner) heat shield is made of brass[32] coated with gold, to make it suitable for ultra-low Vacuum. In order to remove water and other trace gases that could adhere to the aluminum, the vacuum chamber (with the aluminum heat shield placed inside) was heated under vacuum up to 150°C for three weeks[33]. After cleaning the ensemble of chamber and the two heat shields with an ultrasonic acetone bath, we place the cavity inside it and seal it using indium wire (1 mm diameter) as a gasket.

Using a turbo pumping station[34], the pressure inside the cavity housing is reduced to $8 \times$

---

[29]Temperature of minimum thermal expansion of the cavity as we will show in Sec. 4.1.1
[30]$n - 1 \approx 2.4 \times 10^{-7} P/\text{mbar}$
[31]The aluminum alloy 6061
[32]Aluminum Alloy made of copper and zinc
[33]Baking under vacuum $\approx 10^{-5}$mbar
[34]Pfeiffer Vacom, iCube.

10^{-7} mbar. An ion pump[35] is used to maintain a low pressure. By evaluating the ion pump current[36], we estimate that a final pressure of 2.4×10^{-8} mbar is reached, and its fluctuations are evaluated and converted into Allan deviation of the frequency using Eq. 4.17. The results are plotted in Fig. 4.19.

The Allan deviation shows that the pressure fluctuations induce fluctuation of the frequency below 10^{-17}, which means that for the current pressure of about 10^{-8} mbar we have a 1% fluctuation of the pressure with $\sigma_P \approx 10^{-10}$ mbar. Thus, pressure fluctuations in our cavity vacuum chamber do not limit the stability for measurement times shorter than 10^4 s.
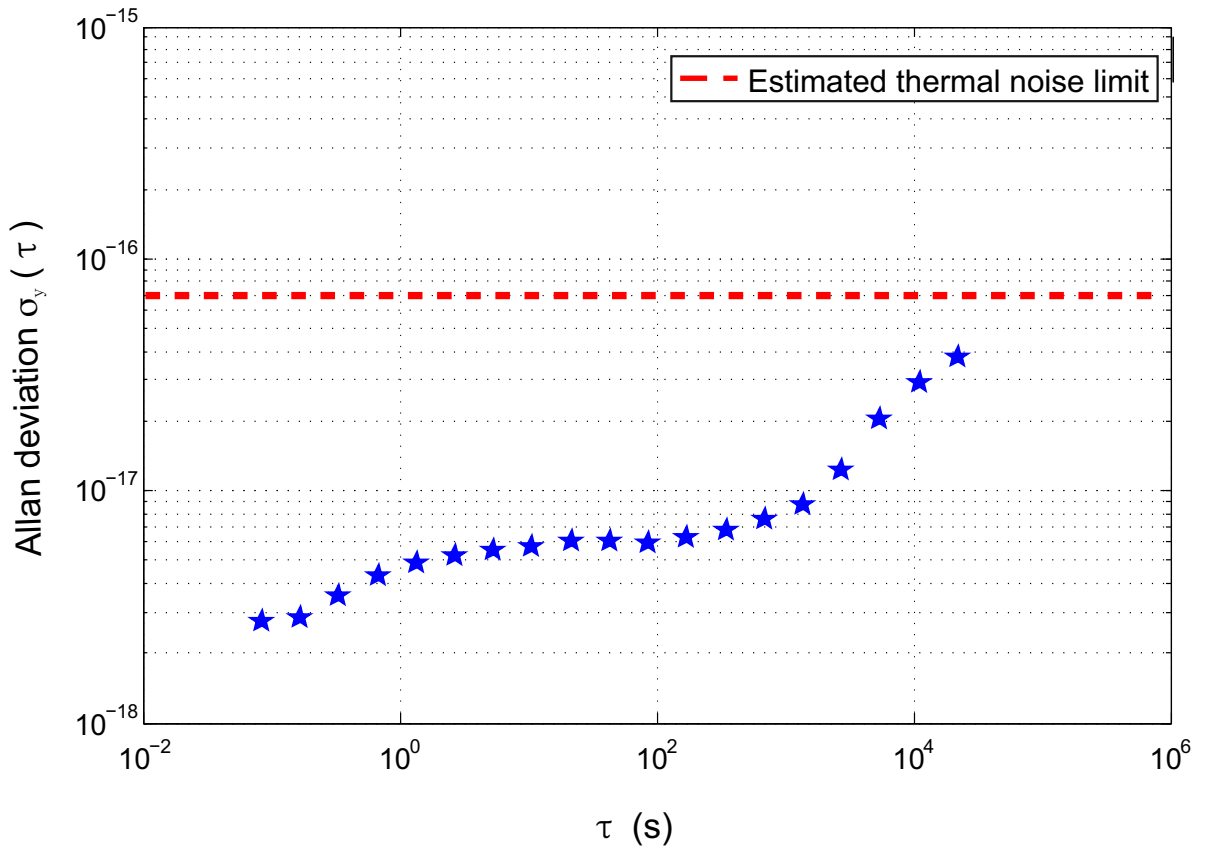
Figure 4.19: Pressure fluctuation contribution to Allan deviation of the laser frequency. The red dashed line is the thermal noise limit as estimated in Sec. 3.1.1.

[35]Type 20 l/s (VacIon Plus 20 StarCell)

[36]The controller of the ion pump (MiniVac Controller, 230V, Agilent) features of a DC-voltage output with 1 V = 1 mA, from the data-sheet of the ion pump we obtain the conversion factor of 1.7×10^{-3}, used for evaluating the pressure.

4.2 Laser stabilization to an optical cavity

4.2.1 High finesse optical cavity

In order to build an ultra-stable laser, the mirrors of the optical cavity the laser is stabilized to must be highly reflective. As shown in section 2.4, the sensitivity to laser frequency fluctuations is defined by the frequency discriminant D from Eq 2.34. Since the cavity has a fixed free spectral range for a fixed length, the linewidth of the cavity (See Eq. 2.16) can be reduced by increasing the cavity finesse.

For our experiment we chose to optically contact two highly reflective mirrors produced by ATFilms[37]. The substrate is made of Fused Silica (FS) coated with a 6 μm thik high reflective multi-layer Bragg reflector over an 8 mm aperture for the plane mirror substrate surface, and 12 mm for the concave (1 m Radius of curvature) mirror surface. The mirrors have a diameter of 2.54 cm (1 inch) and a thickness of 6.35 mm. The coatings are deposited by Ion Beam Sputtering (IBS). This kind of dielectric coating is known for its low absorption losses specified to less than 1 ppm. The mirror substrates are polished to a roughness of less than 10^{-10} m RMS. Roughness leads to scattering losses that limit the finesse. The coating has a high number of dielectric layers (≈ 40) which allow to have highly reflective mirrors. Cleaning the mirror coating is a delicate procedure that can be done with pure acetone. We use untouched (no additional cleaning), out-of-the-box mirrors, and we optically contact them to the center of the optical hole in the spacer using a metallic mask for alignment (see Fig. 4.20).
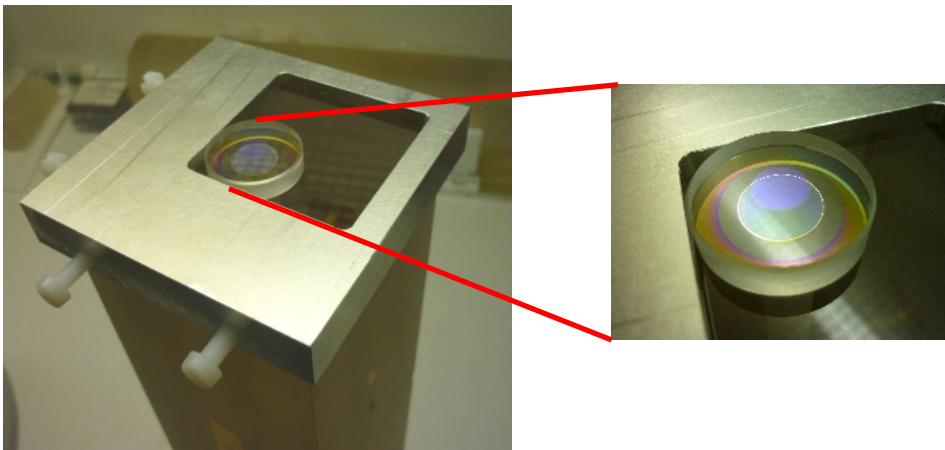
Figure 4.20: Pictures taken while contacting one mirror to the spacer. The interference fringes (colored rings around the center of the mirrors) disappear completely once the optical contact is established. The contacting was done in a laminar flow box for dust protection with the help of Dr. Thomas Legero (PTB).

It is possible to measure the finesse of the cavity using the exponential decay of the stored energy τ_s [100, 101]. The cavity storage time τ_s is the time required for a $1/e$ decay of the

---

[37]http://www.atf-ppc.com

cavity transmitted intensity. It is related to the finesse of the cavity $\mathscr{F}$ and its linewidth Γ by:

$$\tau_s = \frac{1}{\Gamma} = \frac{\mathscr{F}L}{c\pi}. \tag{4.18}$$

The experimental set-up for measuring the finesse shown in Fig. 4.21. When the transmitted intensity measured on the photodiode reaches a threshold set by the controller, a switch turns off the Acousto-Optic Modulator[38] (AOM) that acts as a fast shutter to stop the incident beam toward the cavity within about 1 μs.
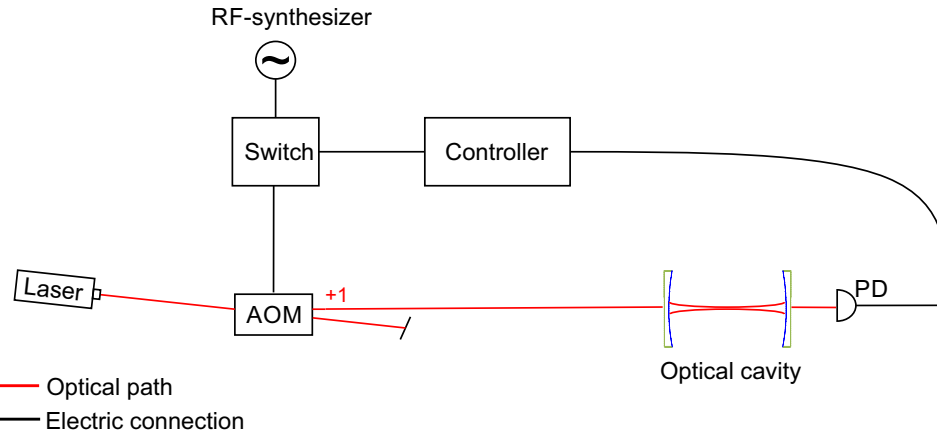
Figure 4.21: Sketch of cavity high-finesse measurement optical setup. AOM: Acousto-Optic Modulator, PD: photodiode.

We scan the laser over a fundamental mode (TEM$_{00}$) of the cavity with a 30% transmission efficiency[39], and under a vacuum pressure of 10^{-5} mbar. In Fig. 4.22 we show the transmitted voltage from the cavity after switching off the AOM. From the exponential decay time constant $\tau_s = 274.1 \pm 2$ μs we conclude that the finesse of our cavity is $\mathscr{F} = 650000 \pm 6,000$, corresponding to a mirror reflectivity of $R \approx 99.9995$. This finesse is only observable under vacuum; at room pressure absorption losses due to the air in the cavity limit the finesse to 420,000. From this result, we calculate a cavity linewidth of $\Gamma = 2\pi \times 580.6$ Hz. The narrow linewidth increases the frequency discriminant signal amplitude and thus optimizes the performance of the PDH lock.

4.2.2 Pound Drever Hall lock performance

We implement a PDH locking scheme, outlined in Sec. 2.4, to stabilize the 1070 nm wavelength laser to the 39.5 cm cavity. Stable locking of a laser to a cavity at a level better than 10^{-16} requires excellent control of a number of potentially detrimental effects (error signal asymmetry, phase shift between the PDH detection RF-signal and the local oscillator (see Sec. 2.4)), electronic noise and detection shot noise, laser intensity stability, residual amplitude modulation (RAM), etc.

---

[38]Type: Crystal Technology, Inc. AOMO 3200-1117
[39]Efficiency = output power/input power
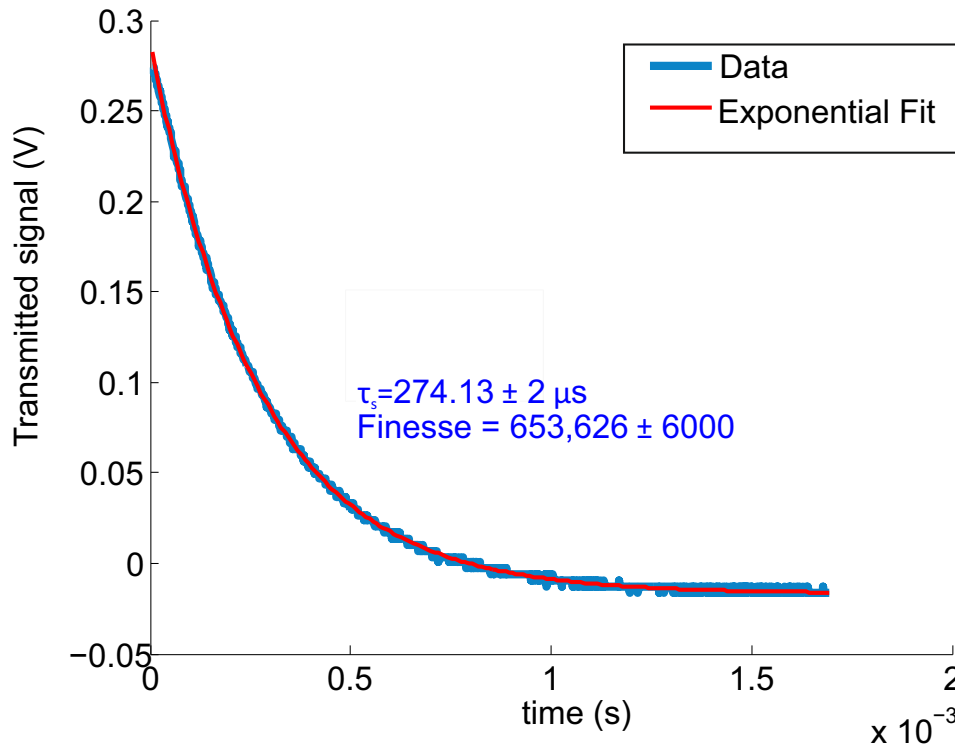
Figure 4.22: Cavity transmitted signal as a function of time. The time constant of exponential decay of the intra-cavity power gives a measurement of the cavity finesse. This measurement was done under vacuum pressure equal to 10^{-5} mbar. For measurements done at room pressure (1 bar) the time constant is in the order of 175 μs, which corresponds to a finesse of 420,000.

We start the section with a full description of the PDH optical and electronic settings of our experiment. At the end of the section we recall the fundamental limit of the PDH technique, which is the photodetection shot noise, and compare it to the achieved laser noise suppression. The performance of the PDH technique is then evaluated in terms of fractional frequency instability and compared to that of a free running laser and to the estimated thermal noise limit.

Optical setup

Fig. 4.23 shows a sketch of the optical and electronic setup used in the PDH laser stabilization scheme. The red line in this figure represents the optical path of the laser as it is in the experiment. The laser used is a grating stabilized external cavity diode laser (ECDL)[40] at a wavelength of 1070 nm and measured output power of 56 mW[41].

Two optical isolators [42] are placed after the diode laser head to suppress the reflected light from the cavity and the rest of the optics by more than 100 dB, to prevent laser disturbance the

---

[40]DL PRO, Semiconductor laser diode: LD-1060-0150-AR-1. Toptica Photonics AG.

[41]Power as of January 2014, for current set to 240 mA and temperature set to 19.9°C.

[42]Double stage Faraday isolator TGG ($>$ 60 dB isolation, 90% transmission) Altechna and IO-5-1064-HP (38-44 dB isolation, 93% transmission) Thorlabs.
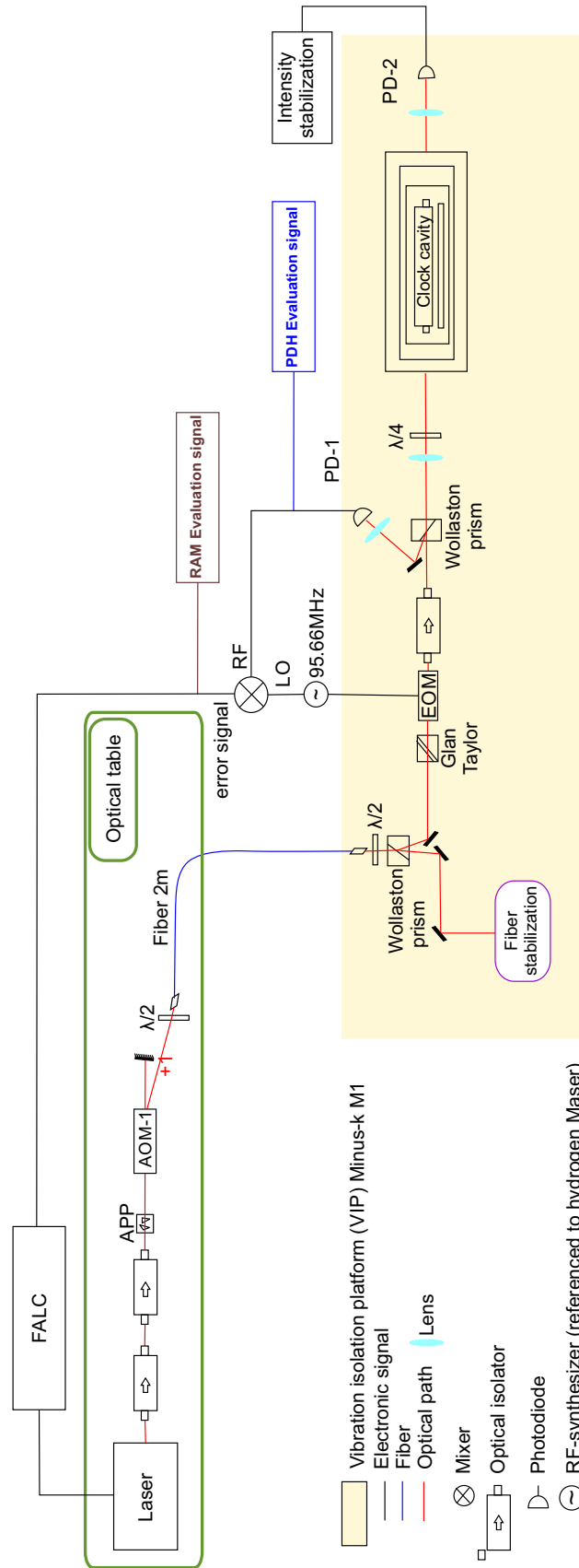
Figure 4.23: Sketch of the optical setup for the PDH laser stabilization to the 39.5 cm cavity. PD-1 is used as the PDH detection photodiode that generates the RF signal. PD-2 is used for monitoring the transmitted intensity and together with the AOM is used for the intensity stabilization (See 4.2.4). A more general overview of the setup is presented in Appendix C.

laser or even damage of the diode laser. They are followed by an anamorphic prism pair[43] to render the elliptic laser beam from the diode laser to a circular shape.

The laser is then sent to an Acousto-Optic Modulator[44] (AOM-1) that is used for intensity stabilization (see Sec. 4.2.4). A Phase Locked Loop stabilized crystal oscillator [45] referenced to a stable 10 MHz reference derived from a Hydrogen maser at PTB, is used as RF-synthesiser to generate the 200 MHz operating frequency of the AOM. The first-order diffracted beam (+200 MHz) is transferred from this first optical table to a second optical table that is mounted on top of the vibration isolation platform (VIP) of the cavity, via a 2 m long polarization-maintaining (PM) optical fiber[46] with 65% transmission efficiency. This table contains the optical setup related to the stabilization of the laser to the cavity (i.e. optical coupling, Electro-Optical-Modulator (EOM) for the PDH signal generation, photodiodes, intensity stabilization optics (Sec. 4.2.4), and fiber stabilization optics (Sec. 5.1). This compact system reduces the free space optical path and thus the sensitivity to air currents in the lab.

A half-wave plate ($\lambda/2$) is placed after the 2 m fiber, followed by a Wollaston prism[47] splitting the beam into two orthogonally polarized beams, where the first is used for the PDH stabilization while the second is sent to the clock experiment via a 120 m long fiber (see Sec. 5.1). The wave plate is used to adjust the power distribution between the two beams since only 10 to 30μW are needed for the cavity locking scheme, while the rest of the power is used for the clock experiment.

In order to realise the PDH lock (for theory see Sec. 2.4.), the laser is sent through an EOM to generate the modulation sidebands. At this stage residual amplitude modulation (RAM) is introduced, which needs to be minimized as described and evaluated in Sec. 4.2.3. The EOM [48] is based on a single $KTiOPO_4$ (KTP) crystal with a Brewster-cut (A small angle between the input and the output facets) to reduce the EOM crystal-induced RAM. A Glan-Laser Polarizer[49] is placed in front of the EOM for a high polarization purity along the principal modulation axis of the EOM. An additional optical isolator[50] is used after the EOM to prevent any etalon effect between the cavity and the EOM output facet (see Sec. 4.2.3).

Laser coupling to the cavity requires the incident laser beam to have the correct waist size focused on the flat coupling mirror and to be centered with respect to the geometrical center of the cavity mirrors for maximum cavity mode matching. The beam is collimated[51] at the output of the 2 m fiber and the size of the beam focus at the cavity incoupling flat mirror was adjusted using a focusing lens in order to match the calculated size (Eq. 2.22) of 291 μm (see Tab. 3.1.). A quarter wave plate ($\lambda/4$) placed directly in front of the cavity rotates the polarization of the reflected beam by 90°, which is separated from the incoming beam using a Wollaston prism. The use of a Wollaston prism instead of a polarizing beam splitter reduces potential etaloning effects and interferences between the incident and reflected beams (Sec. 4.2.3). The reflected

---

[43]PS879-C, Thorlabs.

[44]Type: Inc. AOMO 3200-1117, Crystal Technology.

[45]PLL oscillator MKU XO1PLL-696: 10 MHz to 100 MHz + frequency doubler, Mini-Circuits.

[46]P3-980-PM-FC-2, Thorlabs.

[47]WP10-B, Thorlabs

[48]EOM-320IR2, Time base

[49]PZ2-C10

[50]IO-5-1064-HP, Thorlabs.

[51]Fiber collimators 60FC-4-A8-07 Schaefter + Kirchhoff GmbH.

beam is then redirected and focused to the PDH detection photodiode.

Electronic setup

The black line in Fig. 4.23 shows the electronic connection of the stabilization servo loop, i.e. from the PDH detection PD to the PID and back to the laser head. The PDH detection photodiode[52] has a bandwidth of 125 MHz, which is fast enough to detect the phase modulated beams at the modulation frequency. The responsivity of the photodiode is 0.65 A/W at 1070 nm wavelength. The home-built circuit of the PD contains an internal low noise amplifier for an amplified output signal of 60mV/μW.

A custom Direct Digital Synthesis (DDS) device is used as an RF-frequency synthesizer to drive the EOM at the modulation frequency of $\Omega = 95.6$ MHz and as an electronic Local Oscillator (LO). It is referenced to the 10 MHz stable RF-reference from the Hydrogen Maser at PTB and amplified to provide 1.66 W (~ 32.6 dBm) of power to the EOM for an optimum sideband modulation depth of $\beta = 1.08$. The use of a relatively high modulation frequency ($\Omega = 95.6$ MHz) decreases sensitivity of the locking servo loop to the electronic noise at lower frequencies [52].

A power splitter[53] at the output of the RF-synthesizer splits the power between the RF-amplifier that drives the EOM and the signal used as LO. The LO signal is mixed[54] with the AC signal of the PDH detection photo-diode. It is recommended to use a DC-block[55] at the RF input of the mixer. The phase difference between the RF and LO (Sec. 2.4) is optimized by a proper choice of the cable length from the PD to the mixer since inserting a phase shifter can add noise to the RF signal. In fact, an electronic signal of 95.66 MHz frequency traveling a coaxial cable experiences a time delay of about 5 ns/m, which corresponds to a phase delay of about 172°/m.

The PDH error signal at the output of the mixer is sent to the PID system. We use the commercial Fast Analogue Linewidth Control FALC[56] that regulates the current of the diode laser (fast feedback path) and the piezo of the external diode laser cavity (slow feedback path) by applying negative feedback to counteract frequency deviations from cavity resonance. When the accumulated phase shift in the servo loop (e.g. from cables or electronics) is about 180°, the feedback will become positive and the servo loop will add noise to the laser. At this point the overall gain must not exceed unity to prevent oscillation of the lock. This limits the servo bandwidth. However the gain should be maximum at lower frequencies which requires the use of integrators (low-pass filters) in addition to a proportional gain (proportional part of the PID). The differential filter introduces a phase advance in the loop at high frequencies which allows maximization of the servo bandwidth [53]. The FALC used in our PDH locking scheme is adjusted as follows:

- The setpoint input of the FALC is held at 0 V (by short circuiting it) and the error signal (with the appropriate polarity) is centered around the setpoint using an offset trimpot.
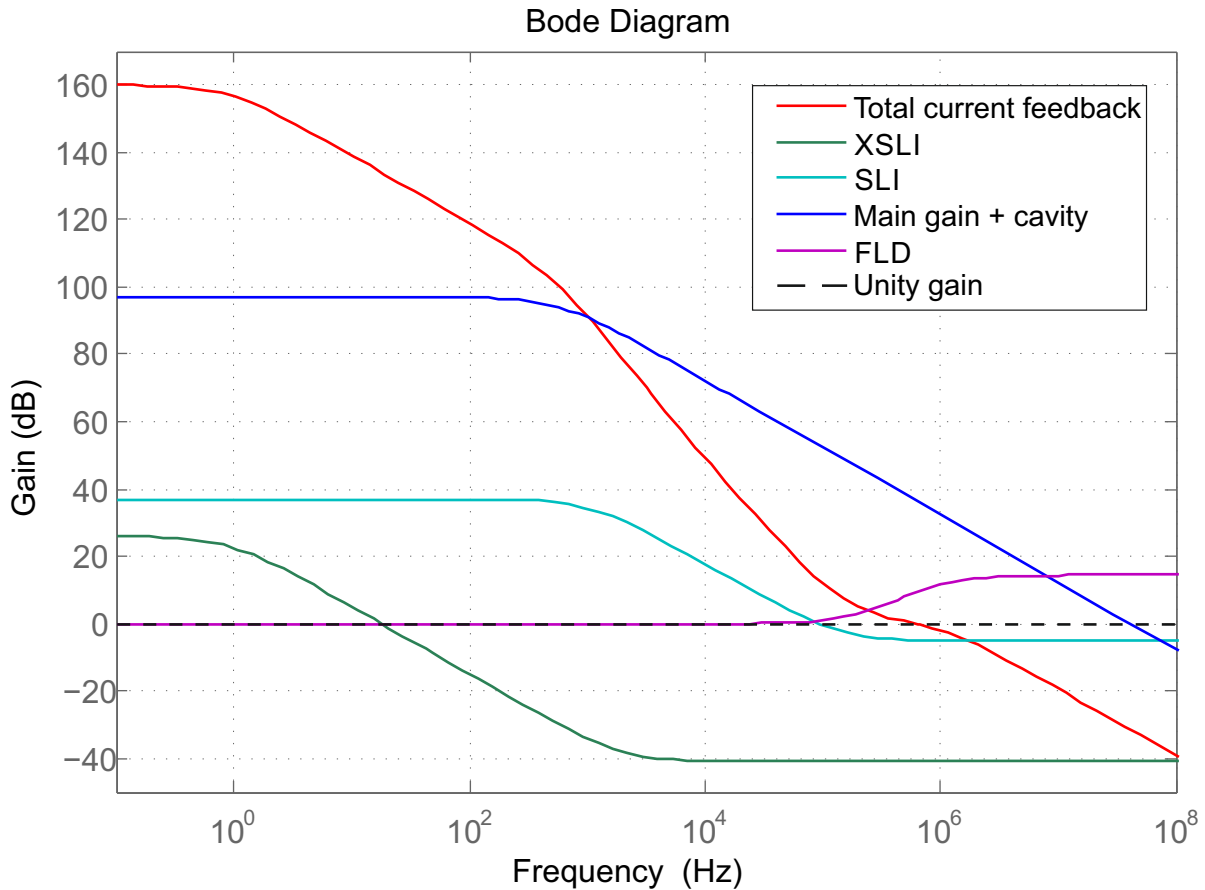
---

[52]FDGA05, active Area 0.2 mm^2, Thorlabs.
[53]ZFSC-2-1-S+, Mini-Circuits.
[54]ZX05-1-S+, Mini-Circuits.
[55]we use BLK-89+, Mini-Circuits.
[56]FALC-110, Toptica Photonics AG.

Figure 4.24: Calculated Bode diagram of the fast path PID transfer function. According to the FALC manual, our settings of three lag-lead filters of the FALC are as follows: XSLI (cut-off 1 Hz and 2000 Hz, Gain 26 dB), SLI (cut-off 1 kHz and 140kHz Gain 37 dB) and FLI (off) and FLD (cut-off 190 kHz and 1MHz, Gain 0 dB). Main gain+cavity: describes the main gain of the servo including the PID main gain and the cut-off frequency of the cavity (560 kHz), and this gain is adjusted in the simulation so that the overall transfer function of the PID crosses the unity-gain (0 dB) at the measured servo-bandwidth of 560 kHz. The second branch ULI is not presented in the plot, but it takes over increasing the gain at low-frequencies (below 1 Hz). The variation of the gain with frequency at the unity-gain frequency is kept below 20dB/decade so that the overall phase of the servo does not exceed 90°.

The input gain is set to 1 (minimum), since the RF signal is already amplified by the PD circuit. In this way we avoid extra delay in the feedback loop due to the input gain.

- The FALC has two parallel circuit branches. The first is the fast feedback branch that modulates the laser current[57]. It is composed of three lag-lead filter stages: extra slow limited integrator (XSLI), slow limited integrator (SLI), and fast limited integrator (FLI) and fast limited differentiator (FLD). The main gain of the proportional part of this branch is set via a potentiometer and adjusted for a maximum locking bandwidth and high noise suppression as will be discussed later. The second branch is the unlimited integrator (ULI) which regulates the piezo of the external laser cavity and offers high voltage amplification. It corrects for slow frequency drifts (for example temperature fluctuations), using the same error signal, by adding an unlimited gain to the PID at very low frequencies (particularly below the ESLI low corner frequency of about 1 Hz in the Toptica FALC).

- The final transfer function of the servo loop takes into account the linewidth of the cavity as the cut-off frequency of an additional low-pass filter made of the cavity coupled system (i.e. cavity, PDH detection PD, mixer), thus providing an additional integrator and gain to the PID, that we call: main gain + cavity.

- The fast and slow parts of the integrator are in parallel and use the same error signal, so any sub-millivolt offset between them is amplified by the ULI to several volts and deteriorates the quality of the lock. Extra trimpot exist to cancel this offset for the settings described above.

No filter was added after the mixer (contrary to what is shown in Fig. 2.6) since the FALC bandwidth is below the modulation frequency and has no external input offset. The input gain is set to minimum (0 dB) since the RF-signal is already amplified by the PD circuit.

In order to evaluate the total transfer function and the gain of this servo loop, the behaviour of the fast branch of the FALC (lag-lead filters), and the estimated transfer function of the integrator (main gain + cavity) are simulated and plotted in Fig. 4.24, showing the resulting servo loop transfer function and its evolution toward unity-gain (0 dB) (dashed black line). The gain level of the integrator (main grain + cavity) is adjusted in the simulation in such a way that the total current feedback crosses 0 dB at the measured servo bandwidth of 560 kHz (discussed in the following). Fig. 4.24 shows also that, with the described FALC settings, the overall noise suppression increases by up to 60 dB/decade at low frequencies due to the overlap between the different integrators (20 dB/decade for each), while it is decreased to below 20 dB/decade when it crosses the unity-gain frequency for minimum phase accumulation in the loop.

After the lock was established the linewidth of the laser is much smaller than the cavity linewidth. At this point input coupling of the laser to the cavity is optimized by observing the transmitted signal from the cavity. We obtain a coupling efficiency of 30% for an input power of 10μW.

---

[57]Modulation via ac FET-current control, accessible via BNC connection to the MOD-DC input of our diode laser
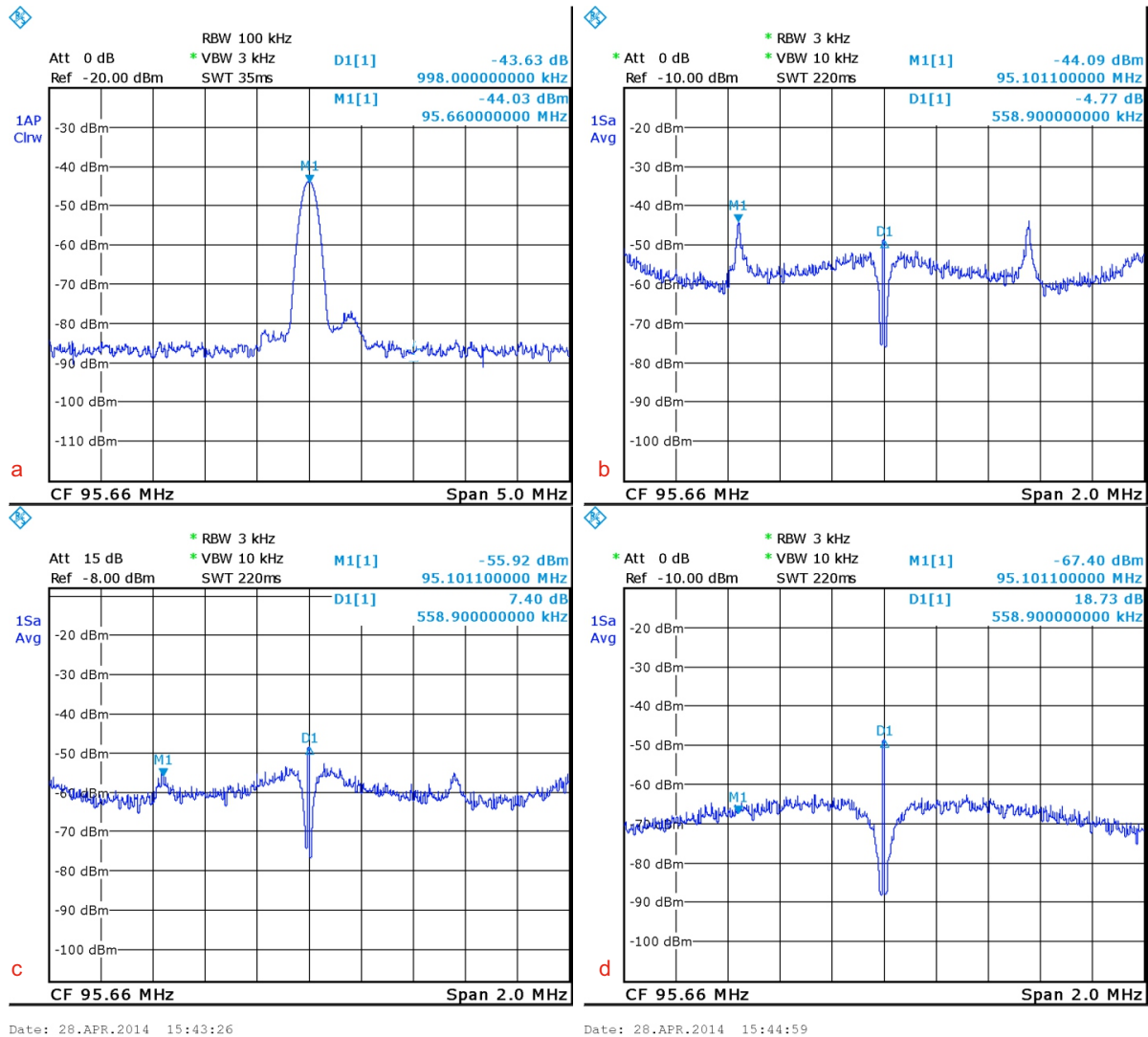
Figure 4.25: RF signal of the PDH detection photodiode taken with the spectrum analyser. (a) The photo-diode RF signal shows a peak at the modulation frequency that results from the reflected modulation sideband interference with the reflected carrier frequency (containing free running laser noise), far from the cavity resonance (out-of-loop) (see Sec.4.2.3). The three remanning graphs present the RF signal at the laser resonance with the cavity (in-loop) for various settings of the FALC main gain: (b) at maximum gain (just before going out-of-lock) showing the servo-bumps that correspond to a servo bandwidth of $\Omega - f \approx 560$ kHz, (c) at relatively lower gain compared to case (b) showing the same servo bandwidth, (c) at the optimum gain setting where the servo-bumps are minimized and the laser noise suppression around the modulation frequency is maximum. The residual peak at the modulation frequency in-loop (with the marker D_1) is the remaining quadrature of the photodiode RF-signal that has not been demodulated by the PDH mixer. This effect can be neglected since the laser stabilization relies on the quadrature of the RF-signal that has exactly a 90° phase shift with the LO.

Evaluation of the PDH lock performance

Once the laser lock to the cavity is established using the fast and slow feedback loops, the FALC settings (i.e. main gain and cut-off frequencies of the integrators) are adjusted in order to increase the servo bandwidth and gain, and thus efficiently suppress the laser noise. The servo bandwidth is determined by looking at the remaining laser noise of the RF signal (the mixer input signal from the PD) in-loop (while the laser is in lock) around the modulation frequency Ω using a spectrum analyzer[58] (see Fig. 4.23 (PDH evaluation signal)). The cavity converts laser frequency noise to phase noise of the carrier with respect to the sidebands, which interfere to give the RF signal (see Sec. 2.4). By observing the RF-signal in-loop, one can see the laser noise being suppressed symmetrically around the modulation frequency by the PID as shown in Fig. 4.25. The servo-bumps in Fig. 4.25(b,c) indicate the frequency at which the servo accumulates a total phase shift of $180°$ and begins to add noise to the laser. The measured bandwidth is about 560 kHz.
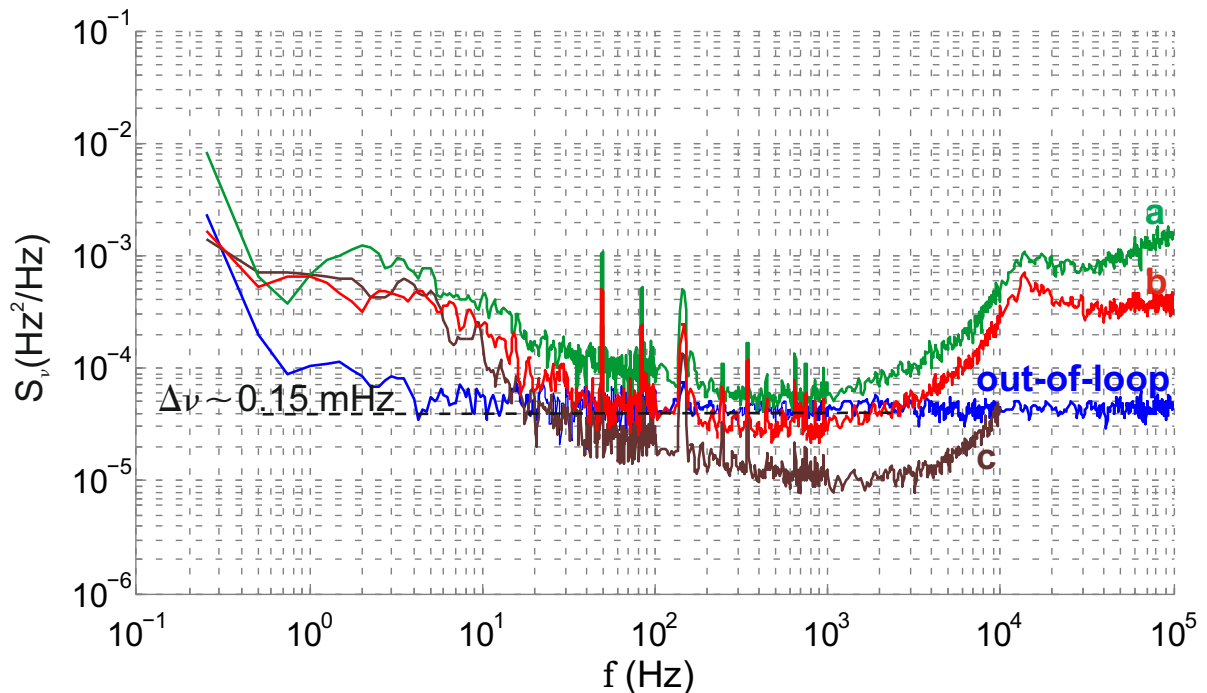
Figure 4.26: Measurement of the power spectral density of the PDH evaluation signal, as a function of the Fourier frequency f. The locked laser noise is measured with three locking configurations: (a) main gain level below the optimum, (b) main gain at the optimum level and (c) main gain above the optimum level. (out-of-loop): detection noise measured out-of-loop and far from resonance.

The gain was reduced to an optimum operation point with reduced servo-bumps as shown in Fig. 4.25(d). Since the servo loop cannot distinguish between electronic noise and laser frequency noise, a high gain might also reduce the electronic noise by adding fluctuations to

---

[58]Rohde and Schwarz spectrum analyser

the laser frequency (i.e. oscillations on the current to compensate for the electronic noise). For this reason a trade-off is made in order to have a servo loop limited by the white electronic noise of the system with a high gain at low frequencies for optimum laser noise cancellation. The optimum PDH main gain level was determined by monitoring the error signal (at the output of the mixer) in-loop with a fast Fourier transform analyser (FFT) [59] while varying the FALC main gain. The PSD of the noise measured with the FFT [in dBV/$\sqrt{\text{Hz}}$)] is converted to power units [V^2/Hz] to obtain a voltage noise PSD S_V. The PDH frequency discriminator (conversion factor in [V/Hz])) is measured as the peak-to-peak amplitude V$_{pp}$ of the error signal, visualized on an oscilloscope while scanning the unlocked laser frequency across a cavity resonance with no DC feedback to the laser. The frequency discriminator is then given by $D = \text{V}_{pp}/\Gamma$, where $\Gamma = 580.6$ Hz is the cavity linewidth (Sec.4.2.1). This slope is corrected by taking into account the low pass filtering effect of the cavity as a function of the Fourier frequency f:

$$D(f) = D/\sqrt{1 + (2f/\Gamma)^2}. \tag{4.19}$$

Finally the PSD of the frequency noise is obtained as $S_\nu(f) = S_V(f)/D(f)^2$. In our case, V$_{pp} = 110$ mV (with the FALC having an input load of 50 Ω connected to the mixer) and $D = 3.44 \times 10^{-4}$ V/Hz.

Fig. 4.26 shows the laser noise in three locking configurations: (a) main gain level below the optimum, (b) main gain at the optimum level and (c) main gain above the optimum level. A lower bound to the laser noise is the electronic detection noise that can be seen at the error signal out-of-loop and far from the cavity resonance. In case (a) the laser noise is higher than the detection noise. In case (b) the laser noise is suppressed efficiently up to the level of the detection noise. In case (c) the servo loop partially corrects for the detection noise, which disturbs the laser frequency stability.

Ideally, a PDH lock is limited by the shot noise of the photodiode due to the quantum nature of light. This shot-noise current is amplified by the servo and fed into the laser by the actuator, thus adding undesirable frequency noise. To estimate the best locking performance, we consider the power reflected onto the PDH detection photodetector (PD-1) P_r. Under ideal conditions at resonance, only the reflected power from the sidebands is left and we can write $P_r \simeq 2J_1(\beta)^2 P_0 \simeq 2P_s$. The power spectral density of the shot noise is frequency independent and can be written as [52]:

$$S_{SN} = 2h\nu(2P_s) \tag{4.20}$$

where $h\nu$ is the energy of a photon (h = Planck's constant). It is then converted into frequency noise by the PDH error signal slope (Eq. 2.34) D:

$$S_y = \frac{S_{SN}}{\text{D}^2} = \frac{\Gamma^2}{16}\frac{h\nu}{P_c}. \tag{4.21}$$

Since we cannot stabilize the laser below the detection shot noise, we can estimate the minimum linewidth of the laser with respect to the cavity in this PDH servo loop using the simple
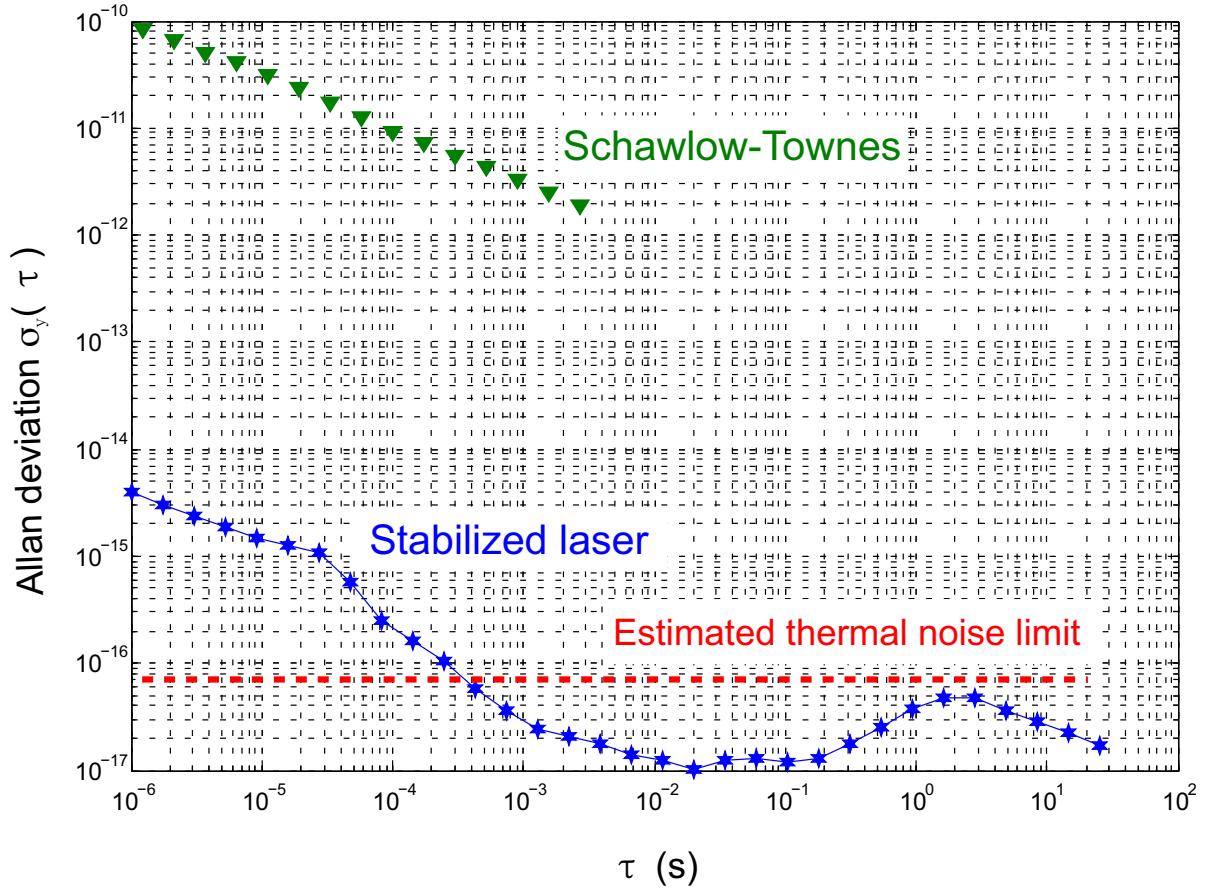
Figure 4.27: Allan deviation of the stabilized and the unstabilized laser noise (with white frequency noise (Schawlow-Townes only [103]) with respect to the thermal noise limit as a function of the averaging time τ.

relation for a white noise spectrum $\Delta \nu_{PDH} = \pi S_y$ [102]. An estimation made for a cavity with length $L = 39.5$ cm and finesse 6.5×10^5 using a laser of $\nu = 280$ THz and $P_c = 10\ \mu$W, gives $\Gamma = 580$ Hz, corresponding to a minimum frequency noise of about 4×10^{-10} Hz^2/Hz or a shot noise limited laser linewidth of $\Delta \nu_{PDH} \approx 1.2 \times 10^{-9}$ Hz.

However, the electronic noise in the PDH lock can be orders of magnitude higher due to a non-ideal mode matching to the cavity (reflection of the carrier frequency that leads to a non-zero error signal), electronic noise from the servo loop (e.g. amplifier noise, non linearity of the mixer, etc.). Nevertheless, we estimate that the white frequency noise between 10 Hz and 3 kHz of the locked laser give a linewidth of the laser with respect to the cavity on the order of $\Delta_{LC} = \pi \cdot S_\nu \approx 0.15$ mHz. Thus, the servo loop will not limit the stability of the laser with a target linewidth of around 20 mHz.

The instability of the locked laser ((b) in Fig. 4.26) is also calculated in terms of fractional frequency Allan deviation and compared to the free running laser instability in Fig. 4.27. The stabilized laser noise with respect to the cavity shows a level lower than the fundamental

---

[59]HP-35670A

thermal noise limit. The evaluation of the PDH performance shows a low noise limit, however the ultimate performance of the PDH scheme relies on the stability of the detected error signal and specifically the RF signal in the PDH detection.

A major limit to the laser stabilization is the residual amplitude modulation (RAM), which is discussed in the following section.

4.2.3 Residual Amplitude Modulation (RAM)

In the PDH stabilization scheme, the error signal should be equal to zero when the laser is on resonance with the cavity, the carrier frequency is (partially) transmitted, and the sidebands are totally reflected and cancel each other. Any perturbation of this symmetry (i.e. sidebands with unequal magnitude, phase asymmetry around the carrier, or both), especially when this perturbation is not constant in time, disturbs the error signal locking point (See Sec. 2.4) by adding a fluctuating DC-offset and thus deteriorating the laser stabilization procedure. A major distortion to the modulation sidebands symmetry comes from residual amplitude modulation (RAM). In fact, the EOM and the optical setup between the EOM and the cavity form a very low finesse resonator that acts as a frequency to amplitude converter. This will create an amplitude asymmetry between the red and the blue sideband of the frequency modulated laser, which appears as an additional oscillation of the intensity on the PDH detection photodiode at the modulation frequency, which results in a DC-offset of the error signal.

The RAM-induced fractional frequency instability $\sigma_y(\tau)$ can be written as [104]:

$$\sigma_y(\tau) = \sigma_{RAM}(\tau)\frac{\Gamma}{\nu}. \tag{4.22}$$

For our cavity measured linewidth of $\Gamma = 580.6$ Hz at $\nu \approx 280$ THz laser frequency, the Allan deviation of the RAM fluctuations σ_{RAM} should be below 10^{-5} in order to operate the cavity at the thermal noise limit of $\sigma_y \approx 7 \times 10^{-17}$.

A number of techniques have been developed to overcome the RAM by an active cancellation of this effect [31, 105–108]. A recent publication [104] shows a possible reduction of the RAM induced by a waveguide-based EOM to $\sigma_{RAM} \approx 1 \times 10^{-5}$ by implementing an active servo with a DC electric field and temperature stabilization of the EOM.

The work presented here does not contain an active cancellation of RAM; instead, this effect is evaluated in order to understand its limitation on the laser stability performance. We start by presenting our passive method for minimizing the RAM effect. Then, an evaluation in terms of Allan deviation with respect to the estimated thermal noise limit of laser stability is given.

Minimization of the RAM effect

The PDH optical and electronic settings are shown in Fig. 4.23. Possible RAM sources and corresponding methods used for minimizing their effect of the laser stabilization (described in Sec. 4.2.2) are given in the following:

- The internal backscattering between the EOM facets. To minimize this effect, we use a Brewster-cut EOM that has a small angle between the facets of the KTP crystal, which in turn has a small piezo-electric effect[60].

- Mismatch between the light polarization and the modulation axis of the EOM. In this case the polarization is rotated with the modulation frequency of the EOM, and the polarizing beam splitter placed after the EOM (to redirect the reflected beam from the cavity) produces an amplitude modulated beam. This effect can be reduced by using a Glan-Laser Polarizer in front of the EOM, and a precise alignment of the EOM crystal, for a high polarization purity along the principal modulation axis.

- Etalon effect between the cavity mirror and the end facet of the EOM. An additional optical isolator is used after the EOM to prevent such parasitic cavity. In addition, all optics between the EOM and the cavity are AR coated for our wavelength and slightly tilted to prevent etalons. The cavity mirrors have a small angle (0.5-2°) between their facets and the beam samplers used as viewports for the heat shields and the vacuum chamber windows are AR coated on both sides and also have a 0.5° angle between facets to avoid plane-parallel etalon effects (Vacuum chamber design can be found in Appendix D).

The passive solutions presented above to minimize the RAM effect can not prevent temperature fluctuations in the experimental environment from disturbing the stability of the polarization alignment with the principal axis of the EOM. Other defects in the EOM such as the non-homogeneity of the modulation-RF field in the EOM crystal due to an imperfection in the crystal itself also causes RAM effects. However, with a brewster-cut EOM, the major contribution to RAM comes usually from the etalon effect between the different optical components that are between the EOM and the coupling cavity mirror.

Another effect that can disturb the error signal detection is the cross talk between the RF source for the frequency modulation of the EOM and the PDH detection photodiode (PD). This can generate DC-offset fluctuation after the mixer. In our case, shielding the EOM, the DDS box and the PD minimizes the RF pick-up noise to below -80 dB and obtain a final RF signal-to-noise ratio of more than 40 dB.

Evaluation of the RAM effect

The evaluation of the RAM effect is performed with the laser turned off-resonance with the cavity. It is important to note that an off-resonance (laser out of lock) estimation of the RAM will give a lower bound on this effect, which might be even higher when the laser is in lock. In fact, spurious etalons can disturb, due to the line pulling effect, the resonance frequency of the laser with the reference cavity. On the other hand, an in-loop evaluation of RAM is not conclusive since more noise sources from the servo-loop electronics are added to the RAM noise spectrum, such as electronic noise and fluctuations of the differences between ground levels of the different electronic components.

---

[60]Crystals used in the EOMs are also piezo-electric and induce an avoidable amplitude modulation particularly when they are driven at frequencies close to acoustic resonances of the crystal.

In our case, an evaluation of the RAM effect is made off-resonance at the DC output of the mixer (see Fig. 4.23) in the PDH setup. This signal is equivalent to the error signal DC level. When the RAM effect is high, one can see this non-zero DC-signal far from the cavity resonance frequency. In our case, a precise voltmeter[61] is used to evaluate the behaviour of the error signal DC-level. A time series of the voltage is then converted into a fractional frequency Allan deviation using the same conversion factor from Eq. 4.19. Fig. 4.28 shows the results for the off-resonance RAM measurements.
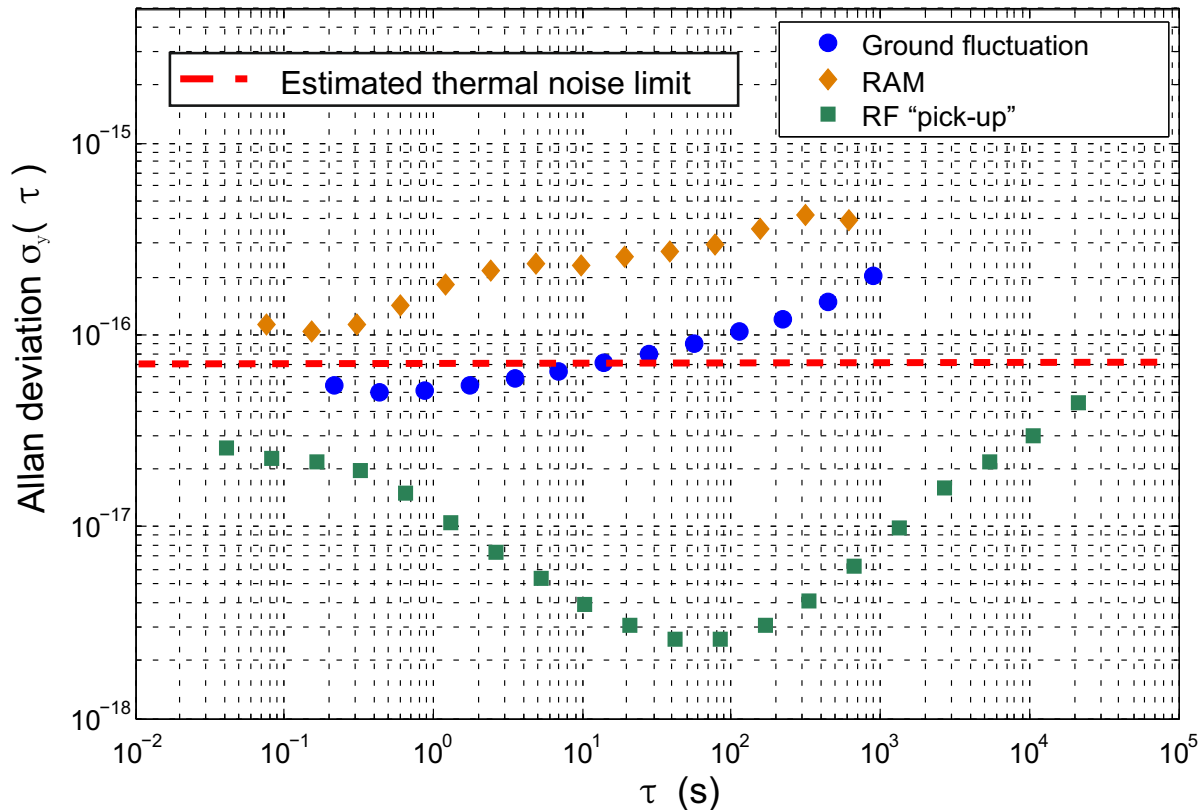
Figure 4.28: Fractional frequency instability due to RAM effect, RF pick-up noise on the PDH detection PD, and ground loop fluctuations as a function of the averaging time τ, compared with the estimated thermal noise limit of the frequency stability (dashed red line).

From Fig. 4.28 and Eq. 4.22 we can conclude that the RAM effect in our setting is only reduced to $\sigma_{RAM} \approx 2 \times 10^{-4}$ and thus induces a fractional frequency stability of up to 4×10^{-16} for times shorter than 200 s. In order to evaluate the noise sources contributing to such high fractional frequency instability, a second evaluation is made while the laser beam going to the PDH detection PD is blocked in order to distinguish the effect of the RF pick-up noise on the PD from the RAM effect (the modulated laser light). An additional measurement consists of evaluating the ground level fluctuations between the ground of the power supply of the FALC and the ground level at the mixer (from PD supply and the DDS box of the RF local oscillator), since a variation over time of the ground level between the FALC and the mixer

---

[61]Precise digital multimeter 34410A, Agilent Technology.

induces an additional oscillation at the DC-level of the error signal and influences the laser lock performance.

The RF pick-up contribution to the fractional frequency stability is below 10^{-17} between 1 and 200 s, while the ground fluctuation induces a fractional frequency stability above 5×10^{-17} for the same time scale. For both evaluated cases, the RAM effect (measurement done with the laser going to the PD) is dominant and limits the performance of the system.

Several steps could be done in order to improve RAM and the electronic noise disturbing the DC level of the error signal, such as:

- Active cancellation of the RAM effect

- Ground-loop cancellation

Other groups where able to stabilize RAM to below 10^{-5} [104]. Thus following these steps we would be abel to reduce the RAM induced fractional frequency instability below the level of the thermal noise limit.

4.2.4 Laser intensity stabilization

Intensity stabilization is crucial for improving the performance of ultra-stable optical cavities. When the laser is resonant with the cavity, the power circulating inside this optical resonator is resonantly enhanced due to the high mirror reflectivity. The power inside the cavity P_I can be written as a linear function of the coupled power P_0 as:

$$P_I \approx \frac{\mathscr{F}}{\pi} \times P_0 \tag{4.23}$$

where $\mathscr{F}$ is the cavity finesse. In our case, the measured finesse is about $\mathscr{F} = 650,000$ (see Sec. 4.2.1), which means that for a coupled input power of 10 μW, the circulating power inside the cavity is about 2.06 W. The laser beam inside the cavity applies a local heating on the mirror that has a power density of 628 W/cm^2 for our case, where the beam radius on the mirrors is on average 450 μm. The intensity absorbed by the coating creates a spatially varying temperature distribution and the thermal expansion deforms the coating and the substrate, particulary with the FS substrate that has a relatively high coefficient of thermal expansion (see Sec. 4.1.1). This effect results in cavity length fluctuations that are converted into frequency fluctuations correlated with to the laser power fluctuations. Depending on the cavity finesse, the type of the mirrors, cavity length etc., the sensitivity to intensity fluctuations χ_c ([Hz/W]) is specific to each cavity. It relates the Allan deviation of the cavity transmitted intensity fluctuations $\sigma_I(\tau)$ [W] at the laser frequency ν_0 to the fractional frequency fluctuation $\sigma_y(\tau)$ by:

$$\sigma_y(\tau) = \frac{\chi_c}{\nu_0} \sigma_I(\tau). \tag{4.24}$$

In this section, we present two measurements. The first one consists of stabilizing the laser intensity and identifying the cavity frequency sensitivity to intensity fluctuations χ_c. The second one consists of evaluating the performance of the implemented intensity stabilization scheme. Results in terms of Allan deviation will be given and compared to the thermal noise limit.

Cavity sensitivity to intensity fluctuation

An active cancelation of the laser intensity fluctuation is performed using the transmitted beam from the cavity. A sketch of the intensity stabilization system is presented in Fig. 4.29.

The transmitted laser beam from the cavity is detected using the photodiode[62] PD-1, with responsivity of $R_\lambda = 0.1$ A/W at 1070 nm wavelength, showing an amplified output signal of 79 mV/μW (measured voltage with respect to the transmitted beam power sent to this photodiode) in the transmitted laser power. The resulting DC-voltage is compared with a stable voltage source of measured voltage stability $\sigma_{v,ref}=10^{-6}$ V (See Appendix E). An error signal is generated and sent to a PI-servo (See Appendix E) to adjust the power level at the AOM[63]. The PI contains one integrator and two operational amplifiers to minimize the internal electronic thermal noise that influences the stability of the reference voltage source[64]. The measured time constant of the intensity stabilization servo-loop is 65(5) μs. Details of the electronic components are presented in Appendix E.

Detecting the transmitted laser beam (from the cavity) for the intensity stabilization is recommended since the photodiode after the cavity is insensitive to non-resonant stray light or polarization fluctuations that would occur when using a beam sampler to extract a part of the incident beam. Although this limits the intensity stabilization bandwidth to frequencies below the linewidth of the cavity, this still includes the averaging time of interest.

Once the laser is locked to the cavity, the intensity is stabilized using all of the cavity transmitted intensity on PD-1. In order to evaluate the frequency shift due to the intensity variation and thus calibrate χ_c, we manually change the set voltage of the PI and observe the frequency shift due to the changing input intensity. The temporal response behaviour of the frequency shift is not evaluated since the set voltage is shifted manually.

Fig. 4.30 shows the frequency shift with the level of the transmitted intensity as a function of the measurement time (linear drift is removed from the data, see Chap. 5). The shift shows that $\chi_c = 132(20)$ Hz/μW. According to Eq. 4.24, the intensity should be stable to within $\sigma_I = 0.14$ nW in order to reach the thermal noise limit.

Intensity stabilization results

For the final intensity stabilization setup, the more sensitive photodiode PD-2[65] with a responsivity of 0.7 A/W at 1070 nm wavelength and amplified output signal of 0.6 V/μW is used in-loop. The first (less sensitive) photodiode PD-1 is now used for an out-of-loop evaluation of the intensity stabilization performance. The transmitted beam is split equally by a polarizing beam splitter (PBS) into two transmitted beams for the two photodiodes. The DC-voltage output of PD-1 is measured over time[66] and the instability in terms of Allan deviation is converted first into the Allan deviation of the intensity fluctuation using PD-1 sensitivity of (79 mV/μW), and then converted into a fractional frequency instability using the measured sensitivity factor

---

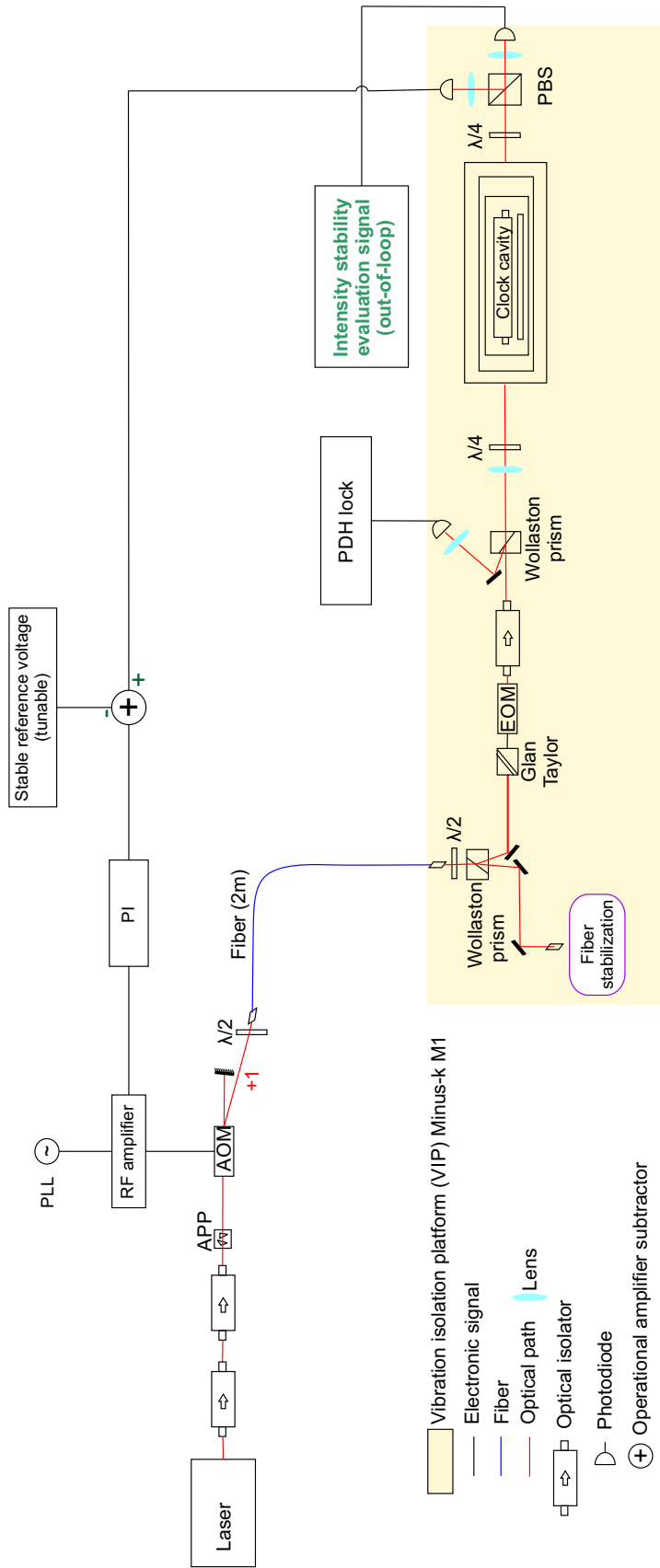[62]S5971, active area 1.2 mm^2, Hamamatsu

[63]custom RF-amplifier (PTB design) with DC modulation input controlling the RF output power level

[64]Pin Programmable, precision voltage reference AD584-K. Maximum trimmed temperature coefficient of 15 ppm/$^\circ$C.

[65]DFGA10, active area= 1.1mm^2

[66]Precise digital multimeter 34410A, Agilent Technology.

Figure 4.29: Sketch of the optical setup for the intensity stabilization in transmission. The transmitted beam from the cavity is separated via a quarter wave plate ($\lambda/2$) and a polarizing beam splitter (PBS) then focussed on two different photodiodes:: the first is used in the servo-loop of the intensity stabilization and the second for the out-of-loop evaluation of the intensity stability. The photodiode signal in-loop is compared to the stable reference voltage source via an operational amplifier subtractor, then the error signal is sent to the Proportional integral feedback circuit (PI) (electronic parts are described in Appendix E). PLL: Phase-locked loop crystal oscillator used to generate 100 MHz from the reference signal at 10 MHz (from the Hydrogen maser). The PDH stabilization step is described in Sec. 4.2.2, the fiber link stabilization in Sec. 5.1.

χ_c and Eq. 4.24. The results for the stabilized laser (stabilization on, measured with PD-1 out-of-loop) plotted in squares in Fig. 4.31, shows that the Allan deviation of the fractional frequency instability due to the intensity fluctuation has a flicker floor noise at the level of 4×10^{-16}.
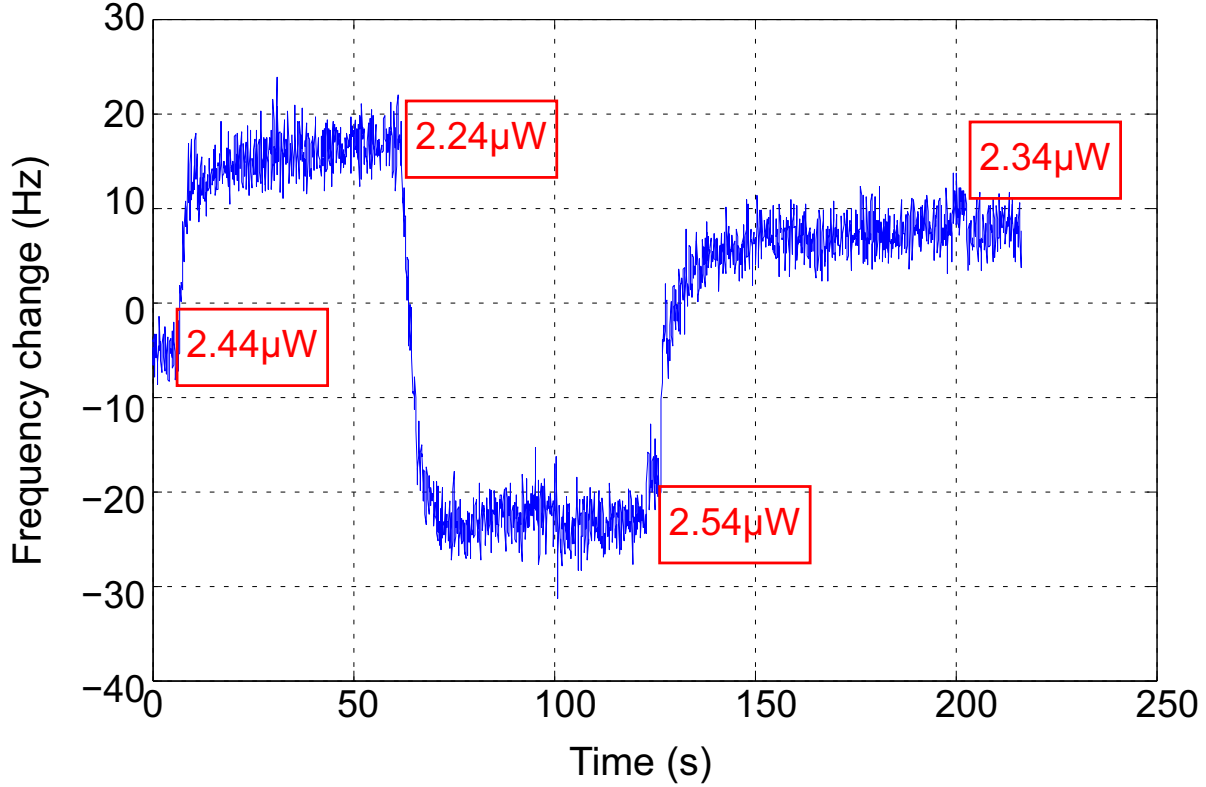
Figure 4.30: Variation of the laser frequency for different values of transmitted intensities (the power was measured with PD-2 of sensitivity 79 mV/μW). A fit to the data results in a sensitivity of the stabilized laser frequency of $\chi_c = 132(20)$ Hz/μW to the transmitted intensity.

Several estimations done in order to evaluate the limiting factors in the intensity stabilization schemes are shown in the same plot.

The sensitivity of PD-1 is limited in principle by electronic noises, Johnson-Nyquist noise and shot-noise due to the finite number of photons in the light on the PD. The Johnson-Nyquist noise and shot-noise both have a $1/\sqrt{\tau}$ behaviour in terms of Allan deviation (See Tab. 2.1). Nevertheless, an estimate of the Allan deviation of the PD-1 shot-noise is done in order to compare it with the measured results. The mean power of the laser on PD-1 is measured to be $P_{t2} = 1.3\ \mu$W and the quantum efficiency of PD-1 is $\eta = R_\lambda h\nu/e \approx 11\%$, where $R_\lambda = 0.1$ A/W is the responsivity, e is the elementary charge and h is the Planck constant. The shot noise can then be evaluated from the photocurrent with:

$$\sigma_{SN}(\tau) = \sqrt{\frac{h\nu_0}{\eta P_{t2}}}\sqrt{\frac{1}{\tau}} \approx 1.1 \times 10^{-6}\sqrt{\tau} \tag{4.25}$$

where ν_0 is the laser frequency in resonance with the cavity (280 THz). This corresponds also to the Allan deviation of the relative power fluctuation, and we can calculate a relative frequency fluctuation using the sensitivity factor χ_c:

$$\sigma_y(\tau) = \frac{P_{t2}}{\nu_0}\chi_c\sigma_{SN}(\tau) \approx 7 \times 10^{-19}\sqrt{\tau}. \tag{4.26}$$

PD-2 has a shot noise limit of about $3\times10^{-19}/\sqrt{\tau}$. This means the photodiode shot-noise does not limit the current performance of the intensity stabilization. However, the electronic noise has a behaviour of $1/f$ (See Tab. 2.1), which means it contributes a flicker floor to the Allan deviation. This is evaluated by blocking the laser beam on PD-1. Fig. 4.31 (triangles) shows that this is also not responsible for the current performance of the fractional frequency fluctuation from the intensity instability (squares). The dark noise (with blocked laser) of the sensitive photodiode PD-2 is also evaluated for the limitation on the intensity stability, but it shows similar results as for PD-1.

This means that either the detected light on the photodiode does in fact fluctuate in intensity with $\sigma_I = 0.86$ nW, a factor of 6 higher than what is required for thermal noise limited clock cavity performance.

The polarization axis of the quarter-wave plate ($\lambda/4$) placed in front of the PBS (See Fig. 4.29) to split the cavity transmitted beam is sensitive to room temperature variation and cold air flows (both are present in our lab). A rotation of the polarized light occurs and changes the power ratio at the level of the photodiodes (in-loop and out-of-loop). This adds intensity noise to the system and thus induces higher fractional frequency instability. In order to evaluate the effect of temperature variation on the polarized light, we heat[67] for a short time the $\lambda/4$ plate while the intensity is stabilized. The results of the out-of-loop evaluation of this effect is plotted in Fig. 4.31 (in stars). The measurement proves that the temperature changes in the lab can induce an additional intensity fluctuations in the system.

A flicker fractional frequency instability of 4×10^{-16} due to the intensity instability is not sufficiently low to achieve the thermal noise limit (dashed red line in Fig. 4.31). This might be due to thermal effects on the photodiode amplifier that increase the internal noise in both (in-loop and out-of-loop) photodiodes. In addition, the quarter wave plate placed in front of the polarizing beam splitter to split the transmitted beam into the in-loop and out-of-loop photodiodes is not an optimum choice since the sensitivity of the $\lambda/4$ plate to temperature may induce polarization rotation on the PBS. Replacing the system ($\lambda/4$ + PBS) by a non-polarizing (50/50) beam splitter and the use of photodiodes with identical sensitivity (type PD-2) for the intensity stabilization and the out-of-loop characterization, can reduce the frequency fractional instability due to the intensity instability. Covering of the optical system and isolating it from air flows and room temperature variations can further reduce the intensity instability.

---

[67]Using a heat gun at lowest temperature setting in order not to damage the wave plate. Heating for short time before evaluating the intensity stability.
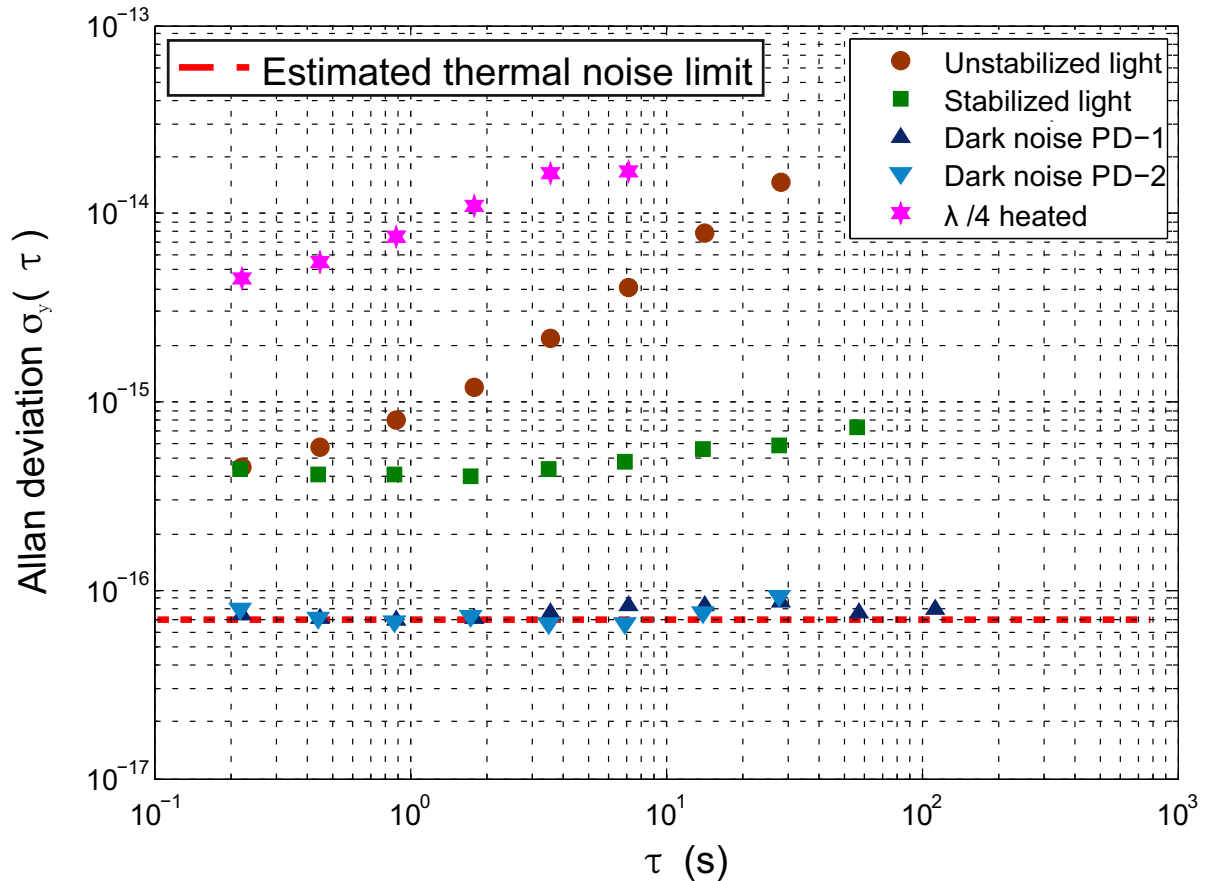
Figure 4.31: Allan deviation of the intensity instability contribution to the fractional frequency instability $\sigma_y(\tau)$ as a function of the the averaging time. The power of the transmitted laser from the cavity is split into two beams equal in intensity to within 1%, using a quarter-wave plate ($\lambda/4$) in front of a PBS as shown in Fig 4.29, for the in-loop (PD-2) and the out-of-loop (PD-1) photodiodes (1.3 μW each). (squares): Out-of-loop the evaluation of $\sigma_y(\tau)$ using PD-2 (similar results for PD-1 used out-of-loop) with the intensity stabilization on. (stars): Out-of loop measurement (using PD-2) while heating the $\lambda/4$ which induces a fluctuation on the power ratio at the level of the PBS. (circles): $\sigma_y(\tau)$ for non-stabilized transmitted laser power. (triangles): The measurement of the electronic (dark) noise contribution to $\sigma_y(\tau)$ from PD-2 (triangle up) and PD-1 (triangle down) with all incoming laser and room light blocked.

Chapter 5

Performance of the Clock cavity

In the previous chapter, we have presented the experimental evaluation of individual contributions from the environmental perturbations and the stabilization scheme to the fractional frequency instability of the 1070 nm laser locked to the 39.5 cm cavity. In order to measure the achieved performance of the cavity, the stabilized laser is transferred via a 350 m optical fiber and compared with two different ultra-stable lasers at PTB using a frequency comb. A general overview of the laser stabilization optical setup is presented in Appendix C.

The results are presented in this chapter. In the first section, we describe the fiber noise cancellation technique used to stabilize the 300 m fiber link. In the second section we explain the technique of using a frequency comb to compare ultra-stable lasers of different wavelengths. The last section of this chapter contains the cavity performance results as well as a discussion about possible ways of improving it.

5.1   Fiber link stabilization

The 1070 nm stabilized laser is transferred from the cavity laboratory located in the sub-basement of the building (-1st floor), via a 100 m long polarization maintaining (PM) fiber[1], to the ion clock experimental laboratory (5th floor) for interrogating the Al^+ ion. This link was used when we characterize the thermal properties of the cavity (see Sec. 4.1.1). By connecting the end of this fiber to a second 250 m long PM fiber[1], the laser is sent to a different building at PTB (Paschen Bau) where two additional stable laser systems are used for a comparison in terms of stability (see 5.2). Thus, the stabilized laser must travel a total of 350 m of fiber.

Fiber links are a useful tool for frequency standards that allow ultra-stable laser transfer [109, 110] for comparison and manipulation. However, they are sensitive to environmental perturbations (i.g. temperature fluctuation, acoustic pressure variation, etc.) that add phase noise to the transmitted laser and thus cause degradation of the laser frequency stability [111]. For this reason, fiber phase noise compensation is required.

In this section we first review the major noise sources of an optical fiber link. In the second part, the 350 m fiber noise compensation scheme and its limits are presented. An in-loop

---

[1] Commercial polarization maintaining fiber with cut-off wavelength 840 nm-1020 nm, FC-APC, type Bow-Tie HB1000, Company: Fibercore.

evaluation of the fiber noise compensation in terms of fractional frequency Allan deviation in the third and laser part is given.

Fiber induced frequency noise

A laser sent through the fiber arrives after a time delay of $\tau_f = n_f L_f/c$ where L_f is the geometrical length of the fiber (350 m), $n_f \approx 1.5$ is the refractive index of the glass core of the fiber and c is the speed of light. The modulation of the fiber optical path length ($n_f \cdot L_f$) due to a fluctuation of the refractive index of the glass core results in phase noise that is accumulated by a laser while traveling in the fiber and added to the original frequency noise of the laser, thus broadening its line. The measured instability at the end of the fiber thus becomes higher.

The fluctuations of the refractive index $n_f(T,P)$ inside the fiber are the result of environmental perturbation effects such as unstable temperature (T) and mechanical and acoustic vibrations that act as a pressure P applied to the fiber. The propagating laser phase changes inside the fiber as a function of time t, inducing an instantaneous frequency change of $\Delta\nu_{fib}$ that can be written as [112]:

$$\Delta\nu_{fib} = \frac{d\phi_{fib}}{dt} = \frac{2\pi}{\lambda}\frac{d\left[n_f(T,P)\cdot L_f(T,P)\right]}{dt}. \tag{5.1}$$

The refractive index variations as a function of the temperature and pressure ($d(n_f(T,P))/dt$) have a greater effect on optical path length inside the fiber than the thermal and mechanical expansion of the fiber glass core ($d(L_f(T,P))/dt$) [113]. These effects can be interpreted as Doppler frequency shift of the laser inside the fiber which can be approximated as:

$$\Delta\nu_{fib} \approx \frac{2\pi L_f}{\lambda}\left(\frac{d(n_f)}{dT}\frac{dT}{dt} + \frac{d(n_f)}{dP}\frac{dP}{dt}\right) \tag{5.2}$$

This Doppler shift increases with the length of the fiber L_f. However, it is possible to compensate for it using an acousto-optic modulator (AOM) [111] as we will show.

Fiber noise compensation

For compensating the frequency fluctuations in the fiber link, a heterodyne interferometric technique is implemented [111]. It consists of comparing the laser frequency before and after the fiber link and correcting for the frequency shift between them. Since the two ends of the fiber are situated in two different laboratories, a mirror at the output of the fiber is used to reflect the laser back through the fiber to form the interferometer. This technique assumes that the noise accumulated by the laser in its trip through the fiber is the same as that accumulated on the return trip. A total delay of $2\tau_f = 2n_f L_f/c$ is accumulated. This technique correctly cancels the phase noise induced by the fiber as long as the coherence time of the laser is much longer than the time delay in the fiber, so that the light phase at both ends of the fiber is correlated[2]. For our case, we aim to achieve a laser linewidth well below 1 Hz, corresponding to a coherence length of 6×10^4 km, orders of magnitude longer than the fiber length.

---

[2]If the coherence time of the laser is shorter than the delay time of the fiber, the laser phase at the two ends will be uncorrelated.
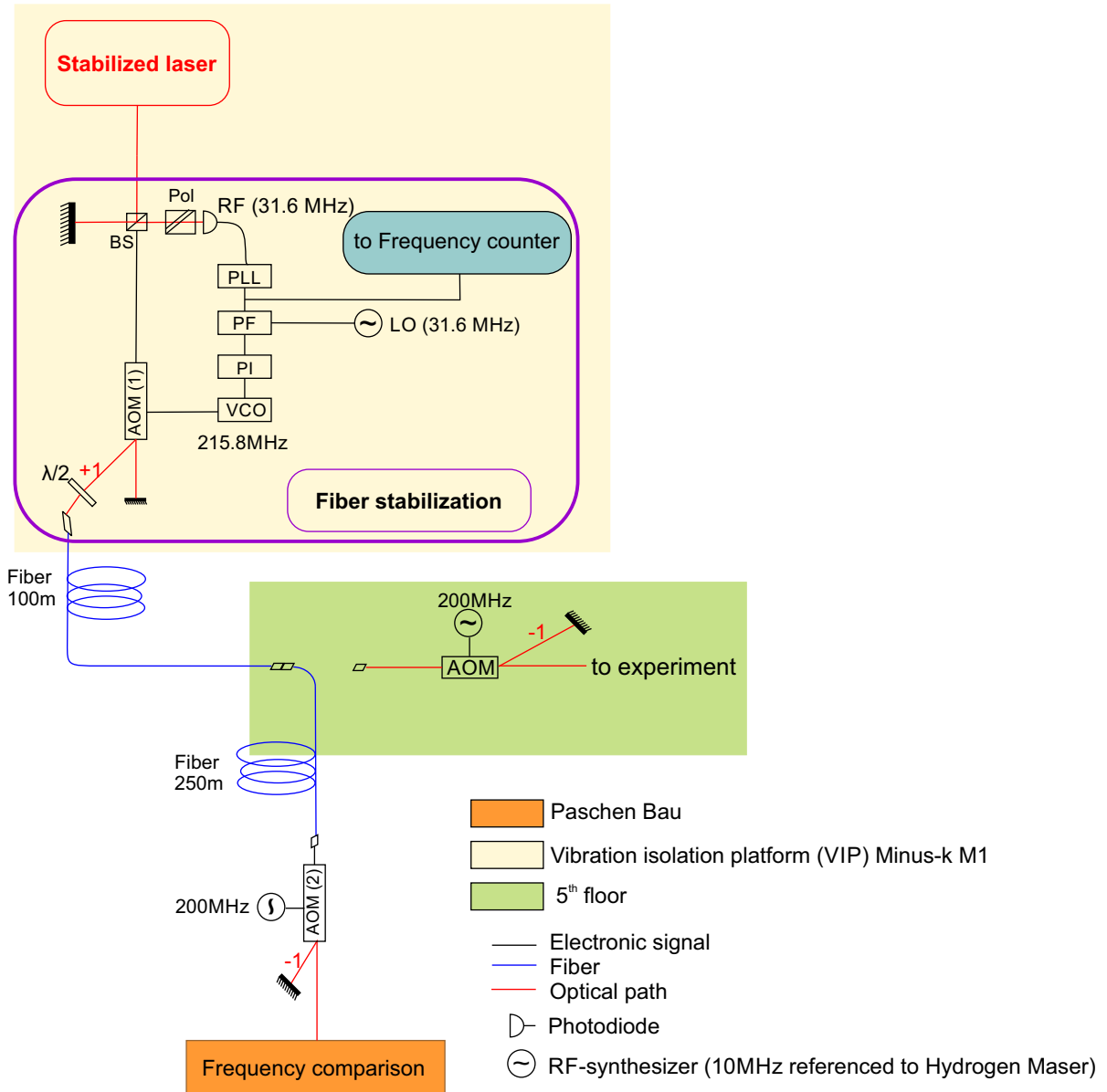
Figure 5.1: Optical setup for fiber induced frequency noise cancellation using a heterodyne interferometer. BS: beam sampler (90/10) for sending about 10% of the light to the reference arm of the interferometer and 90% of the rest of the power to the fiber. PLL: phase locked loop used as a tracking oscillator of the RF beat note frequency with a bandwidth of 5 MHz, PFC: phase-frequency comparator, PI: proportional integral filter, VCO: voltage controlled oscillator (Marconi with DC-modulation input as in Sec. 4.1.2) and Pol: Glan Taylor polarizer.

A schematic of the optical setup used for the fiber noise cancellation is presented in Fig. 5.1. The stabilized laser at frequency ν_0 is split using a beam sampler (BS)[3] into two paths. The short arm of the interferometer (10% of the power) located before AOM (1) is used as the reference arm (assuming no phase noise in the arm). The long arm contains the AOM (1), the fiber and a second AOM (2) after the fiber. The light in the short path is reflected by a mirror, crosses the BS a second time and is then directed towards a photodiode. The laser in the long path is frequency shifted using a first AOM[4] (1) by $\nu_{AOM1} = +215.8$ MHz where the frequency is provided by a VCO[5] referenced to the 10 MHz signal from a the Hydrogen maser. The polarization of the diffracted beam is rotated using a $\lambda/2$ wave-plate to meet the polarization axis of the first 100 m long PM fiber, to which it is coupled with 70% coupling efficiency. On the 5th floor (location of the ion experiment), the fiber is connected to the second fiber of 250 m length, using a mating sleeve[6] to send the laser to the frequency comparison in a second lab (Paschen bau, PTB $\approx$200 m away from our building). During this trip through the fiber, the laser accumulates a frequency shift of $\Delta\nu_{fib}$.

At the end of the second fiber, the laser is again frequency shifted (negative shift) using the second AOM (2) by $\nu_{AOM2} = -200$ MHz. The total frequency shift of the diffracted beam is then:

$$215.8 \text{ MHz} + \Delta\nu_{fib} - 200 \text{ MHz} = \Delta\nu_{fib} + 15.8 \text{ MHz}. \tag{5.3}$$

The diffracted beam from AOM (2) is then reflected back and coupled to the fiber with the same incoming polarization[7], using a stable mirror, for a precise fiber noise cancelling. The returning beam crosses the AOM (2) for the second time and accumulates a second negative frequency shift $\nu_{AOM2} = -200$ MHz. Traveling the fiber, the laser accumulates a second frequency shift $\Delta\nu_{fib}$ and then crosses AOM (1) a second time and adds a laser frequency shift of $\nu_{AOM1} = +215.8$ MHz. The laser frequency is in total shifted by:

$$\Delta\nu_{fib} + 15.8 \text{ MHz} - 200 \text{ MHz} + \Delta\nu_{fib} + 215.8 \text{ MHz} = 31.6 \text{ MHz} + 2 \times \Delta\nu_{fib}. \tag{5.4}$$

The superposition of the short path beam and the long path beam will result in a beat-note at the photodiode at 31.6 MHz$+2 \times \Delta\nu_{fib}$. The amplitude of the beat is optimized using a polarizer. The photodiode[8] we use for detection is AC-coupled with 46 dB RF-signal amplification. The reason of using a frequency of 31.6 MHz is to minimize the photodiode RF-pick-up of frequency multiples of 10 MHz present in our laboratory.

The RF-signal from the photodiode is amplified and spectrally purified by means of a phase locked loop oscillator that also optimizes the signal to noise ratio of the signal (to about 40 db). A custom Direct Digital Synthesis (DDS) device generates a stable 31.6 MHz signal

---

[3]Beam sampler BSF10-C, Thorlabs.

[4]Type: Inc. AOMO 3200-1117, Crystal Technology.

[5]Marconi 2023B Signal Generator. We use the DC modulation input to correct the RF frequency output toward the AOM.

[6]ADAFC3, Thorlabs.

[7]The PM fiber has two orthogonal axes: the slow one with high refraction index and the fast one with a low refraction index. The fiber noise cancellation should be applied to a laser traveling back and forth on the same axes, otherwise the frequency correction can be compromised by a differential effect of the two polarization speed.

[8]FDGA10, active area 0.8 mm^2, Thorlabs, integrated into a home-built amplifier circuit.

(from the 10 MHz RF-signal of the Hydrogen maser), and is used as a stable Local Oscillator (LO). A custom made digital phase-frequency comparator compares the LO signal to the beat RF-signal and generates an error signal. The PI (proportional integral filter) is used to convert the error signal into a DC voltage that is then fed-back to the DC modulation input of the VCO. The signal in Fig. 5.2 shows the locked heterodyne beat note in-loop, that results from the interference of the reference laser beam (short path) and the reflected laser through the fiber (long path). The interference pattern results from the fact that the laser is coherent after a round trip in the fiber and interferes with itself on the photodiode.
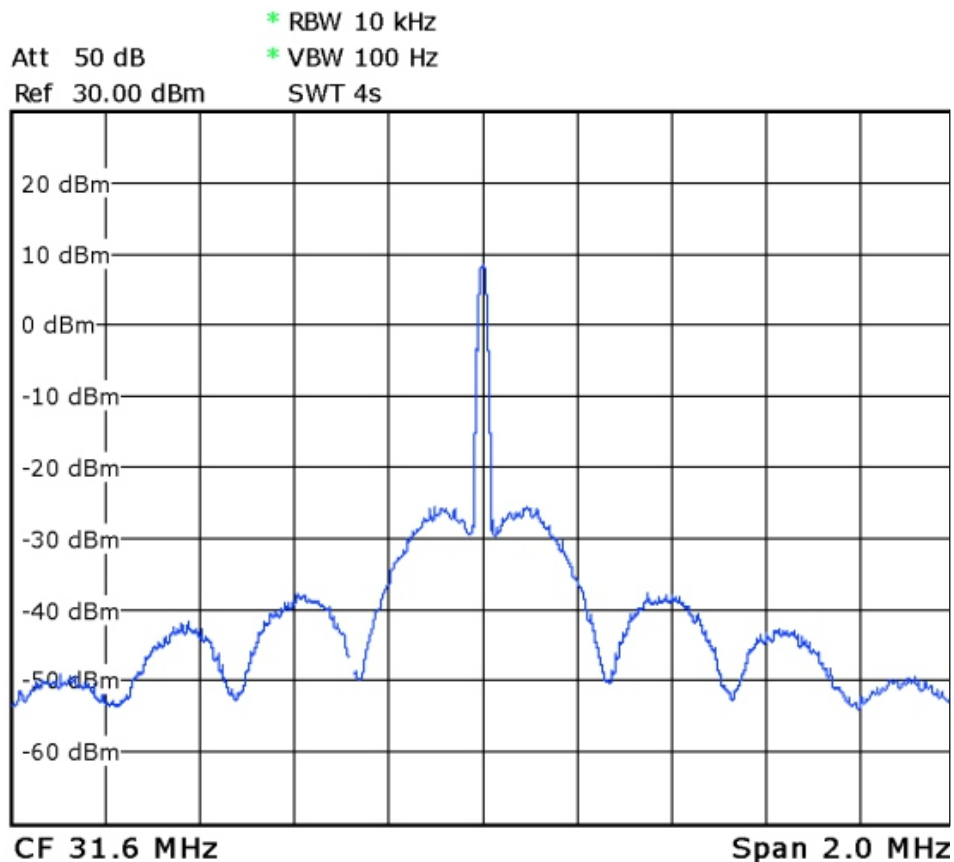
Figure 5.2: Power spectrum of the in-loop RF beat-signal observed using a spectrum analyser. The interference pattern results from the finite ($\approx 3.5 \ \mu$s) round trip delay in the fiber. The bandwidth of the spectrum analyser (10 kHz) limits the resolution of the central peak.

The heterodyne technique measurement is efficient in detecting very small phase (frequency) shifts induced by the fiber noise. However, this technique has three major limitations [114]. The first limit is the delay time of the fiber: an accumulated phase shift of π occurs at a Fourier frequency of $f = 1/4\tau_f$ and results in positive feedback to the stabilization loop, limiting the servo bandwidth (servo-bumps appear at harmonics of $1/4\tau_f$ and increase the overall integrated timing jitter).

The second limit is the residual fiber noise. In fact, the heterodyne technique corrects for a phase noise accumulated during a full round trip of the light in the fiber ($2\Delta \nu_{fib}$), however, at

the detector, the laser that has only crossed one-way of fiber will suffer uncompensated phase noise. The effectiveness of one-way noise cancellation is fundamentally limited by the delay time of the fiber τ_f. The reader can find more information about this effect in [114].

The third limit of the technique is the interferometer phase noise: The fiber noise cancellation scheme consists of the laser propagating both in the fiber and a second part where the laser propagates in the free-space interferometer (i.e. between the mirrors, the AOMs and the photodiodes). The noise in this part of the interferometer is not controlled, potentially prone by air flows and temperature changes in the labs at both ends of the fiber, and it is not distinguishable from the fiber noise and thus erroneously corrected. [114].

The use of several RF-electronics (RF-synthesizers for two AOMs in different buildings, PLL, etc) induces cumulative RF-phase noise that can disturb the fiber stabilization scheme. This noise becomes negligible when all the RF-synthesizers are referenced to a common 10 MHz reference signal from the Hydrogen maser that is in turn stabilized to the same Cs fountain at PTB.

Evaluation of the fiber noise cancellation

Counting the fiber beat-note frequency using a frequency counter[9], provides an in-loop evaluation of the fiber noise. Fig. 5.3 shows the Allan deviation of the fractional frequency instability of the fiber beat note frequency. When the fiber is unstabilized the beat-note Allan deviation has a flicker floor noise behaviour at time scales above 1 s. At shorter time scales (<0.7 s), the fiber noise increases due to slow vibrations. This data was taken under relatively quite conditions (overnight). However, the fiber noise level from one measurement to the next depends on the acoustic and mechanical vibrations around the fiber.

When the fiber stabilization is on, the in-loop fractional frequency instability of the stabilized laser noise shows a white frequency noise behaviour that averages as $(1/\tau)$, where τ is the averaging time. The value of $2 \times 10^{-18}/\tau$ indicates that the heterodyne setup is efficiently suppressing the fiber noise in the loop. The real level of the frequency noise in the fiber is not observable in Fig. 5.3. However, we emphasize that the time delay and more precisely the one-way uncanceled fiber noise for the 350 m long fiber should not degrade the performance of the fiber stabilization above 10^{-17}, since much longer fibers such as the 172 km long fiber in [110], shows an out-of-loop fiber noise Allan deviation below $5 \times 10^{-16}/\tau$.

We have shown in this section, the heterodyne fiber noise cancellation technique used for transferring the cavity stabilized light. In our case, the 350 m long transfer of the stabilized laser is used for comparing the stability of our laser locked to the 39.5 cm cavity with different laser systems within PTB. An in-loop evaluation of this method does not show the real fiber noise level, but shows that the stabilization scheme is working properly, and has a lower noise limit below 10^{-18} for averaging times longer than 1 s.

---

[9]FXE High Resolution Multichannel Synchronous Phase Recorder, K+K Messtechnik GmbH
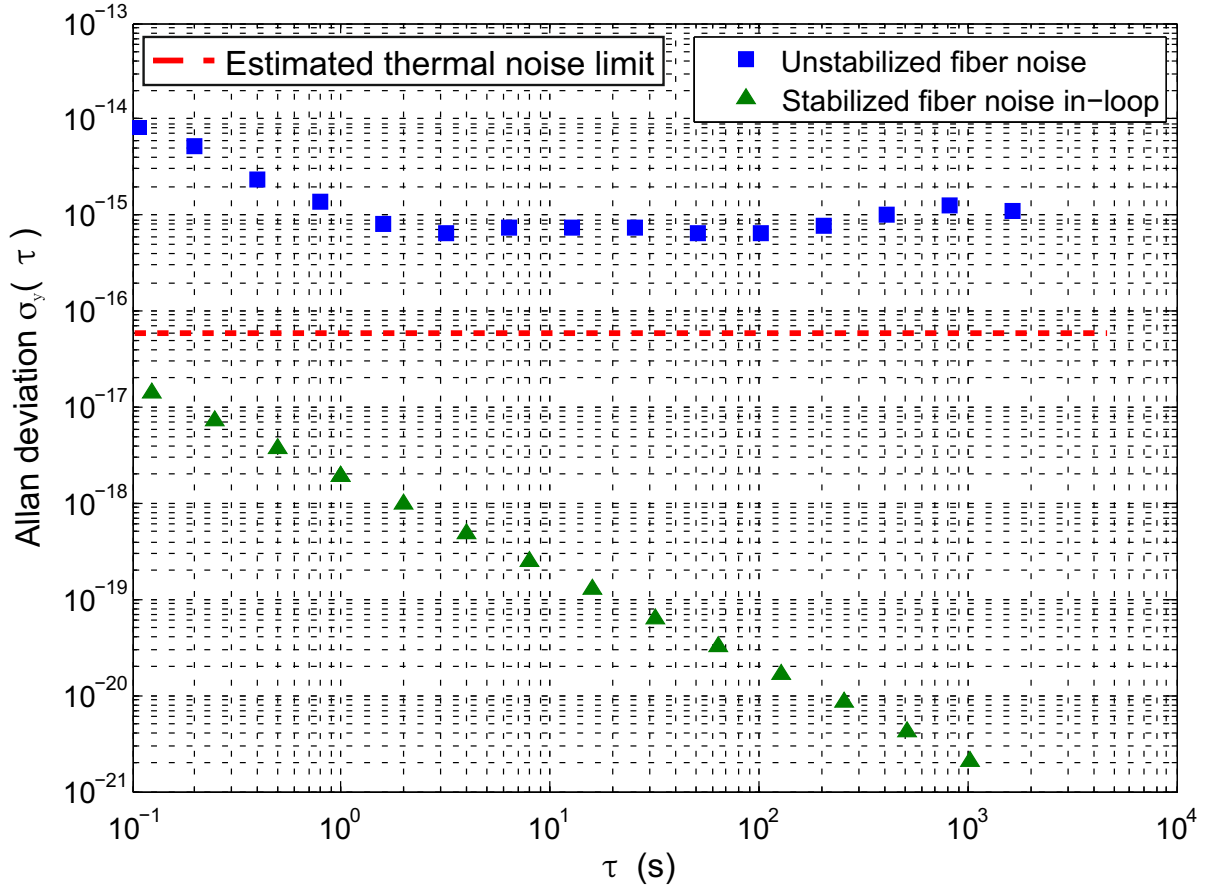
Figure 5.3: Allan deviation of the fractional frequency instability induced by the fiber noise measured by counting the beat-note frequency of the heterodyne fiber interferometer as presented in Fig. 5.1. The solid squares present the unstabilized fiber noise. The solid triangles present the in-loop stabilized fiber noise. For both measurements the laser frequency was stabilized to the 39.5 cm long cavity. The theoretical thermal noise limit of the 39.5 cm long cavity stabilized laser is plotted as a dashed line.

5.2 Stability comparison of two different lasers

During the last 15 years, the use of mode-locked femtosecond lasers has substantially facilitated optical frequency measurements [115, 116] and thus, has increased the use of optical frequencies in diverse ultra-precise measurements i.e. spectroscopy, astronomy, tests of fundamental constants etc. [117]. It has also become an indispensable tool in the field of optical frequency standards, where they are used as part of a clockwork that converts the optical frequencies to the microwave frequency regime, where the time unit is defined and the clock signal is electronically countable [118–123].

The mode-locked laser generates femtosecond pulses that, in the frequency domain, consist of a series of frequencies equally spared by the repetition rate ν_{rep}, hence the name frequency comb. Each line in the spectrum of the frequency comb is at a frequency ν_m that can be

described as:

$$\nu_m = \nu_{ceo} + m\nu_{rep} \tag{5.5}$$

where ν_{ceo} is the so-called carrier envelope offset frequency describing the offset of the entire comb with respect to zero frequency, m is the integer order number of the mode and ν_{rep} is the repetition rate.

Using Eq. 5.5 for an absolute frequency measurement requires the detection and stabilization of ν_{ceo} and ν_{rep}, which is typically performed using a stable reference frequency (i.e. a stable RF signal from a hydrogen maser) [118]. However, the residual frequency noise from fluctuations of ν_{ceo} and ν_{rep} in each comb tooth limits the frequency measurement stability. A more detailed description of the different types and functionalities of the frequency comb can be found in [19, 120]

The use of a frequency comb as a transfer-oscillator [124] enables, inter alia, the comparison between two ultra-stable lasers without introducing additional noise from the frequency comb itself [14, 63, 125, 126].
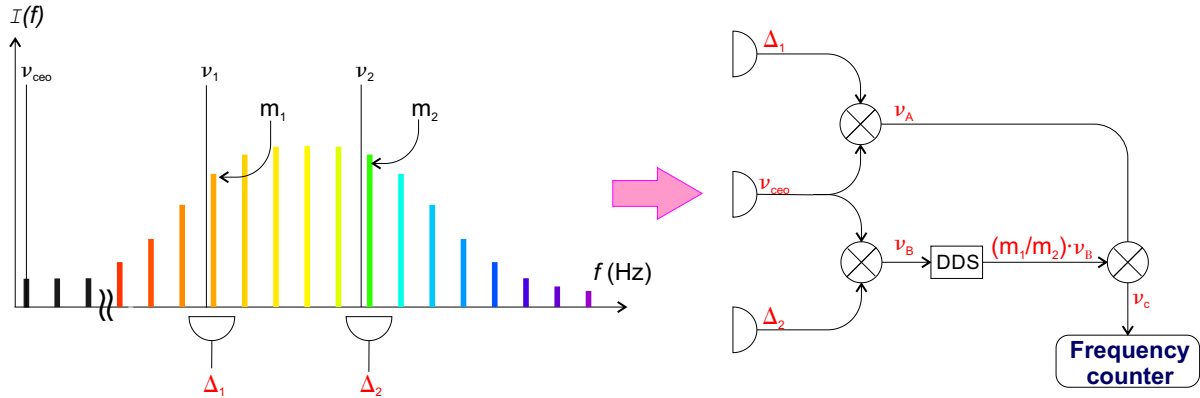
Figure 5.4: Simplified schematic of the transfer-oscillator technique used for comparing two frequencies ν_1 and ν_2 via a frequency comb. Left: the intensity $I(f)$ of the frequency comb is schematized as a function of frequency. Right: the signal processing scheme for frequency comparison as described in Eqs. 5.6- 5.9. DDS: direct digital synthesis.

In this section, we describe how this particular application of the frequency comb is used to compare the stability of the 1070 nm laser, that is in turn stabilized to our 39.5 cm cavity, with other stable lasers present in PTB operating at different wavelengths. The principle of the comparison of two stable lasers using a frequency comb is schematized in Fig. 5.4.

Consider two lasers of different frequencies ν_1 and ν_2, both within the output spectrum of the frequency comb[10]. In order to compare them, a beat-note of each laser with the frequency comb is realized, resulting in:

$$\Delta_1 = \nu_1 - \nu_{ceo} - m_1\nu_{rep} \tag{5.6}$$

for the first beat-note Δ_1 between the laser of frequency ν_1 and the nearest comb tooth of order m_1, and

$$\Delta_2 = \nu_2 - \nu_{ceo} - m_2\nu_{ref} \tag{5.7}$$

---

[10]The frequency comb used in our case (located at Paschen Bau, PTB) is a femtosecond fiber laser with $\nu_{rep} = 250$ MHz, MenloSystems.

for the second beat-note Δ_2 between the laser of frequency ν_2 and the nearest comb tooth of order m_2. These two beat notes are then mixed with the ν_{ceo} of the comb to subtract it, which is usually obtained from a beat between one comb tooth and its double in frequency within the same comb. If the comb does not have a large enough spectrum to do so, as it is the case for the comb used here, then a non-linear process is required to broaden the comb spectrum [127]. Results of the beat-notes mixing with the ν_{ceo} are given by:

$$\begin{aligned} \nu_A &= \nu_1 - m_1 \nu_{ref} \\ \nu_B &= \nu_2 - m_2 \nu_{ref}. \end{aligned} \tag{5.8}$$

One of these frequencies, for example ν_B, is then divided by the factor m_2/m_1. The rescaled frequency is produced by a direct digital synthesis (DDS) signal generator phase locked to ν_B. Mixing the frequencies $m_1/m_2 \cdot \nu_B$ and ν_A results in:

$$\nu_c = \nu_A - \nu_B = \nu_1 - \frac{m_1}{m_2}\nu_2. \tag{5.9}$$

The obtained frequency ν_c is independent of the comb parameters ν_{rep} and ν_{ceo}, and thus independent of any frequency noise that can be introduced to the measurement by imperfect stabilization of these two parameters. By measuring ν_c, the Allan deviation of ν_1 compared to ν_2 is deduced.

Comparing ultra-stable lasers at different wavelengths using a frequency comb does not degrade the quality of the measurement or influence the resulting Allan deviation. It is a reliable tool for the comparison optical frequencies with uncertainties approaching the 10^{-19} level [125] owing to the phase locks between all involved frequencies. The reader can find more details about the transfer-oscillator technique in [124].

In our case, the first laser used for the comparison was built by T. Legero *et al.* [128], and the second one by C. Hagemann *et al* [31, 63]. The use of a second stable laser with similar performance in the comparison allows the estimation of the individual frequency instabilities as discussed in Sec. 2.1.

5.3 Results and discussion

Cavity instability results

After transferring the laser via the 350 m stabilized fiber (see Sec. 5.1), two ultra-stable laser systems Ref-1 and Ref-2 are used in order to evaluate the stability of our 1070 nm laser (Al-cavity) and thus determine the performance of the 39.5 cm cavity. The lasers used in the comparison are referred to by the following names:

- Ref-1: the 1550 nm laser stabilized to the silicon cavity [31], [63]. This system is known the be one of the most stable lasers at PTB, showing a frequency instability on the order of 4×10^{-16} between 1 s and 10 s and a negligible linear drift [128].

- Ref-2: the 1550 nm laser stabilized to a 10 cm long cavity made entirely of ULE. This cavity currently has a frequency stability on the order of 1×10^{-15} between 0.2 s and 100 s and a long term linear drift of about 5 mHz/s(at the time of this measurement).

- Al-cavity: The 1070 nm laser stabilized to our 39.5 cm long cavity, since it will be used as the clock laser of the Al^+ frequency standard at PTB.
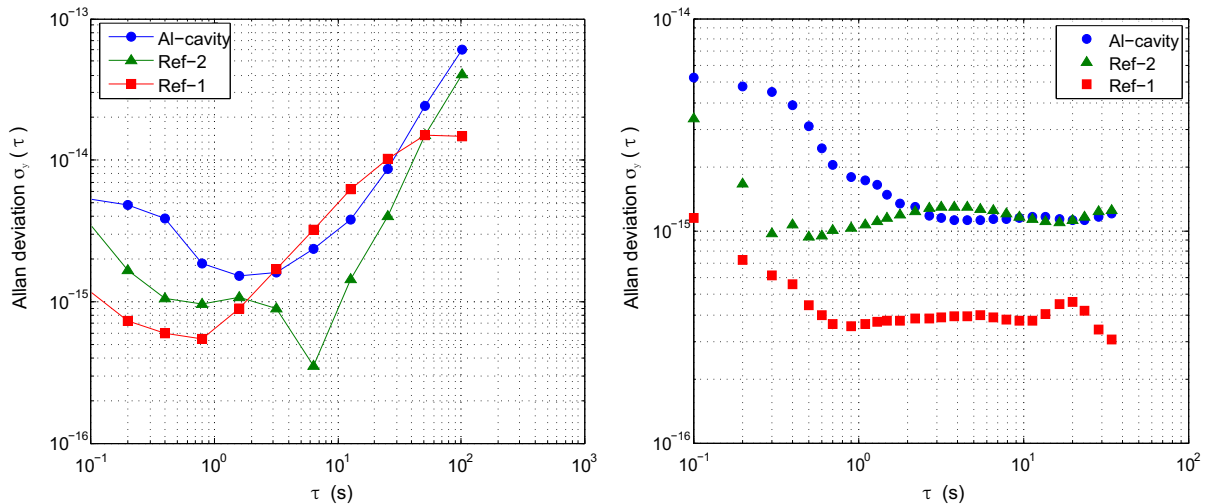
Figure 5.5: Allan deviation of the fractional frequency instabilities as a function of the averaging time τ of the three lasers used in the three-cornered hat analysis: (Al-cavity) for the 39.5 cm cavity stabilized laser, (Ref-1) for the silicon cavity stabilized laser [63], and (Ref-2) for the 10 cm all ULE cavity [128]. The left plot shows the results with linear drift and the right plot shows the results after removing linear drift. The method used in the calculation of the three-cornered hat [41], assuming no correlations (i.e. from common vibrations at PTB) between the three lasers, but the results remain the same if the method of no-correlation is used instead [42].

The three-cornered hat technique used in this measurement is explained in Sec. 2.1.

Fig. 5.5 shows the three cornered hat measurement results in terms of the individual Allan deviations of the lasers used in the three cornered hat comparison, before and after removing the residual linear drift of each cavity (See. 4.1.3).

The measured Allan deviation of the 39.5 cm cavity stabilized laser (Al-cavity) shows a flicker floor behaviour of the laser instability at 1.1×10^{-15} in the measurement averaging interval between 2 s and 20 s. This is about an order of magnitude above the expected thermal noise instability of 7×10^{-17} at 1 s.

In order to identify the limiting factor that deteriorates the stability of our cavity, we summarize the different effects contributing to the cavity instability discussed in Chap. 4 in Fig. 5.6.

Discussion of the results

From Fig. 5.6, the origin for the measured instability on the order of 10^{-15} is not evident. In this section, we present our evaluation of the possible causes that may limit the cavity stability to this level. We start by the two effects that we are concerned about the most:
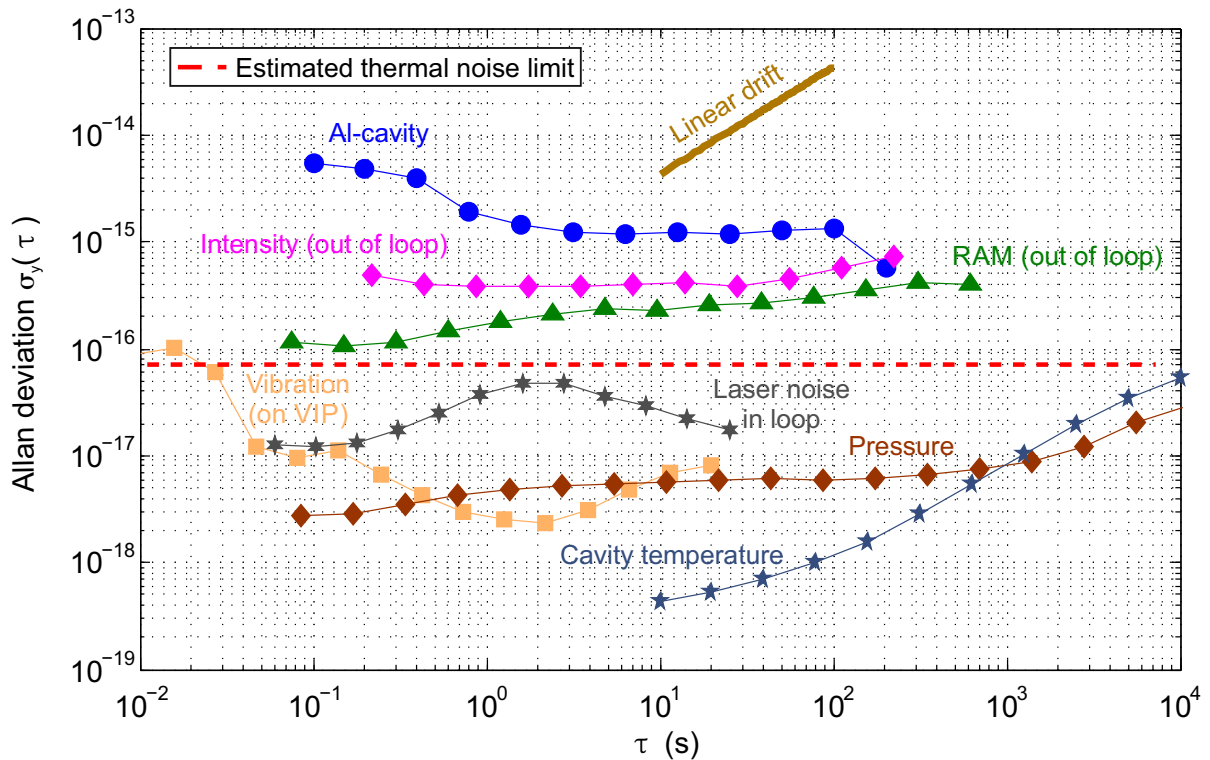
Figure 5.6: Summary of instability contributions, as discussed and evaluated in Chap. 4, to the fractional frequency instability of the laser as a function of the averaging time τ. The Al-cavity Allan deviation is the current performance of the 39.5 cm cavity stabilized laser (large blue circles) after removing the linear drift. The effect of the linear drift is plotted separately (small brown circles). The cavity thermal expansion effect (dark blue stars) is plotted assuming 4 mK of temperature excursion from the CTE null point Sec. 4.1.1 . The dashed red line represents the theoretical thermal noise limit.

- Intensity stabilization: it was shown in the previous chapter, Sec. 4.2.4, that intensity fluctuations induce frequency instability, and that the influence can increase due to the sensitivity of the current intensity stabilization optical setup to room temperature variations. However, the intensity contribution to the laser instability shown in Fig. 5.6 was not measured at the exact same time we collected the data for the laser instability.

- Fiber link stabilization: the stability of the 350 m fiber link was evaluated in Sec. 5.1 in-loop, which means that the real level of the fiber frequency noise is not known. Even though it is unlikely that the fiber caused the observed flicker frequency noise of the laser, a more conclusive evaluation of the quality of the fiber noise contribution to the laser is required.

For these reasons, the laser frequency instability was evaluated a second time (compared with Ref-1), in order to observe separately the intensity fluctuations and the fiber noise effects. The results in terms of Allan deviation are presented in Fig. 5.7.
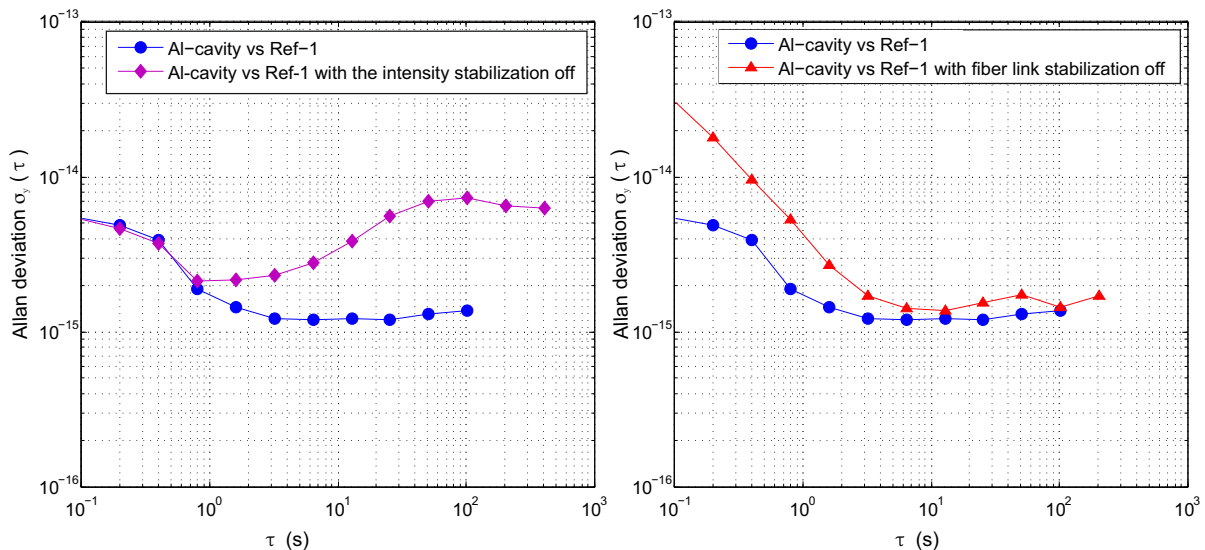
Figure 5.7: Allan deviation of the fractional frequency instability as a function of the averaging time. (Al-cavity vs Ref-1): Allan deviation of the fractional frequency instability of the 39.5 cm cavity stabilized laser (blue cycles) compared with Ref-1 (Silicon cavity). Left: the effect of a non stabilized laser intensity (full diamond) while the fiber link is stabilized. Right: the effect of the unstabilized fiber link (full triangles) while the intensity was stabilized.

From Fig.5.7, one can see that the intensity fluctuation has a different contribution to the laser noise than the fiber does. While an unstabilized fiber leads to increased laser noise at low averaging times below 1 s, the unstabilized intensity causes increased laser noise levels at longer averaging times. From these results, one could suspect that the fiber noise effect is not likely the cause of instability for time scales above one second. However, the Allan deviation of fractional frequency instability due to intensity instability could possibly be the limiting factor in our system at the time of the measurement (See Sec. 4.2.4).

Another effect, the residual amplitude modulation (RAM) (See Sec. 4.2.3), was also evaluated out-of-loop, and could be responsible for these increases of the laser instability, depending on the level of the RF-noise at the modulation frequency or the electronic noise during the actual measurements.

Possible improvement

Even though the origins of the observed flicker frequency noise with $\sigma_y \approx 10^{-15}$ between 2 s and 200 s is not completely clear, we propose several steps that may improve the results:

- Modifying the current setup of the intensity stabilization shown in Fig. 4.29 by using a 50/50 beam splitter for the cavity transmitted beam in order to eliminate the $\lambda/4$ waveplate and the polarizing beam splitter. With this approach, we can reduce the effect of the room temperature on the performance of the intensity stabilization.

- Active cancellation of the RAM effect (See Sec.4.2.3).

- Minimization of air circulation in the cavity experimental lab, room light (i.e. from computers) and low frequency acoustic vibrations by placing an acoustic box around the cavity vacuum chamber.

- Elimination of possible ground loops in the laboratory, which can influence the performance of the different electronics.

- Stabilization of the laboratory room temperature.

- Careful reevaluation of noise sources and their fluctuations over time.

Implementation of the first two points should allow us in principle to achieve the thermal noise limit of the cavity and enable us to analyze and eliminate any remaining and unaccounted for detrimental effects to the laser stability.

Although the goal of having an ultra-stable laser that is limited by the thermal noise level of the 39.5 cm long cavity was not achieved, the measured flicker floor level of 10^{-15} between 2 s and 200 s in terms of instability is most likely the results of a technical limitation that can be improved in the future.

Chapter 6

Summary and Outlook

The main motivation of this thesis was to build an ultra-stable passive optical cavity that will be used for the sub-Hertz spectroscopy of a single ion aluminum frequency standard at PTB.

Laser stabilization to passive optical cavities is fundamentally limited by thermal noise originating from the cavity mirror coatings. In this work we investigated two different approaches to reduce the thermal noise effects in optical cavities by increasing the laser mode size on the mirrors. The first approach consists of operating the cavity near instability. The results show that a thermal noise limit at the level of 10^{-16} at one second is attainable for a 10 cm long cavity. This is useful for the development of ultra-stable portable lasers, e.g. for portable stable lasers [79], transportable frequency standards [80], and for future space missions of gravitational wave detectors such as Laser Interferometer Space Antenna (LISA) [129] and GRACE-2 Follow-on [130], for which short cavities with reduced thermal noise are advantageous. The second approach consists of increasing the cavity length. We calculated that for a 39.5 cm long cavity, a thermal noise-limited Allan deviation below 10^{-16} at 1 s is reachable when the cavity is operating under optically stable conditions.

A challenging task appears when choosing to design a long cavity in terms vibration sensitivity. Using numerical simulations, we were able to design a quasi-symmetric 39.5 cm long cavity made of ultra-low expansion spacer material and fused silica mirrors, for which the estimated thermal noise limit is 7×10^{-17} at 1 s. The numerical simulations were also used to predict the optimum supporting points of the cavity for a minimum acceleration vibration sensitivity. Furthermore, the adjustable design allows correction for machining tolerances by possible adjustment of the support position.

For the experimental part of this thesis, highly reflective mirrors were optically contacted to the 39.5 cm long cavity spacer with especially designed supporting points. A UHV chamber, containing two heat shields, where one has an actively stabilized temperature, was designed and assembled to protect the cavity from environmental perturbations. The system was installed in a dedicated laboratory, where all of the electronics, the laser system, and the vibration isolation system are contained around the optical cavity.

By characterizing the different aspects of the cavity, it was shown for the first time that an almost 40 cm long cavity can have a measured vibration sensitivity equal to or below 10^{-12}/m·s^2 in all three directions, in agreement with what the numerical simulation predicted. With this design, we show that an insensitive cavity was realized, with vibration, temperature,

and pressure fractional length instabilities below the calculated thermal noise limit.

The Pound Driver Hall laser stabilization technique was implemented, showing a robust suppression of the free running laser noise up to a 560 kHz bandwidth, due to the narrow cavity linewidth of $2\pi \times 580$ Hz. However, this technique is sensitive to residual amplitude modulation (RAM). A passive minimization of RAM was performed and leads to an induced fractional frequency instability of up to 4×10^{-16} for averaging times shorter than 200 s. The current result can be improved by implementing an active RAM cancellation scheme. The relatively high thermal expansion coefficient of the fused silica mirrors of the cavity make it particularly sensitive to intra-cavity power fluctuations and leads to an estimated induced fractional frequency instability (flicker floor) of 4×10^{-16}. This level can increase due to the sensitivity of the current intensity stabilization optical setup to variations of the room temperature. We plan to improve the current optical setup in order to reduce the temperature dependency.

The evaluation of the performance of the cavity requires the transfer of the stabilized laser via a 350 m fiber to a different laboratory at PTB. The evaluation of the implemented fiber noise cancellation scheme shows an in-loop fractional frequency instability averaging as $2 \times 10^{-18}/\tau$, which we assume not to be a limitation on the transferred laser stability. Using a frequency comb, the frequency of the laser stabilized to the 39.5 cm cavity was compared to that of several stable lasers present at PTB. The results show a flicker floor at $\sigma_y = 1.1 \times 10^{-15}$ for averaging times between 2 s and 200 s. We believe that these results do not represent the optimum laser stabilization that the 39.5 cm cavity could achieve. Corrections to technical limitations such as the residual amplitude modulation and the laser intensity stabilization can help to improve these results. In the future, we aim to correct these limitations on the current performance of the cavity. Replacing the currently used diode laser with a fiber laser will further improve the stability of the laser.

Appendix A

Test a monolithic high-reflectivity mirror

We have characterized the monolithic reflective mirror used by Dr. Daniel Friedrich *et al.* in reference [70] at different laser wavelengths.
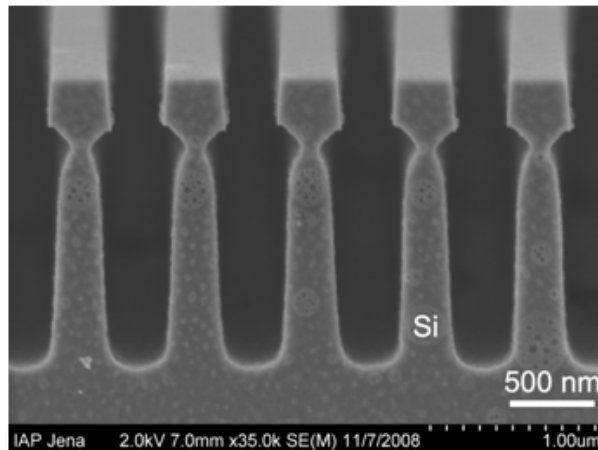
Figure A.1: Monolithic mirror from a nanostructured single silicon crystal as shown in reference [70].

These mirrors are based on a surface nanostructure on a single crystal of silicon. A picture of this nanostructure is shown in Fig. A.1. The achieved high reflectivity relies on resonant coupling to a guided optical mode of the surface nanostructure. Since no coating is involved, these mirrors benefit from the quality factor of $Q \sim 10^8$ for silicon at room temperature [57], meaning mechanical losses $\phi = 1/Q$ two orders of magnitude lower than for dielectric coating. Thus, such mirrors will reduce the thermal noise effect on ultra-stable cavities.

In reference [70], the reflectivity of this nanostructured mirror was measured to be $R = (99.79 \pm 0.01)\%$ at 1.55 μm wavelength. Theoretical simulations predicts a reflectivity maximum for about 1.543 μm laser wavelength. At PTB, we used a tunable laser with a range of 1.44 μm to 1.64 μm wavelength, with which we evaluated the reflectivity of the monolithic mirror for different wavelengths[1]. The maximum power of this laser is 7.9 mW. We build a

---

[1]With the help of Dr. Daniel Friedrich from Max-Planck-Institut für Gravitationsphysik (Albert-Einstein-Institut)

cavity made of one coupling mirror of known high reflectivity of $R_1 = r_1^2 = 99.9841\%$ (measured value for wavelength between 1.52 μm and 1.57 μm) and one nanostructured mirror of reflectivity $R_2 = r_2^2$. The low power of the laser was not suitable to reproduce the measurements with the method used in reference [70], where the laser is frequency modulated and the reflected modulation sidebands are used as a scale for determining the width of the transmitted carrier peak. Since the two cavity mirrors have different reflectivity values, the cavity has an impedance mismatching and thus losses in the Airy transmitted peak intensity and higher reflected power. For a lossless Fabry Perot cavity, the power reflection factor P_{RF} can be written on resonance as a function of the reflectivity of the mirrors r_1 and r_2:

$$P_{RF} = \frac{r_1^2 + r_2^2 - 2r_1r_2}{1 + r_1^2 r_2^2 - 2r_1r_2} \times \eta \tag{A.1}$$

where η is the correction factor ($0 \leq \eta \leq 1$) that reflects the mode matching efficiency (Chap. 2). Using this formula and replacing r_1 by the known value of the reflectivity of the coupling mirror, we can find out the reflectivity of the nanostructured mirror r_2 by measuring the power reflection factor of the cavity for different laser wavelengths[2]. We obtain the value of the correction factor η by equating our results for the reflectivity of the nanostructured mirror at 1.55 μm to the value given in reference [70] and then using the resulting correction factor to extrapolate the results for different wavelengths.
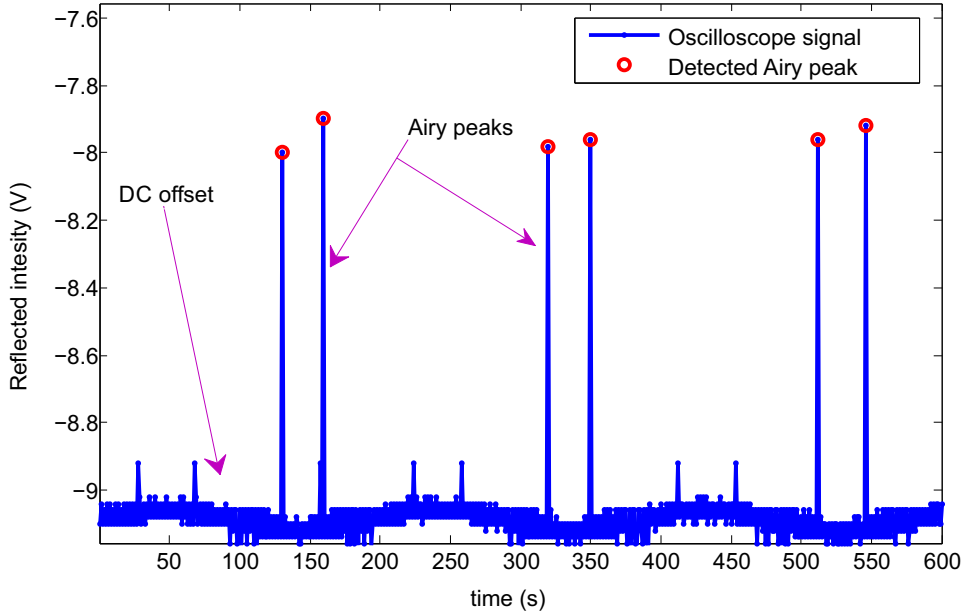
Figure A.2: Reflected intensity of the cavity made of one monolithic silicon mirror and one dielectric reference mirror (inverted signal). Power of the laser is 7.9 mW at 1.545 μm, the scope is at Peak detection acquisition mode.

A typical reflection spectrum taken while scanning the tunable laser is given in Fig. A.2. The position of the spot laser on the nanostructured mirror was optimized according by maximizing the dip amplitude in the reflected intensity.

---

[2]The movable mount of the monolithic mirror blocks the cavity transmitted beam.

We find[3] the peaks in every reflected power signal, and averaged over the different values to get the Airy peak intensity that we call intensity **A**. The DC offset is different for different wavelengths, and we can average over the DC line to get the DC offset value that we call intensity **B**. The relative intensity of the Airy peaks, is in this case 1-**A/B**. The power reflection function is then plotted against the different wavelengths to create Fig. A.3.
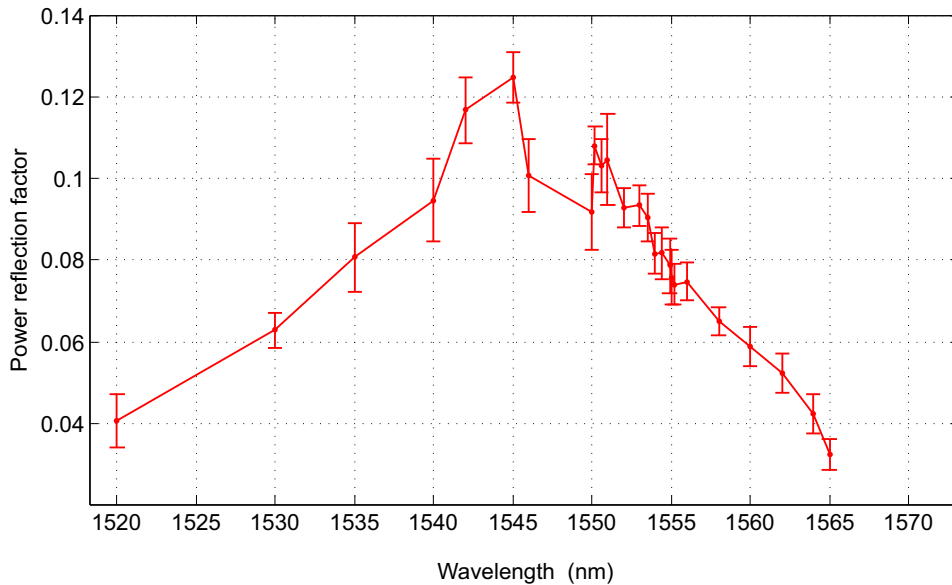
Figure A.3: Power reflection factor as a function of the wavelength of the laser at an optimum position of the monolithic silicon mirror. The power of the laser is 7.68 mW. The size of the laser beam on the monolithic planar mirror is 67 μm. The error-bar is calculated from the standard deviation of the Airy peak intensities and the DC signal and added according the error propagation theorem.

At 1.550 μm wavelength we have a power reflection factor equal to 0.091 that corresponds to a reflectivity of the monolithic mirror equal to $R_2 = 99.79\%$ if we choose the mode matching correction factor $\eta = 81.2\%$ to reproduce the same reflectivity value of reference [70]. We use this same correction factor to deduce the reflectivity of the monolithic mirror at different wavelengths. For a power reflection factor equal to 0.123 ± 0.006 which means a coupling efficiency equal to 12.31% at a wavelength of 1.545 μm, we calculate a higher reflectivity of the mirror equal to $(R_2 = 99.81 \pm 0.02)\%$ for $\eta = 81.2\%$. The high error bar is due to the high statistical error contribution from the DC signal due to the low power of the laser and the photodiode residual noise.

---

[3]We use the script "peak-finder Matlab script" available online under math-works.de/matlabcentral/fileexchange.

Appendix B

Comparison of different cavity mounting concepts

The mounting design discussed in Sec. 3.3 was the result of a detailed investigation of several mounting concepts for 39.5 cm long ULE cavity spacers. In Tab. B.1 a summary of the vibration sensitivity and the machining tolerance of three different mounting strategies for cavities of outer dimension $39.5 \times 15 \times 15 \, \text{cm}^3$ is given. Similar mounting designs have been discussed previously [81, 83, 87], and we adapted them for the case of a long spacer. We determined the optimum support points and sensitivity to tolerances for all cases as described in the previous section. We found that the vibration sensitivity to machining tolerances of all studied designs is very similar and thus not a selection criteria. However, practical aspects, such as manufacturing feasibility, and adjustability of the support points determined the choice for the design studied in detail in Sec. 3.3.
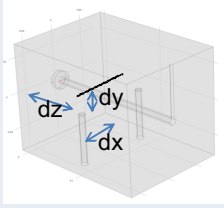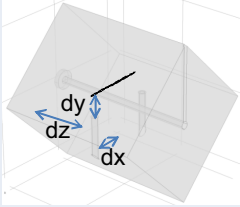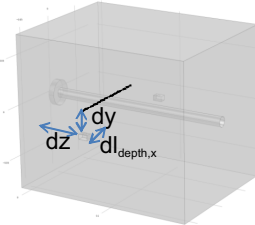
The spacer in case *A* of Tab. B.1 is supported from the bottom through 4 blind holes of a fixed diameter of 8 mm and a depth of 70.4 mm. The end surface of the blind hole is lower than the center horizontal (X, Z) plane of the cavity by $dy = 4.6$ mm to compensate the length change induced by the symmetry-breaking with respect to this plane. We simulate the case of supporting the cavity with pads of 2 mm diameter fixed onto four supporting legs that enter these blind holes. A major limitation of this design consists in the lack of degrees of freedom with respect to positioning the supporting legs inside the blind holes to compensate small errors. In principle, this could be alleviated by choosing a larger diameter for the holes, or going through a mushroom design [84]. However, machining of such a long blind hole with the required precision is challenging.

The spacer in case *B* mitigates this problem to some degree by being rotated by $45°$ [87] around its optical axis with respect to the designs in *A* and *C*. The supporting legs are placed in four blind holes of fixed diameter 8 mm. We simulate the case of supporting the cavity with pads of 2 mm diameter fixed onto four supporting legs. The end surface of the blind hole is 6.1 mm below the middle plane of symmetry (X, Z) to eliminate the sensitivity to vertical acceleration.

The spacer in case *C* is designed to reduce the asymmetry introduced by the supporting cut-outs as much as possible. The rectangular cut-outs on the sides of the spacer are 1.1 mm below the (X, Z) middle plane of the cavity to compensate the asymmetry due to these cut-

outs. We simulate the case of supporting the cavity with four pads of 2 mm diameter from these cut-outs. The advantage of this design is the possibility of moving the pads in both X and Z direction that helps optimizing the dx and dz parameters. At the same time, the small cut-outs can be easily machined with high precision, well below the required tolerances of a few hundred μm. The geometry of this design is very similar to the design discussed in Sec. 3.3, however, the diameter of the cavity considered here is 15 cm.

| Design of the cavity Y ↱X ↱Z	Direction of acceleration 1 g = 9.8 ms^{-2}	Tolerances	
		k_j $(10^{-12}/(g\cdot mm))$	κ_j $(10^{-12}/(g\cdot mm^2))$
A	Vertical	$140\cdot\delta dy$	$20\cdot\delta dz$
	Horizontal	≈ 0	$19\cdot\delta dz$
	Axial	≈ 0	$47\cdot(\delta dy\text{-}dy)$
B	Vertical	$130\cdot\delta dy$	$20\cdot\delta dz$
	Horizontal	≈ 0	$36\cdot\delta dz$
	Axial	≈ 0	$89\cdot(\delta dy\text{-}dy)$
C $(dl_{depth,x}=7.5mm, dl_{depth,y}=5mm, dl_{depth,z}=5mm)$	Vertical	$150\cdot\delta dy$	$26\cdot\delta dz$
	Horizontal	≈ 0	$20\cdot\delta dz$
	Axial	≈ 0	$76\cdot(\delta dy\text{-}dy)$

Table B.1: FEM simulation results for the machining tolerances of 3 different mechanical support designs of optical cavities made of ULE spacer and FS mirrors. L= 39.5 cm is the length of the cavity, the depth and width of all spacers is D= 15 cm. The. $dl_{depth,x}$, $dl_{depth,y}$ and $dl_{depth,z}$ are the dimensions of the cutouts in the case B. For case A and C the position along the X axis noted by dx is optimized then fixed since its influence is minor once we optimize dy parameter (position along Y axis) and δdz parameter (position along Z axis)

.

Appendix C

Complete optical Setup
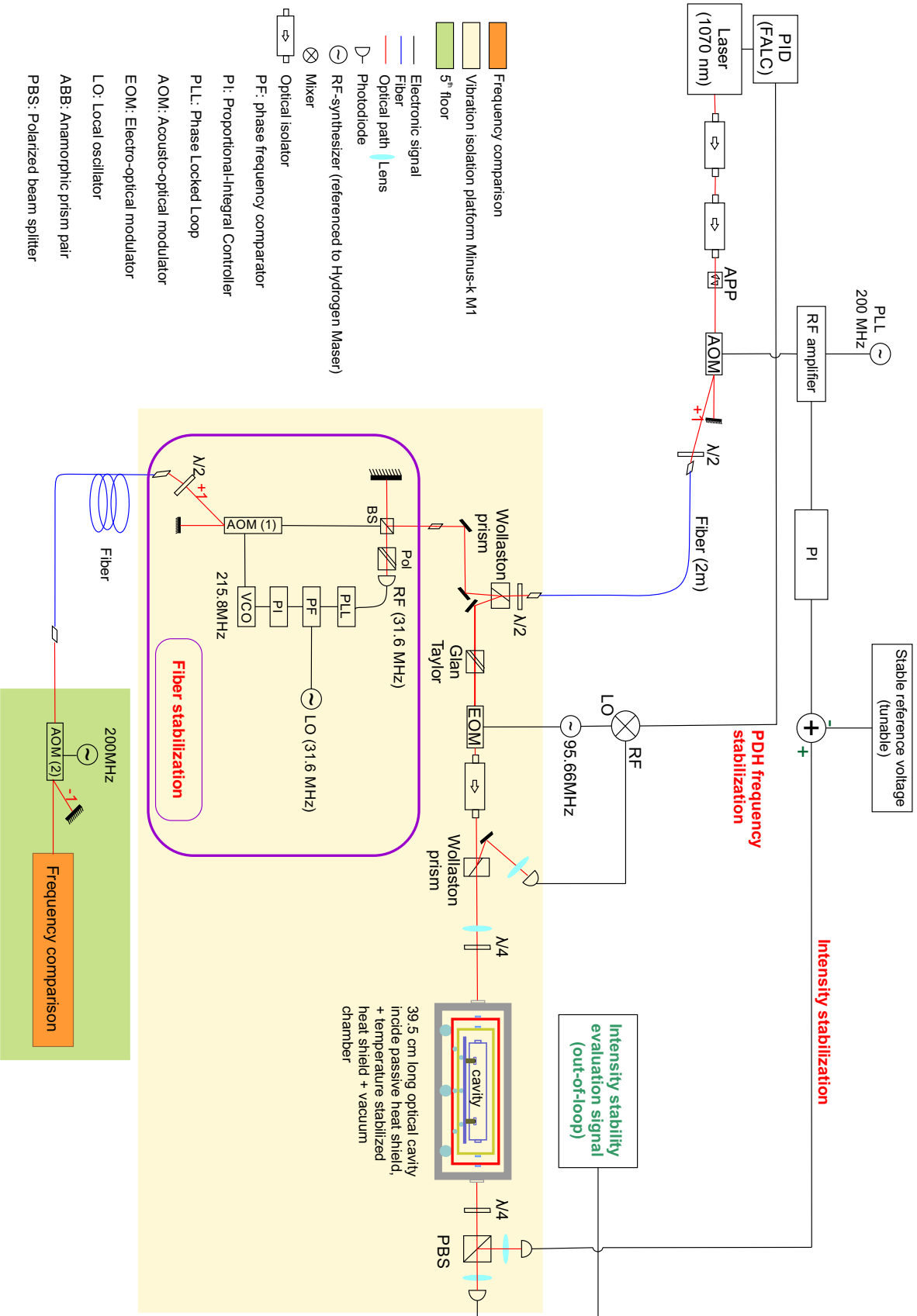
Figure C.1: General sketch of the experimental optical setup used for the 1070 nm laser frequency stabilization to 39.5 cm long optical cavity. The setup includes laser intensity stabilization scheme and fiber stabilization scheme.
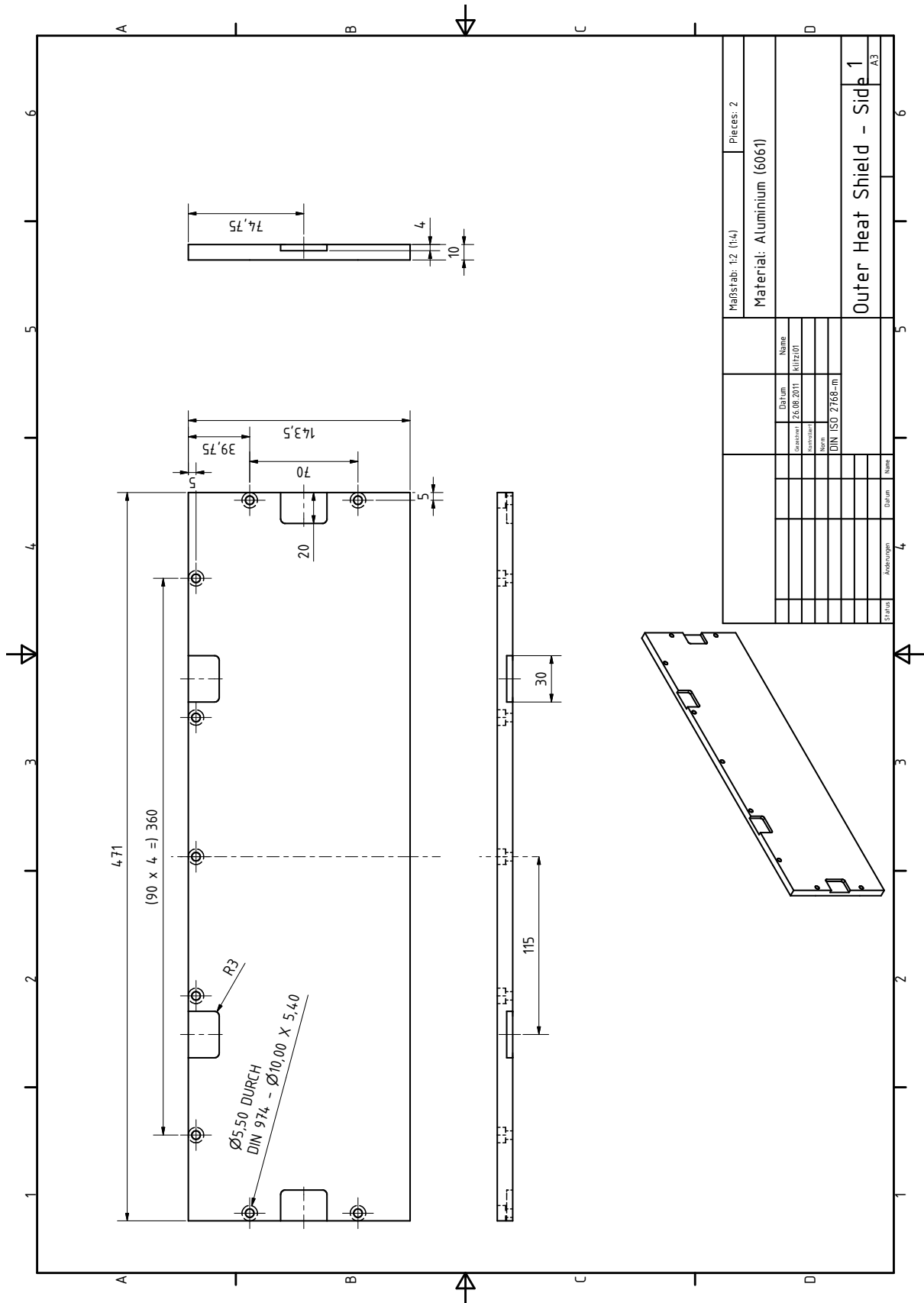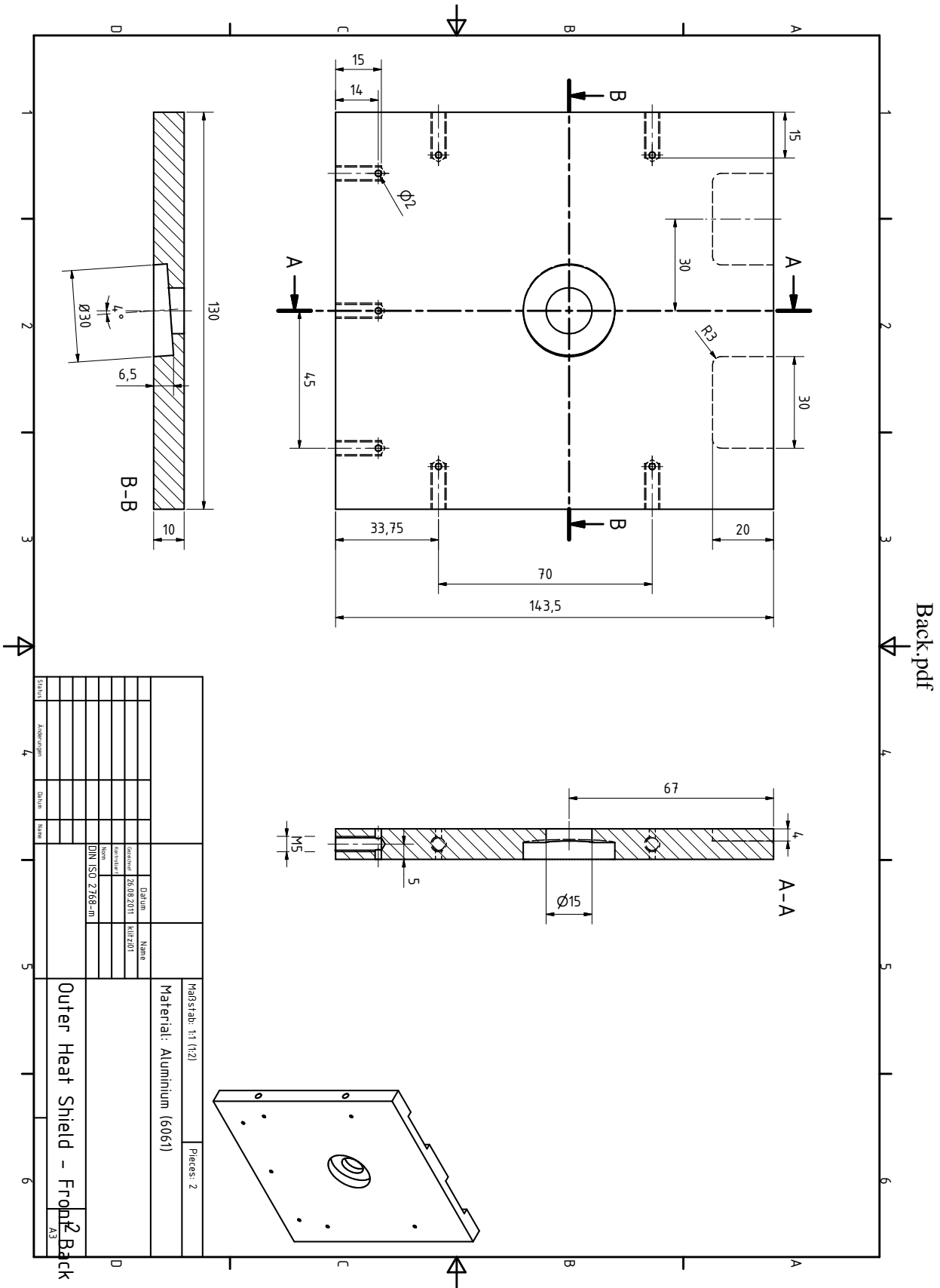
Appendix D

Vacuum system design

Figure D.1: Clock cavity technical drawing.

Figure D.2: Invar cavity support (bridge 2).

Figure D.3: Invar cavity support (bridge).

Figure D.4: Invar support (leg design).

Figure D.5: ULE plate for bridge mounting strategy.

Figure D.6: Top part of the vacuum chamber.

Figure D.7: Bottom part of the vacuum chamber.

Figure D.8: Outer heat shield. Part 1.

Figure D.9: Outer heat shield. Part 2.

Figure D.10: Outer heat shield. Part 3.
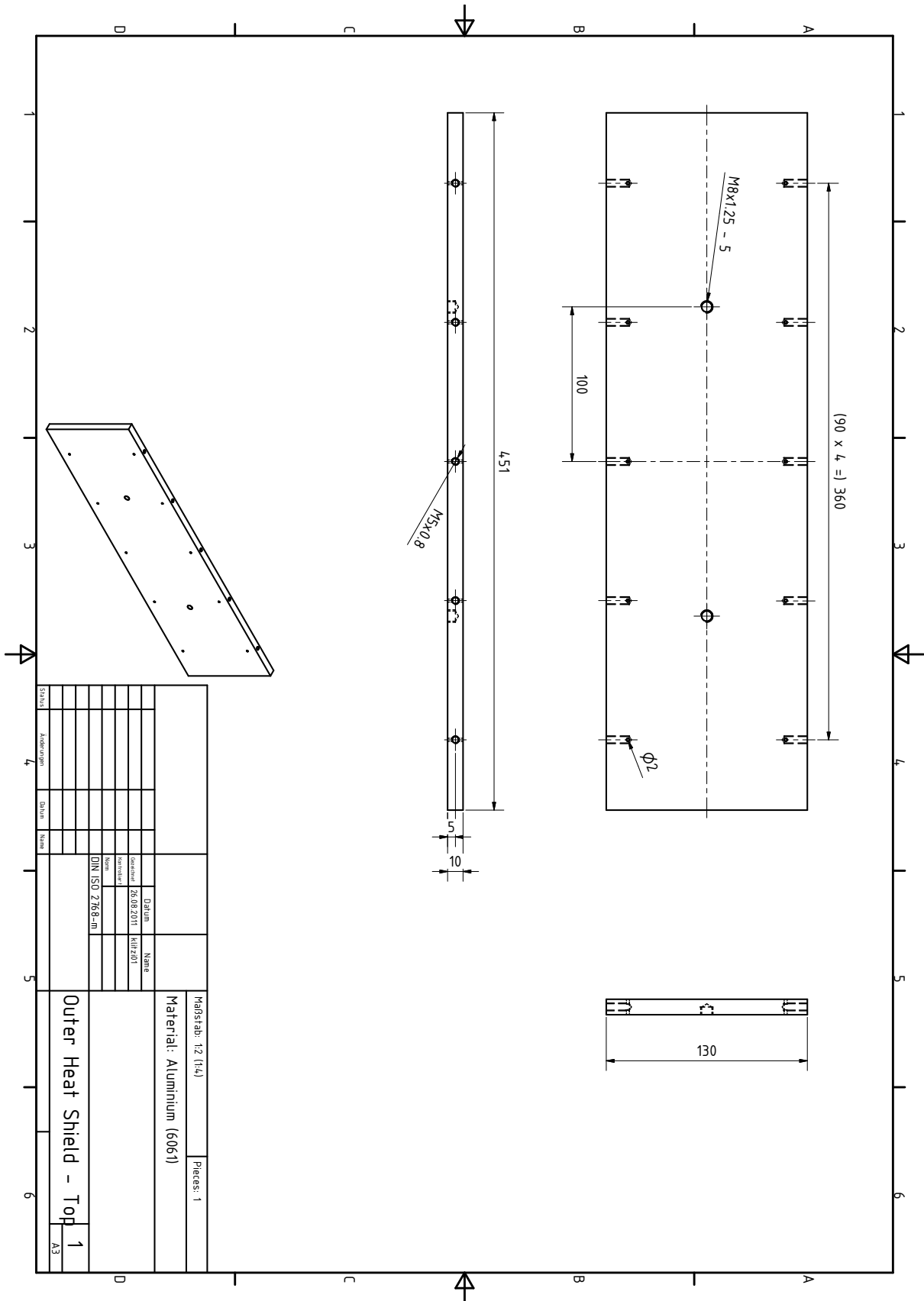
Figure D.11: Outer heat shield. Part 4.
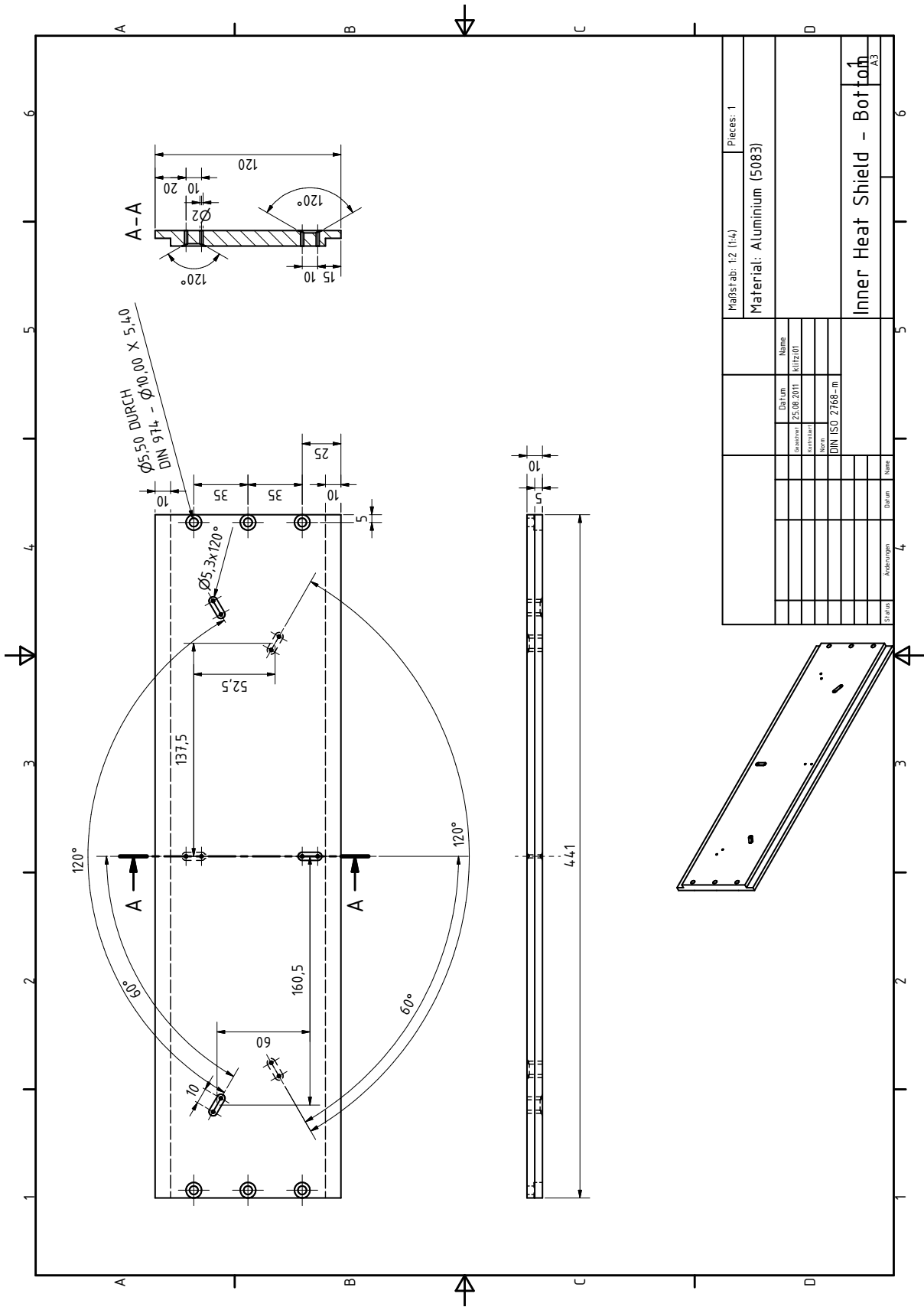
Figure D.12: Inner heat shield. Part 1.

Figure D.13: Inner heat shield. Part 2.
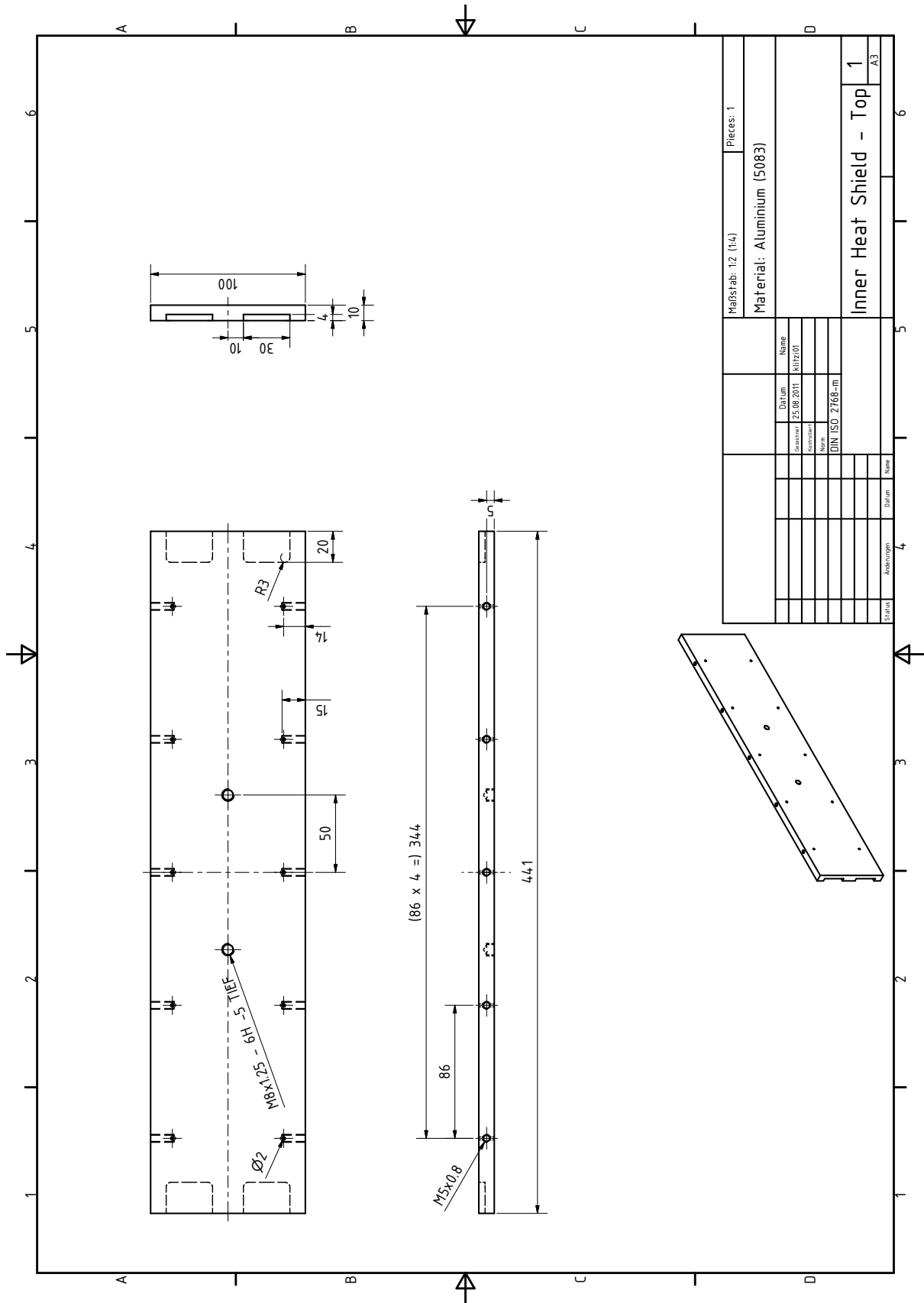
Figure D.14: Inner heat shield. Part 3.

Figure D.15: Inner heat shield. Part 4.

Appendix E

Intensity stabilization PI
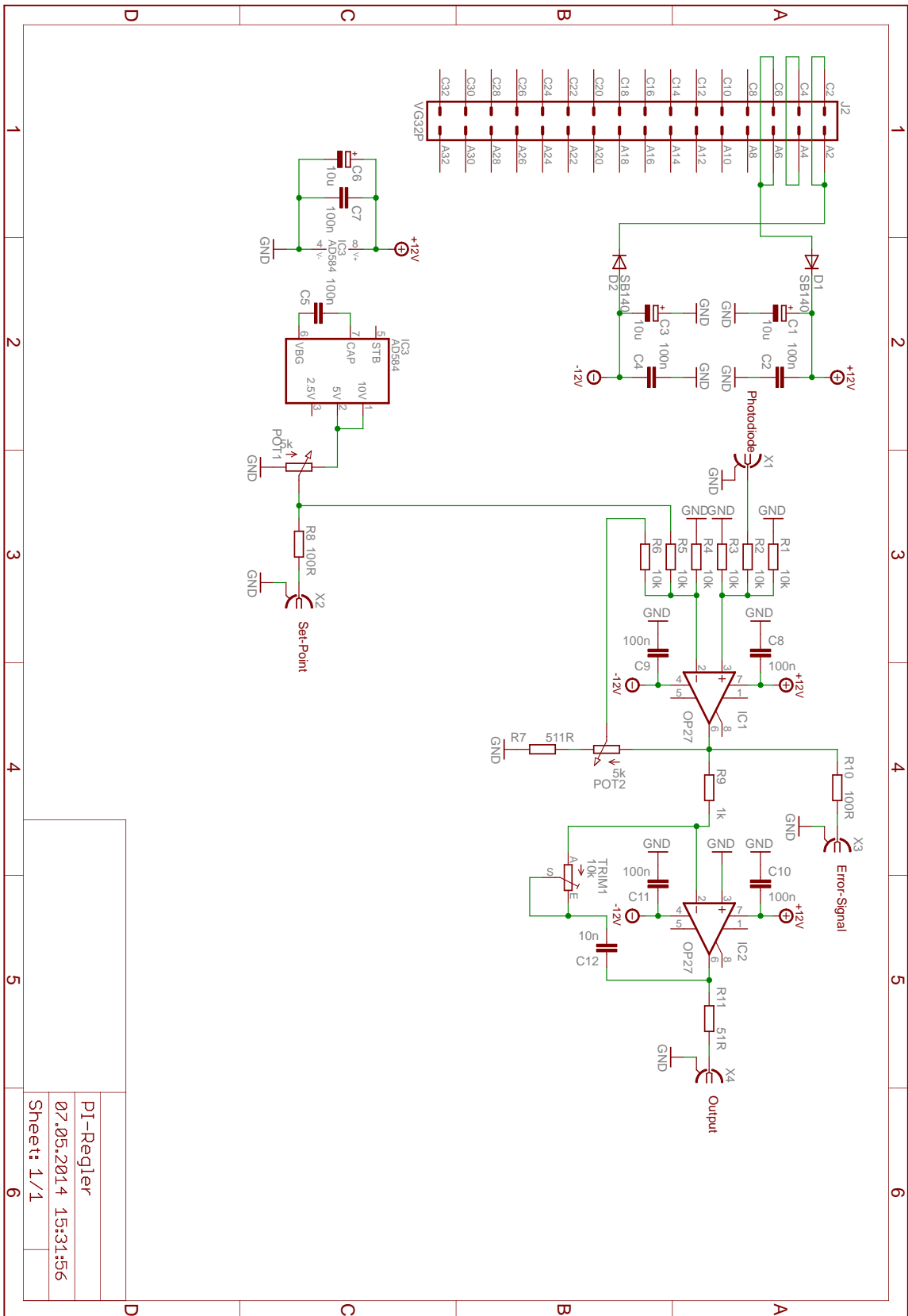
Figure E.1: PI-regulator used for the intensity stabilization.

Bibliography

[1] S. Chu, "Cold atoms and quantum control," *Nature*, vol. 416, no. 6877, pp. 206–210, 2002. 1

[2] C. Cohen-Tannoudji and W. D. Phillips, "New mechanisms for laser cooling," *Physics Today*, vol. 43, no. 10, pp. 33–40, 1990. 1

[3] J. R. Abo-Shaeer, C. Raman, J. M. Vogels, and W. Ketterle, "Observation of vortex lattices in Bose-Einstein condensates," *Science*, vol. 292, no. 5516, pp. 476–479, 2001. 1

[4] S. Haroche, "Nobel lecture: Controlling photons in a box and exploring the quantum to classical boundary," *Review of Modern Physics*, vol. 85, no. 3, p. 1083, 2013. 1

[5] D. J. Wineland, "Nobel lecture: Superposition, entanglement, and raising Schrödinger cat," *Review of Modern Physics*, vol. 85, p. 1103, 2013. 1

[6] P. O. Schmidt, T. Rosenband, C. Langer, W. M. Itano, J. C. Bergquist, and D. J. Wineland, "Spectroscopy using quantum logic," *Science*, vol. 309, pp. 749–752, 2005. 1, 7

[7] J. L. Hall, "Nobel lecture: Defining and measuring optical frequencies," *Review of Modern Physics*, vol. 78, no. 4, p. 1279, 2006. 1

[8] T. W. Hänsch, "Nobel lecture: Passion for precision," *Review of Modern Physics*, vol. 78, no. 4, pp. 1297–1309, 2006. 1

[9] C. Braxmaier, O. Pradl, H. Müller, A. Peters, J. Mlynek, V. Loriette, and S. Schiller, "Proposed test of the time independence of the fundamental constants α and m_e/m_p using monolithic resonators," *Physical Review D*, vol. 64, no. 4, p. 042001, 2001. 1

[10] S. Herrmann, A. Senger, K. Möhle, M. Nagel, E. V. Kovalchuk, and A. Peters, "Rotating optical cavity experiment testing lorentz invariance at the 10^{-17} level," *Physical Review D*, vol. 80, no. 10, p. 105011, 2009. 1

[11] B. C. Barish and R. Weiss, "LIGO and the detection of gravitational waves," *Physics Today*, vol. 52, pp. 44–50, 1999. 1

[12] T. L. Nicholson, M. J. Martin, J. R. Williams, B. J. Bloom, M. Bishof, M. D. Swallows, S. L. Campbell, and J. Ye, "Comparison of two independent Sr optical clocks with 1×10^{-17} stability at 10^3 s," *Physical Review Letters*, vol. 109, no. 23, p. 230801, 2012. 1, 2

[13] P. Gill, "Optical frequency standards," *Metrologia*, vol. 42, p. S125, 2005. 1

[14] C. W. Chou, D. B. Hume, J. C. J. Koelemeij, D. J. Wineland, and T. Rosenband, "Frequency comparison of two high-accuracy Al^+ optical clocks," *Physical Review Letters*, vol. 104, no. 7, p. 070802, 2010. 1, 90

[15] T. Rosenband *et al.*, "Frequency ratio of Al^+ and Hg^+ single-ion optical clocks; metrology at the 17th decimal place," *Science*, vol. 319, no. 5871, pp. 1808–1812, 2008. 1

[16] A. D. Ludlow *et al.*, "Sr lattice clock at 1×10^{-16} fractional uncertainty by remote optical evaluation with a Ca clock," *Science*, vol. 319, no. 5871, pp. 1805–1808, 2008. 1

[17] T. Udem and F. Riehle, "Frequency combs applications and optical frequency standards," *Rivista del Nuovo Cimento*, vol. 30, no. 12, p. 563, 2007. 1

[18] T. J. Quinn, "Practical realization of the definition of the metre (1997)," *Metrologia*, vol. 36, no. 3, pp. 211–244, 1999. 1

[19] F. Riehle, *Frequency Standards: Basics and Applications*. Wiley-Vch, 2004. 1, 2, 3, 4, 9, 13, 59, 90

[20] T. Schneider, E. Peik, and C. Tamm, "Sub-hertz optical frequency comparisons between two trapped $^{171}Yb^+$ ions," *Physical Review Letters*, vol. 94, no. 23, p. 230801, 2005. 1

[21] J. Von Zanthier, M. Eichenseer, A. Y. Nevsky, M. Okhapkin, C. Schwedes, and H. Walther, "A single indium ion optical frequency standard," *Laser Physics-Lawrence*, vol. 15, no. 7, p. 1021, 2005. 1

[22] K. Matsubara, H. Hachisu, S. Nagano, Y. Li, A. Nogami, C. Locke, K. Hayasaka, M. Hosokawa, and T. Ido, "Direct frequency comparison between a single Ca^+ clock and a Sr lattice clock," in *European Frequency and Time Forum & International Frequency Control Symposium (EFTF/IFC), 2013 Joint*. IEEE, 2013, pp. 525–528. 1, 2

[23] S. Falke *et al.*, "The ^{87}Sr optical frequency standard at PTB," *Metrologia*, vol. 48, no. 5, p. 399, 2011. 1

[24] S. Weyers, U. Hübner, R. Schröder, C. Tamm, and A. Bauch, "Uncertainty evaluation of the atomic caesium fountain CSF1 of the PTB," *Metrologia*, vol. 38, no. 4, p. 343, 2001. 1

[25] T. Rosenband *et al.*, "Frequency comparison of Al$^+$ and Hg$^+$ optical standards," in *Laser Spectroscopy: Proceedings of the XVIII International Conference on ICOLS 2007 Telluride, Colorado, USA, 24-29 June 2007*. World Scientific Publishing Company, 2008, p. 297. 1

[26] B. C. Young, F. C. Cruz, W. M. Itano, and J. C. Bergquist, "Visible lasers with subhertz linewidths," *Physical Review Letters*, vol. 82, no. 19, pp. 3799–3802, 1999. 1, 20, 21

[27] R. W. P. Drever, J. L. Hall, F. V. Kowalski, J. Hough, G. M. Ford, A. J. Munley, and H. Ward, "Laser phase and frequency stabilization using an optical resonator," *Appl. Phys. B: Lasers and Optics*, vol. 31, no. 2, pp. 97–105, 1983. 2, 13

[28] K. Numata, A. Kemery, and J. Camp, "Thermal-noise limit in the frequency stabilization of lasers with rigid cavities," *Physical Review Letters*, vol. 93, no. 25, p. 250602, 2004. 2, 17, 18, 19, 20, 21

[29] Y. Y. Jiang, A. D. Ludlow, N. D. Lemke, R. W. Fox, J. A. Sherman, L. S. Ma, and C. W. Oates, "Making optical atomic clocks more stable with 10^{-16}-level laser stabilization," *Nature Photonics*, vol. 5, no. 3, pp. 158–161, 2011. 2, 20

[30] M. D. Swallows, M. J. Martin, M. Bishof, C. Benko, Y. Lin, S. Blatt, A. M. Rey, and J. Ye, "Operating a ^{87}Sr optical lattice clock with high precision and at high density," *IEEE Transactions on Ultrasonics, Ferroelectrics and Frequency Control*, vol. 59, no. 3, pp. 416–425, 2012. 2, 20, 22, 55

[31] C. Hagemann, "Ulta-stable laser based on a cryogenic single-crystal silicon cavity," Ph.D. dissertation, 2012. 2, 59, 60, 74, 91

[32] J. B. Wuebbena, "Controlling motion in quantum logic clocks," Ph.D. dissertation, 2014. 2, 7

[33] S. Amairi, T. Legero, T. Kessler, U. Sterr, J. B. Wübbena, O. Mandel, and P. O. Schmidt, "Reducing the effect of thermal noise in optical cavities," *Applied Physics B: Lasers and Optics*, pp. 1–10, 2012. 1, 18

[34] N. M. Strickland, P. B. Sellin, Y. Sun, J. L. Carlsten, and R. L. Cone, "Laser frequency stabilization using regenerative spectral hole burning," *Physical Review B*, vol. 62, no. 3, p. 1473, 2000. 2

[35] M. J. Thorpe, L. Rippe, T. M. Fortier, M. S. Kirchner, and T. Rosenband, "Frequency stabilization to 6×10^{-16} via spectral-hole burning," *Nature Photonics*, vol. 5, no. 11, pp. 688–693, 2011. 2

[36] A. Arie and R. L. Byer, "Absolute frequency stabilization of diode-pumped Nd:YAG lasers," *Laser Physics*, vol. 4, no. 2, pp. 387–391, 1994. 2

[37] N. Castagna, N. Chiodo, M. Lours, D. Holleville, Y. Lecoq, O. Acef, and F. D. Burck, "Iodine stabilized IR laser sources," in *European Frequency and Time Forum & International Frequency Control Symposium (EFTF/IFC), 2013 Joint*. IEEE, 2013, pp. 405–408. 2

[38] J. Rutman, "Characterization of phase and frequency instabilities in precision frequency sources: Fifteen years of progress," *Proceedings of the IEEE*, vol. 66, no. 9, pp. 1048–1075, 1978. 4

[39] C. A. Greenhall, "Frequency stability review," *Telecommunications and Data Acquisition Progress Report*, vol. 88, pp. 200–212, 1987. 5

[40] P. Tavella and A. Premoli, "Estimating the instabilities of N clocks by measuring differences of their readings," *Metrologia*, vol. 30, no. 5, p. 479, 1994. 5

[41] J. E. Gray and D. W. Allan, "A method for estimating the frequency stability of an individual oscillator," in *Proceedings of the 8th Annual Symposium on Frequency Control*, vol. 2439, 1974, pp. 277–287. 5, 92

[42] F. J. Galindo and J. Palacio, "Estimating the instabilities of N correlated clocks," $31^{s}t$ PTTI planning meeting, Tech. Rep., 1999. 5, 92

[43] C. R. Ekstrom, F. Torcaso, E. A. Burt, and D. N. Matsakis, "Estimating the stability of N clocks with correlations," in *Proceedings of the 1999 Joint Meeting of the European Frequency and Time Forum, 1999 and the IEEE International Frequency Control Symposium, 1999*, vol. 1. IEEE, 1999, pp. 168–172. 5

[44] W. M. Itano, J. C. Bergquist, J. J. Bollinger, J. M. Gilligan, D. J. Heinzen, F. L. Moore, M. G. Raizen, and D. J. Wineland, "Quantum projection noise: Population fluctuations in two-level systems," *Physical Review A*, vol. 47, no. 5, p. 3554, 1993. 6

[45] T. Rosenband *et al.*, "Observation of the $^{1}S_0$–> $^{3}P_0$ clock transition in $^{27}Al^{+}$." *Physical Review Letters*, vol. 98, p. 220801, May 2007. 6

[46] E. Peik, T. Schneider, and C. Tamm, "Laser frequency stabilization to a single ion," *Journal of Physics B: Atomic, Molecular and Optical Physics*, vol. 39, no. 1, p. 145, 2006. 6, 7

[47] E. Riis and A. G. Sinclair, "Optimum measurement strategies for trapped ion optical frequency standards," *Journal of Physics B: Atomic, Molecular and Optical Physics*, vol. 37, no. 24, p. 4719, 2004. 6

[48] T. Udem, S. A. Diddams, K. R. Vogel, C. W. Oates, E. A. Curtis, W. D. Lee, W. M. Itano, R. E. Drullinger, J. C. Bergquist, and L. Hollberg, "Absolute frequency measurements of the Hg^{+} and Ca optical clock transitions with a femtosecond laser," *Physical Review Letters*, vol. 86, no. 22, p. 4996, 2001. 7

[49] M. Vaughan, *The Fabry-Perot interferometer: history, theory, practice and applications*. CRC press, 1989. 7

[50] A. E. Siegman, *Lasers*. University Science Books, 1986, vol. 94941. 7, 11, 12, 25, 27

[51] B. E. A. Saleh and M. C. Teich, *Fundamentals of photonics*. John Wiley & Sons, 1991. 7

[52] E. D. Black, "An introduction to pound–drever–hall laser frequency stabilization," *American Journal of Physics*, vol. 69, no. 1, pp. 79–87, 2001. 13, 67, 72

[53] O. Mor and A. Arie, "Performance analysis of drever-hall laser frequency stabilization using a proportional+integral servo," *IEEE Journal of Quantum Electronics*, vol. 33, no. 4, pp. 532–540, 1997. 15, 16, 67

[54] A. Gillespie and F. Raab, "Thermally excited vibrations of the mirrors of laser interferometer gravitational-wave detectors," *Physical Review D*, vol. 52, no. 2, pp. 577–585, 1995. 17

[55] Y. Levin, "Internal thermal noise in the LIGO test masses: A direct approach," *Physical Review D*, vol. 57, no. 2, p. 659, 1998. 17, 20

[56] T. Hong, H. Yang, E. K. Gustafson, R. X. Adhikari, and Y. Chen, "Brownian thermal noise in multilayer coated mirrors," *Physical Review D*, vol. 87, p. 082001, 2013. 17

[57] K. Numata, "Direct measurement of mirror thermal noise," *University of Tokyo, Department of Physics*, 2002. 17, 18, 98

[58] B. Mours, E. Tournefier, and J. Y. Vinet, "Thermal noise reduction in interferometric gravitational wave antennas: using high order tem modes," *Classical and Quantum Gravity*, vol. 23, no. 20, p. 5777, 2006. 17

[59] H. B. Callen and T. A. Welton, "Irreversibility and generalized noise," *Physical Review*, vol. 83, no. 1, pp. 34–40, 1951. 18

[60] H. B. Callen and R. F. Greene, "On a theorem of irreversible thermodynamics," *Physical Review*, vol. 86, pp. 702–710, 1952. 18

[61] V. B. Braginsky, M. L. Gorodetsky, and S. P. Vyatchanin, "Thermodynamical fluctuations and photo-thermal shot noise in gravitational wave antennae," *Physics Letters A*, vol. 264, no. 1, pp. 1–10, 1999. 18

[62] T. Kessler, T. Legero, and U. Sterr, "Thermal noise in optical cavities revisited," *JOSA B*, vol. 29, no. 1, pp. 178–184, 2012. 18, 20

[63] T. Kessler, C. Hagemann, C. Grebing, T. Legero, U. Sterr, F. Riehle, M. J. Martin, L. Chen, and J. Ye, "A sub-40-mhz-linewidth laser based on a silicon single-crystal optical cavity," *Nature Photonics*, vol. 6, no. 10, pp. 687–692, 2012. 19, 55, 60, 90, 91, 92

[64] G. D. Cole, S. Gröblacher, K. Gugler, S. Gigan, and M. Aspelmeyer, "Monocrystalline AlGaAs heterostructures for high-reflectivity high-Q micromechanical resonators in the MHz regime," *Applied Physics Letters*, vol. 92, no. 26, p. 261108, 2008. 19

[65] G. D. Cole, W. Zhang, M. J. Martin, J. Ye, and M. Aspelmeyer, "Tenfold reduction of brownian noise in high-reflectivity optical coatings," *Nature Photonics*, vol. 7, pp. 644–650, 2013. 19

[66] H. J. Kimble, B. L. Lev, and J. Ye, "Optical interferometers with reduced sensitivity to thermal noise," *Physical Review Letters*, vol. 101, no. 26, p. 260602, 2008. 19

[67] M. L. Gorodetsky, "Thermal noises and noise compensation in high-reflection multi-layer coating," *Physics Letters A*, vol. 372, no. 46, pp. 6813–6822, 2008. 19

[68] F. Y. Khalili, "Reducing the mirrors coating noise in laser gravitational-wave antennae by means of double mirrors," *Physics Letters A*, vol. 334, no. 1, pp. 67–72, 2005. 19

[69] K. Somiya, A. G. Gurkovsky, D. Heinert, S. Hild, R. Nawrodt, and S. P. Vyatchanin, "Reduction of coating thermal noise by using an etalon," *Physics Letters A*, vol. 375, no. 11, pp. 1363–1374, 2011. 19

[70] F. Brückner, D. Friedrich, T. Clausnitzer, M. Britzger, O. Burmeister, K. Danzmann, E.-B. Kley, A. Tünnermann, and R. Schnabel, "Realization of a monolithic high-reflectivity cavity mirror from a single silicon crystal," *Physical Review Letters*, vol. 104, no. 16, p. 163903, 2010. 19, 98, 99, 100

[71] COMSOL, "Multiphysics," 2010. 20, 27

[72] R. Lalezari, "private communication," 2010. 20

[73] J. Millo, D. V. Magalhães, C. Mandache, Y. Le Coq, E. M. L. English, P. G. Westergaard, J. Lodewyck, S. Bize, P. Lemonde, and G. Santarelli, "Ultrastable lasers based on vibration insensitive cavities," *Physical Review A*, vol. 79, no. 5, p. 053829, 2009. 20, 21, 26, 31

[74] S. A. Webster, M. Oxborrow, S. Pugla, J. Millo, and P. Gill, "Thermal-noise-limited optical cavity," *Physical Review A*, vol. 77, no. 3, p. 033847, 2008. 21

[75] S. T. Gulati and M. J. Edwards, "ULE^{TM}-zero expansion, low density, and dimensionally stable material for lightweight optical systems," *Critical Reviews of Optical Science and Technology, vol. CR*, no. 67, p. 1997, 1997. 21

[76] Fused Silica SiO$_2$ Material Properties, http://www.accuratus.com/fused.html. 21

[77] S. Webster and P. Gill, "Force-insensitive optical cavity," *Optics Letters*, vol. 36, no. 18, pp. 3572–3574, 2011. 22, 26, 32, 55, 56

[78] B. Argence, E. Prevost, T. Lévèque, R. Le Goff, S. Bize, P. Lemonde, and G. Santarelli, "Prototype of an ultra-stable optical cavity for space applications," *Optics Express*, vol. 20, no. 23, pp. 25 409–25 420, 2012. 22

[79] D. R. Leibrandt, M. J. Thorpe, J. C. Bergquist, and T. Rosenband, "Field-test of a robust, portable, frequency-stable laser," *Optics Express*, vol. 19, no. 11, pp. 10 278–10 286, 2011. 22, 96

[80] S. Vogt, C. Lisdat, T. Legero, U. Sterr, I. Ernsting, A. Nevsky, and S. Schiller, "Demonstration of a transportable 1 Hz-linewidth laser," *Applied Physics B: Lasers and Optics*, vol. 104, no. 4, pp. 741–745, 2011. 22, 96

[81] T. Nazarova, F. Riehle, and U. Sterr, "Vibration-insensitive reference cavity for an ultra-narrow-linewidth laser," *Applied Physics B: Lasers and Optics*, vol. 83, no. 4, pp. 531–536, 2006. 26, 29, 31, 101

[82] L. Chen, J. L. Hall, J. Ye, T. Yang, E. Zang, and T. Li, "Vibration-induced elastic deformation of Fabry-Perot cavities," *Physical Review A*, vol. 74, no. 5, p. 053801, 2006. 26

[83] Y. Tao, L. Wen-Bo, Z. Er-Jun, and C. Li-Sheng, "Decreased vibrational susceptibility of Fabry–Perot cavities via designs of geometry and structural support," *Chinese Physics*, vol. 16, no. 5, p. 1374, 2007. 26, 101

[84] S. Webster, M. Oxborrow, and P. Gill, "Vibration insensitive optical cavity," *Physical Review A*, vol. 75, no. 1, p. 011801(R), 2007. 26, 101

[85] D. Guyomarct'h, G. Hagel, C. Zumsteg, and M. Knoop, "Some aspects of simulation and realization of an optical reference cavity," *Physical Review A*, vol. 80, no. 6, p. 063802, 2009. 26

[86] S. T. Dawkins, R. Chicireanu, M. Petersen, J. Millo, D. V. Magalhães, C. Mandache, Y. Le Coq, and S. Bize, "An ultra-stable referenced interrogation system in the deep ultraviolet for a mercury optical lattice clock," *Applied Physics B: Lasers and Optics*, vol. 99, no. 1, pp. 41–46, 2010. 26

[87] P. Dubé, A. A. Madej, J. E. Bernard, L. Marmet, and A. D. Shiner, "A narrow linewidth and frequency-stable probe laser source for the ^{88}sr^{+} single ion optical frequency standard," *Applied Physics B: Lasers and Optics*, vol. 95, no. 1, pp. 43–54, 2009. 26, 59, 101

[88] Y. N. Zhao, J. Zhang, A. Stejskal, T. Liu, V. Elman, Z. H. Lu, and L. J. Wang, "A vibration-insensitive optical cavity and absolute determination of its ultrahigh stability," *Optics Express*, vol. 17, no. 11, pp. 8970–8982, 2009. 26

[89] D. R. Leibrandt, M. J. Thorpe, M. Notcutt, R. E. Drullinger, T. Rosenband, and J. C. Bergquist, "Spherical reference cavities for frequency stabilization of lasers in non-laboratory environments," *Optics Express*, vol. 19, no. 4, pp. 3471–3482, 2011. 26, 55

[90] T. Nazarova, "Towards the quantum noise limit in Ramsey-Bordé atom interferometry," Ph.D. dissertation, 2007. 33

[91] R. W. Fox, "Temperature analysis of low-expansion Fabry-Perot cavities," *Optics Express*, vol. 17, no. 17, pp. 15 023–15 031, 2009. 35

[92] T. Legero, T. Kessler, and U. Sterr, "Tuning the thermal expansion properties of optical reference cavities with fused silica mirrors," *JOSA B*, vol. 27, no. 5, pp. 914–919, 2010. 35, 36, 42, 59

[93] R. W. Fox, "Fabry-Perot temperature dependence and surface-mounted optical cavities," in *Proceedings of SPIE, the International Society for Optical Engineering.* Society of Photo-Optical Instrumentation Engineers, 2008, pp. 70 991R–1. 35

[94] J. Alnis, A. Matveev, N. Kolachevsky, T. Udem, and T. W. Hänsch, "Subhertz linewidth diode lasers by stabilization to vibrationally and thermally compensated ultralow-expansion glass Fabry-Pérot cavities," *Physical Review A*, vol. 77, no. 5, p. 053809, 2008. 36, 50

[95] J. Ekin, *Experimental Techniques for Low-Temperature Measurements: Cryostat Design, Material Properties and Superconductor Critical-Current Testing.* Oxford University Press, 2006. 37

[96] http://www.pspglobal.com/properties-compression set.html, "Elastomer properties - compression set/creep." 50

[97] http://www.minusk.com/content/products/standard/bm1-antivibration-platform-benchtop isolator.html, "Passive vibration isolation platform minus-k." 56

[98] W. M. Itano *et al.*, "Optical frequency standards based on mercury and aluminum ions," in *Society of Photo-Optical Instrumentation Engineers (SPIE) Conference Series*, vol. 6673, 2007, p. 2. 60

[99] K. P. Birch and M. J. Downs, "Correction to the updated Edlén equation for the refractive index of air," *Metrologia*, vol. 31, no. 4, p. 315, 1994. 60

[100] M. J. Lawrence, B. Willke, M. E. Husman, E. K. Gustafson, and R. L. Byer, "Dynamic response of a Fabry–Perot interferometer," *JOSA B*, vol. 16, no. 4, pp. 523–532, 1999. 62

[101] H. Rohde, J. Eschner, F. Schmidt-Kaler, and R. Blatt, "Optical decay from a Fabry–Perot cavity faster than the decay time," *JOSA B*, vol. 19, no. 6, pp. 1425–1429, 2002. 62

[102] D. S. Elliott, R. Roy, and S. J. Smith, "Extracavity laser band-shape and bandwidth modification," *Physical Review A*, vol. 26, pp. 12–18, 1982. 73

[103] A. L. Schawlow and C. H. Townes, "Infrared and optical masers," *Physical Review*, vol. 112, no. 6, p. 1940, 1958. 73

[104] W. Zhang *et al.*, "Reduction of residual amplitude modulation to 1×10^{-6} for frequency modulation and laser stabilization," *Optics Letters*, vol. 39, no. 7, pp. 1980–1983, 2014. 74, 77

[105] N. C. Wong and J. L. Hall, "Servo control of amplitude modulation in frequency-modulation spectroscopy: demonstration of shot-noise-limited detection," *JOSA B*, vol. 2, no. 9, pp. 1527–1533, 1985. 74

[106] E. A. Whittaker, C. M. Shum, H. Grebel, and H. Lotem, "Reduction of residual amplitude modulation in frequency-modulation spectroscopy by using harmonic frequency modulation," *JOSA B*, vol. 5, no. 6, pp. 1253–1256, 1988. 74

[107] P. Werle, "Laser excess noise and interferometric effects in frequency-modulated diode-laser spectrometers," *Applied Physics B: Lasers and Optics*, vol. 60, no. 6, pp. 499–506, 1995. 74

[108] L. Li, F. Liu, C. Wang, and L. Chen, "Measurement and control of residual amplitude modulation in optical phase modulation," *Review of Scientific Instruments*, vol. 83, no. 4, p. 043111, 2012. 74

[109] G. Grosche, O. Terra, K. Predehl, R. Holzwarth, B. Lipphardt, F. Vogt, U. Sterr, and H. Schnatz, "Optical frequency transfer via 146 km fiber link with 10^{-19} relative accuracy," *Optics Letters*, vol. 34, no. 15, pp. 2270–2272, 2009. 83

[110] O. Terra, G. Grosche, K. Predehl, R. Holzwarth, T. Legero, U. Sterr, B. Lipphardt, and H. Schnatz, "Phase-coherent comparison of two optical frequency standards over 146 km using a telecommunication fiber link," *Applied Physics B: Lasers and Optics*, vol. 97, no. 3, pp. 541–551, 2009. 83, 88

[111] L.-S. Ma, P. Jungner, J. Ye, and J. L. Hall, "Delivering the same optical frequency at two places: accurate cancellation of phase noise introduced by an optical fiber or other time-varying path," *Optics Letters*, vol. 19, no. 21, pp. 1777–1779, 1994. 83, 84

[112] L. G. Cohen and J. W. Fleming, "Effect of temperature on transmission in lightguides," *Bell System Technical Journal*, vol. 58, no. 4, pp. 945–951, 1979. 84

[113] S. Chang, C.-C. Hsu, T.-H. Huang, W.-C. Chuang, Y.-S. Tsai, J.-Y. Shieh, C.-Y. Leung *et al.*, "Heterodyne interferometric measurement of the thermo-optic coefficient of single mode fiber," *Chinese Journal of Physics*, vol. 38, pp. 437–442, 2000. 84

[114] P. A. Williams, W. C. Swann, and N. R. Newbury, "High-stability transfer of an optical frequency over long fiber-optic links," *JOSA B*, vol. 25, no. 8, pp. 1284–1293, 2008. 87, 88

[115] T. Udem, J. Reichert, R. Holzwarth, and T. W. Hänsch, "Absolute optical frequency measurement of the cesium D_1 line with a mode-locked laser," *Physical Review Letters*, vol. 82, no. 18, p. 3568, 1999. 89

[116] T. Udem, J. Reichert, R. Holzwarth, and T. W. Hänsch, "Accurate measurement of large optical frequency differences with a mode-locked laser," *Optics Letters*, vol. 24, no. 13, pp. 881–883, 1999. 89

[117] J. Ye and S. T. Cundiff, *Femtosecond optical frequency comb: Principle, Operation and Applications*. Springer, 2005. 89

[118] T. Udem, R. Holzwarth, and T. W. Hänsch, "Optical frequency metrology," *Nature*, vol. 416, no. 6877, pp. 233–237, 2002. 89, 90

[119] S. A. Diddams, D. J. Jones, J. Ye, S. T. Cundiff, J. L. Hall, J. K. Ranka, R. S. Windeler, R. Holzwarth, T. Udem, and T. W. Hänsch, "Direct link between microwave and optical frequencies with a 300 THz femtosecond laser comb," *Physical Review Letters*, vol. 84, no. 22, p. 5102, 2000. 89

[120] S. T. Cundiff and J. Ye, "Colloquium: Femtosecond optical frequency combs," *Reviews of Modern Physics*, vol. 75, no. 1, p. 325, 2003. 89, 90

[121] D. J. Jones, S. A. Diddams, J. K. Ranka, A. Stentz, R. S. Windeler, J. L. Hall, and S. T. Cundiff, "Carrier-envelope phase control of femtosecond mode-locked lasers and direct optical frequency synthesis," *Science*, vol. 288, no. 5466, pp. 635–639, 2000. 89

[122] S. A. Diddams, J. Ye, and L. Hollberg, "Femtosecond lasers for optical clocks and low noise frequency synthesis," in *Femtosecond Optical Frequency Comb: Principle, Operation, and Applications*. Springer, 2005, pp. 225–262. 89

[123] J. Reichert, M. Niering, R. Holzwarth, M. Weitz, T. Udem, and T. W. Hänsch, "Phase coherent vacuum-ultraviolet to radio frequency comparison with a mode-locked laser," *Physical Review Letters*, vol. 84, pp. 3232–3235, Apr 2000. 89

[124] H. R. Telle, B. Lipphardt, and J. Stenger, "Kerr-lens, mode-locked lasers as transfer oscillators for optical frequency measurements," *Applied Physics B: Lasers and Optics*, vol. 74, no. 1, pp. 1–6, 2002. 90, 91

[125] L.-S. Ma, Z. Bi, A. Bartels, L. Robertsson, M. Zucco, R. S. Windeler, G. Wilpers, C. Oates, L. Hollberg, and S. A. Diddams, "Optical frequency synthesis and comparison with uncertainty at the 10^{-19} level," *Science*, vol. 303, no. 5665, pp. 1843–1845, 2004. 90, 91

[126] X. Baillard *et al.*, "An optical lattice clock with spin-polarized ^{87}Sr atoms," *The European Physical Journal D*, vol. 48, no. 1, pp. 11–17, 2008. 90

[127] H. R. Telle, G. Steinmeyer, A. Dunlop, J. Stenger, D. Sutter, and U. Keller, "Carrier-envelope offset phase control: A novel concept for absolute optical frequency measurement and ultrashort pulse generation," *Applied Physics B*, vol. 69, no. 4, pp. 327–332, 1999. 91

[128] H. Schnatz, "Resonatorstabilisierter Faserlaser als optischer Lokaloszillator für optische Uhren und die optische Nachrichtentechnik," *TIB Hannover, Schlussbericht MNPQ-Projekt Nr. 06/07*, 2011. 91, 92

[129] J. Livas, J. Thorpe, K. Numata, S. Mitryk, G. Mueller, and V. Wand, "Frequency-tunable pre-stabilized lasers for LISA via sideband locking," *Classical and Quantum Gravity*, vol. 26, no. 9, p. 4016, 2009. 96

[130] W. Folkner *et al.*, "Laser frequency stabilization for GRACE-II," *Earth Science Technology Forum, Pasadena*, 2010. 96

Acknowledgements

اللَّهِــــــ ولے التُوۡفِیق

Dedication

This thesis is dedicated to all my family and friends.

A mon père Hedi: J'ai réalisé mon rêve grace à toi. j'ai toujours rêvé de ce moment, celui de répondre à la question posée à moi dans ta thèse. Ma réponse est *OUI*. Je suis reconnaissante pour tout ce qui tu fais pour moi et pour nous tous.

A ma mère Monia: j'obtiens toujours mes forces de toi, tu m'as appris que tout est possible si on le fait à petits pas. Continue à nous faire voir la vie en rose.

To my brave husband Karsten: You have kept your promise to me and you have been so patient and supportive and I will always remember that. Ich liebe dich mine.

To my Tunisian and German families, and to all my friends from all countries, thank you all for supporting me and believing in me.

Curriculum vitae

Sana Amairi Pyka

Contact information

sana.amairi@gmail.com

Personal information

Date of birth: 22.09.1985
Place of birth: Tunis, Tunisia
Marital status: married (no children)
Nationality: Tunisian

Education

03/2010-today	**Postgraduate studies:** Ion Quantum Logic Optical Clock Directed by: Prof. Piet O. Schmidt Title: *A long optical cavity for sub-hertz spectroscopy* QUEST Institute of Experimental Quantum Metrology Physikalisch-Technische Bundesanstalt (PTB), Braunschweig, Germany and Leibniz Universität Hannover, Germany
2008-2009	**Master degree in physics:** "Optique, Matière, Plasma", sub-specialty "Lasers et Matière" Directed by: Prof. Jacques Robert Laboratoire CNRS Aimé Cotton, Université Paris sud XI, Paris, France
2006-2008	**Bachelor degree in physics (with Honors):** "Nanoscience & Microtechnology" Project: TEMPUS-MEDA Institut Préparatoire aux Etudes Scientifiques et Technologiques (IPEST) La Marsa, Tunisia
2004-2006	**Undergraduate studies:** Diploma of DEUPC "Physics-Chemistry" Classes Préparatoires à l'institut Préparatoire aux Etudes d'Ingénieurs de Tunis (IPEIT), Tunisia
2003-2004	**Baccalaureate (with Honors) (EN: A-Levels):** Natural Sciences and Biology Lycée secondaire EL Sijoumi, Diwan Elzit Tunis, Tunisia

List of publications

1. S. Amairi, T. Legero, T. Kessler, U. Sterr, J. B. Wübbena, O. Mandel and P. O. Schmidt. Reducing the effect of thermal noise in optical cavities. *App. Phys. B: Lasers and Optics*, Vol. 113, pp. 233-243, 2013.

2. J. B. Wübbena, S. Amairi, O. Mandel and P. O. Schmidt. Sympathetic cooling of mixed-species two-ion crystals for precision spectroscopy. *Phys. Rev. A*, Vol. 85, 043412, 2012.

3. Y. Wan, F. Gebert, J. B. Wübbena, N. Scharnhorst, S. Amairi, I. D. Leroux, B. Hemmerling, N. Lörch, K. Hammerer and P. O. Schmidt. Precision spectroscopy by photon-recoil signal amplification. *Nature Communications*, Vol. 5, p. 3096, 2014. DOI:10.1038/ncomms4096